ABSTRACT

Title of Dissertation: IMPACT OF AEROSOL DIRECT AND INDIRECT EFFECTS ON EAST ASIAN AIR QUALITY DURING EAST-AIRE CAMPAIGN PERIOD

Jing Wang, Doctor of Philosophy, 2017

Dissertation directed by: Dr. Dale J. Allen, Department of Atmospheric and Oceanic Science

WRF-Chem simulations were performed for the March 2005 East Asian Studies of Tropospheric Aerosols: an International Regional Experiment (EAST-AIRE) Intensive Observation Campaign (IOC) to investigate the effects of aerosols on surface radiation and air quality. Domain-wide, WRF-Chem showed a decrease of 20 W/m^2 in surface shortwave (SW) radiation due to the aerosol direct effect (ADE), consistent with observational studies. The ADE reduced mixing and caused 24-hr surface $PM_{2.5}$ concentrations to increase in eastern China (4.4%), southern China (10%), western China (2.3%), and the Sichuan Basin (9.6%), due to a thinner planetary boundary layer (PBL) and increased stability. Conversely, surface 1-hour maximum ozone was reduced by 2.3% domain-wide and up to 12% in eastern China because less radiation reached the surface. Studies of the impact of reducing SO_2 and black carbon (BC) emissions by 80% on aerosol amounts were performed via two sensitivity simulations. Reducing SO_2 decreased surface $PM_{2.5}$ concentrations in the

Sichuan Basin and southern China by 5.4% and decreased ozone by up to 6 ppbv in the Sichuan Basin and Southern China. Reducing BC emissions decreased $PM_{2.5}$ by 3% in eastern China and the Sichuan Basin but increased surface ozone by up to 3.6 ppbv in eastern China and the Sichuan Basin. This result indicates that the benefits of reducing $PM_{2.5}$ associated with reducing absorbing aerosols may be partially offset by increases in ozone at least for a scenario when NO_x and VOC emissions are unchanged. The relative importance of direct and indirect effects in altering the atmospheric composition was then studied with two case studies of periods that featured strong synoptic systems. The case studies demonstrated that changes in primary aerosol (i.e., dust, OC) and chemically stable trace gas concentrations (i.e., CO) were mainly driven by changes in meteorological conditions due to the direct and indirect effects with the direct effect showing a stronger impact over highly polluted and dry regions and the indirect effect dominating over humid areas. Secondary aerosols (i.e., sulfate, nitrate) were affected by both changes in meteorological and chemical processes The variation of ozone due to the indirect effect was found to be associated with changes in the NO_2 photolysis rate due to changes in actinic flux driven by changes in AOD and/or COD.

IMPACT OF AEROSOL DIRECT AND INDIRECT EFFECTS ON EAST ASIAN AIR QUALITY DURING EAST-AIRE CAMPAIGN PERIOD

by

Jing Wang

Dissertation submitted to the Faculty of the Graduate School of the
University of Maryland, College Park, in partial fulfillment
of the requirements for the degree of
Doctor of Philosophy
2017

Advisory Committee:
Professor Russell R. Dickerson, Chair
Dr. Dale J. Allen, Co-Chair/Advisor
Adjunct Professor Kenneth E. Pickering
Professor Zhanqing Li
Professor John Ondov, Dean's Representative

Dedication

To my beloved family

Table of Contents

List of Tables

List of Figures

Chapter 1: Introduction

Atmospheric aerosols also known as particulate matter (PM) can be defined as a collection of airborne solid or liquid particles with sizes ranging from 0.01 to 10 μm [*Glossary, IPCC,* 2001]. Aerosols are emitted from both natural sources (i.e., sea spray, deserts and volcanoes), and anthropogenic sources (i.e., coal/fossil fuel burning and biomass burning). Aerosols emitted directly into the atmosphere such as dust and sea salt are defined as primary aerosols whereas aerosols such as sulfate, nitrate and organic aerosols that are formed in the atmosphere from chemical reactions of precursor gases are defined as secondary aerosols [*Hinds,* 1999]. Aerosols play important roles in climate through their direct and indirect effects on the radiative balance of the earth. Growing attention is being paid to the impact of aerosols on the climate because atmospheric aerosol loadings have increased dramatically since the industrial revolution, and because aerosols are a major contributor to the uncertainty in radiative forcing of climate.. Figure 1.1 (taken from *Brauer et al.* [2015]) shows time series of population-weighted $PM_{2.5}$ (particulate matter with diameter < 2.5μm) during the last 25 years for the world's 10 most populated countries. Clearly, $PM_{2.5}$ concentrations are starting to decline in developed countries such as Japan and the United States but are still increasing in developing countries such as Brazil, India and Bangladesh. $PM_{2.5}$ concentrations in China are beginning to level off but are still the highest among the 10 most populated countries.

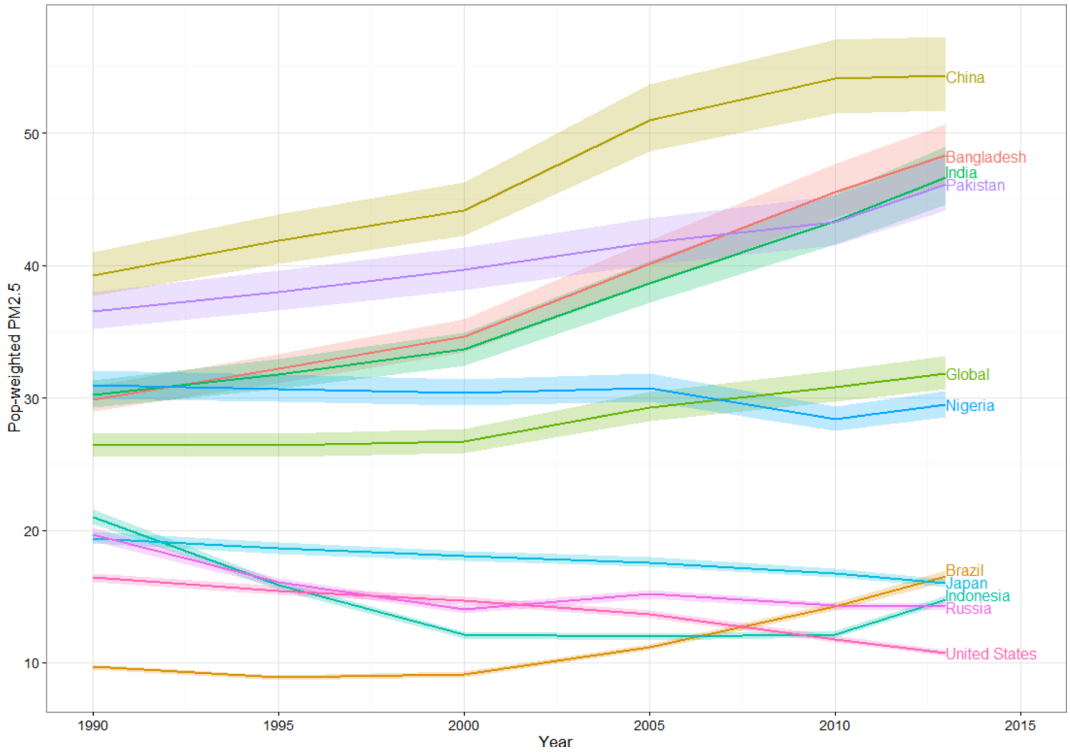

Figure 1.1. Global and country-level population-weighted mean (and 95% uncertainty intervals) concentrations of annual average $PM_{2.5}$ ($\mu g/m^3$) for 1990, 1995, 2000, 2005, 2010, and 2013 for the world's 10 most populous countries [*Brauer et al.*, 2015].

Due to its large population and fast economic development, China is the largest emission source of aerosols and their precursors [*Li et al.,* 2011a]. The Aerosol Optical Depth (AOD) is an important measure of the aerosol loading. It is a dimensionless quantity that represents the total attenuation of radiation between the top of the atmosphere and the surface caused by aerosols. The observational study by *Xin et al.* [2007] showed an annual mean AOD of 0.43 at 19 stations in the Chinese Sun Hazemeter Network (CSHNET). These values are considerably higher than the global mean of AOD (0.19) over land from Moderate Resolution Imaging

Spectroradiometer (MODIS) [*Remer et al.,* 2008]. Positive trends of AOD over the most populated regions in China (eastern and southern China) are evident from Sea-Viewing Wide Field-of-View Sensor (SeaWiFS) retrievals between 1997 and 2010 [*Hsu et al.,* 2012], indicating a degradation of air quality due to particulate matter. In January 2013, an extremely severe and persistent haze spread over a large area of northern and eastern China with monthly average surface $PM_{2.5}$ concentrations exceeding 225 $\mu g/m^3$ [*Huang et al.,* 2014] and daily surface $PM_{2.5}$ concentrations exceeding 500 $\mu g/m^3$ at several observation sites in Beijing and Shijiazhuang (the capital city of Hebei Province) [*Wang et al.,* 2014]. This record-breaking event has heightened concerns about PM pollution in China, which reduces visibility, threatens human health [*Dockery et al.,* 1993; *Harrison and Yin,* 2000], and has considerable impact on the radiative balance of the earth, and consequently the meteorological variables and chemical composition of the atmosphere through meteorology-chemistry-aerosol-radiation feedbacks [*IPCC,* 2014]. In this study, we employ an online regional model with fully coupled meteorology-chemistry-aerosol-radiation interactions to:

1. Calculate the impact of the aerosol direct effect on surface shortwave radiation, meteorological conditions, and air pollutant levels over East Asia.

2. Assess the potential impact of future emission reductions of scattering or absorbing aerosols on East Asian air quality.

3. Compare the relative importance of aerosol direct and indirect effects on meteorology and atmospheric composition via different atmospheric processes.

Chapter 2: Background

2.1 Introduction to aerosols

2.1.1 Aerosol effects

Aerosols exert impact on the radiative balance of the Earth via direct, indirect and semi-direct effects, as shown in Figure 2.1 [Figure 2.10 from *IPCC,* 2001, modified from Haywood and Boucher, 2000]. The aerosol direct effect (ADE) is the mechanism by which aerosols scatter and absorb shortwave and longwave radiation, thereby altering the radiative balance of the Earth-atmosphere system. The aerosol indirect effect (AIE) is the mechanism by which aerosols modify the microphysical and hence the radiative properties, amount, and lifetime of clouds [*IPCC,* 2001]. The effect of aerosols on the cloud droplet number concentration (CDNC) and size assuming a fixed liquid water content is called the 'first indirect effect' [*Ramaswamy et al.,* 2001], the 'cloud albedo effect' [*Lohmann and Feichter,* 2005], or the 'Twomey effect' [*Twomey,* 1977]. The effect of aerosols on the liquid water content, cloud height [*Pincus and Baker,* 1994], and lifetime of clouds has been called the 'second indirect effect' [*Ramaswamy et al.,* 2001], the 'cloud lifetime effect' [*Lohmann and Feichter,* 2005] or the 'Albrecht effect' [*Albrecht,* 1989]. Incoming solar radiation is also absorbed by aerosols consisting of black carbon and mineral dust, heating the local atmosphere and possibly reducing the incidence of cloud formation through the "semi-direct effect" [*Hansen et al.,* 1997; *Ackerman et al.,*

2000].

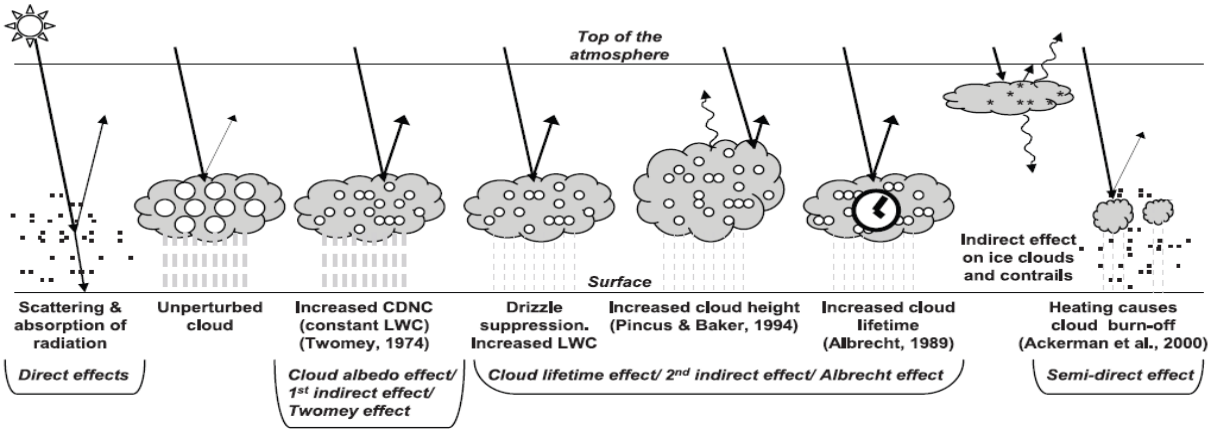

Figure 2.1. Schematic diagram showing the various radiative mechanisms associated with cloud effects that have been identified as significant in relation to aerosols [*IPCC* 2001, modified from *Haywood and Boucher,* 2000].

2.1.2 Aerosol radiative forcing

As defined in *IPCC* [2001, 2007, 2014], radiative forcing is the change in net (downward minus up) irradiance (W/m^2) at the tropopause after allowing stratospheric temperatures to readjust to radiative equilibrium, but with surface and tropospheric temperatures held fixed at unperturbed values [*Ramaswamy et al.,* 2001]. Figure 2.2 shows the estimated radiative forcing associated with changes in long-lived greenhouse gases (LLGHGs), ozone, water vapor, surface albedo, aerosols, and linear contrails due to human activities between pre-industrial times (1750) and 2005 [*IPCC,* 2007]. The increased LLGHGs and tropospheric ozone lead to substantial positive radiative forcing (warming), which is partially offset by the cooling effect of aerosols. Among these terms, aerosol radiative forcing (especially

the aerosol cloud albedo effect) contributes the largest uncertainties in total radiative forcing due to human activities.

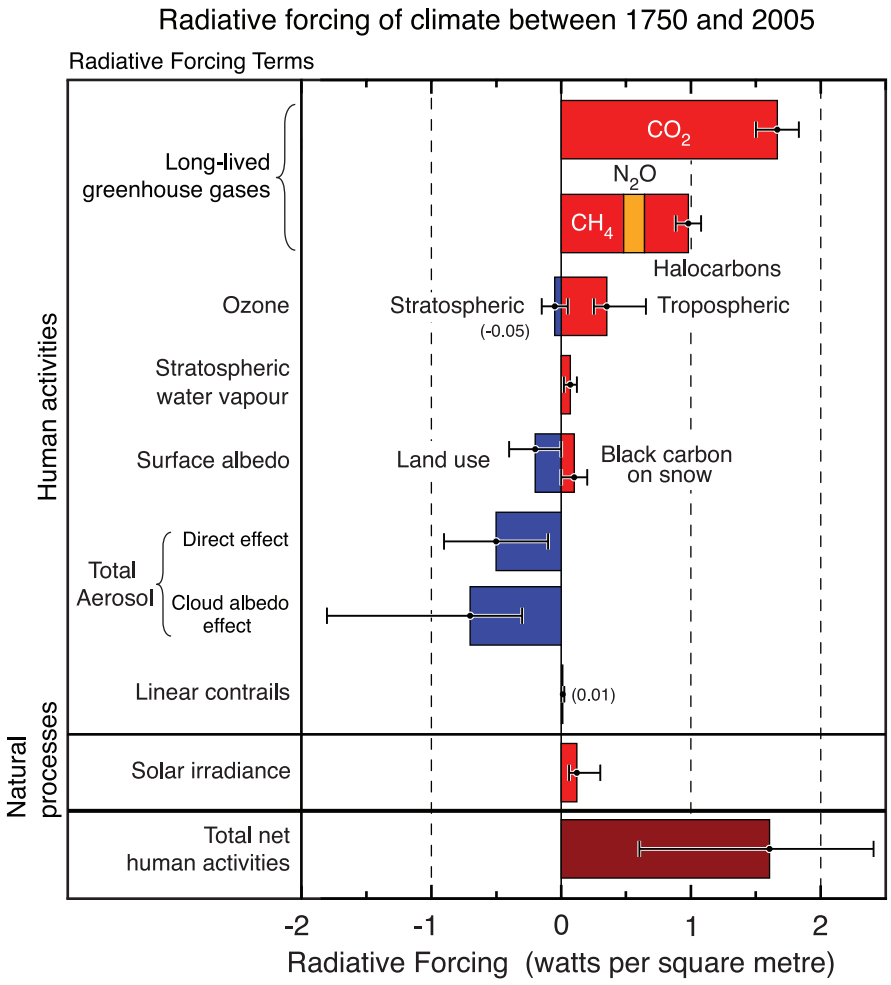

Figure 2.2. Summary of the principal components of the radiative forcing of climate. The values represent the forcing in 2005 relative to 1750 [*IPCC,* 2007].

The impact of the stratospheric temperature adjustment on radiative forcing is most important for LLGHGs. However, this term is less important for calculating the climate response to perturbations of shorter-lived quantities such as aerosols for

which alternative radiative forcing calculation methodologies can be applied. For example, the equilibrium climate response method allows the surface, tropospheric, and stratospheric temperatures to adjust, which leads to an energy equilibrium throughout the atmosphere making it possible to calculate the surface temperature change associated with radiative forcing [*IPCC,* 2007].

2.1.2.1 Aerosol direct radiative forcing

There are several variables that can be used to characterize the optical or direct radiative forcing properties of aerosols: 1) Aerosol extinction coefficient: the fractional attenuation of radiance per unit path length in units of km^{-1} (or m^{-1}); 2) Aerosol single scattering albedo (SSA, ω): the ratio of scattering optical depth to the total optical depth (scattering + extinction) of the atmosphere, measuring the effectiveness of scattering relative to extinction for the light encountering the atmospheric aerosol particles. The mean SSA was found to be 0.83 over northern China during 1993-2001 from ground observations [*Qiu et al.,* 2004], 0.89 ± 0.04 nationwide in 2005 from a combination of ground and satellite measurements [*Lee et al.,* 2007], and 0.90 ± 0.03 at a urban site in Beijing under the heavy hazy conditions of January 2013 [*Che et al.,* 2014]; 3) Aerosol asymmetry factor (g): a measure of the preferred scattering direction (forward or backward) for the light encountering the aerosol particles. In general, g=0 indicates isotropic scattering (scattering from very small particles), with scattering evenly distributed between forward and backward directions. With g>0, scattering is favored in the forward direction, and g approaches 1 for large particle Mie scattering. The asymmetry factor is correlated with the wet size of the aerosols. For example, ammonium sulfate aerosols can have asymmetry

factors ranging between 0.65 and 0.8 for relative humidity values ranging from 30% to 99.5% [*Myhre et al.,* 1998].

2.1.2.1 Aerosol indirect radiative forcing

As discussed in section 2.1.1, aerosols affect the radiative balance indirectly via their impact on cloud microphysics (i.e., cloud condensation nuclei concentrations, ice nuclei concentrations, and size distribution of cloud droplets) and macrophysics (cloud thickness, cloud height, and cloud water content).

Cloud Condensation Nuclei (CCN) and Ice Nuclei (IN) are cloud-activated aerosol particles that play an important role in determining cloud microphysical properties and the aerosol indirect effect. The likelihood that aerosol particles will take on water vapor and become CCN at a given supersaturation level depends on the sizes and composition of the aerosols. The bulk hygroscopicity parameter **κ** represents the effectiveness of an aerosol particle serving as CCN [*Rissler et al.,* 2004, 2010; *Petters and Kreidenweis,* 2007]. Aerosols with higher hygroscopicity parameters, such as sea salt, sulfates and sulfuric acid, nitrate and nitric acid and some organics, are more likely to take water vapor and become CCN. Larger aerosols are more easily activated as CCN than smaller aerosols due to the lower supersaturation required for activation [*Dusek et al.,* 2006; *Ervens et al.,* 2007]. Ice nuclei are defined as the nuclei for ice crystal formation. Homogeneous ice nucleation of pure water occurs at ~235 K (-38 °C), while heterogeneous ice nucleation takes place at temperatures higher than 235 K and lower than the melting temperature [*Koop et al.,* 2004]. Heterogeneous ice nucleation can happen via the following four processes: immersion freezing (initiated from within a cloud droplet), condensation freezing

(freezing during droplet formation), contact freezing (due to collision with an IN), and deposition nucleation (direct deposition of vapor onto IN) [*IPCC,* 2014]. Solid aerosols, i.e., mineral dust, volcanic ash, and primary bioaerosols serve as good IN [*Vali,* 1985; *Hoose and Möhler,* 2012].

Clouds cover two thirds of the Earth's surface [*IPCC,* 2014] with high spatial and temporal variations and play very important roles in regulating the Earth's radiation budget. By comparing upwelling radiation measured from satellite data on cloudy days and clear days, it was found that clouds exert a negative global average shortwave radiative forcing of ~ -50 W/m^2 and a positive longwave radiative forcing of ~ 30 W/m^2 at TOA (Top Of Atmosphere), with uncertainty ranges less than 10% from published satellite estimates [*Loeb et al.,* 2009]. Analyses of data from the Earth Radiation Budget Experiment (ERBE) [*Collins et al.,* 1994] indicate that small changes in cloud macrophysics and microphysics can have a great impact on the energy balance. *Ramaswamy et al.* [2001] showed that a 5% increase of present day negative shortwave radiative forcing by clouds could offset the warming effect induced by increases in greenhouse gases between 1750 and 2000. However, aerosol-cloud interactions contribute large uncertainties in model radiative forcing due to the complex and nonlinear processes involved. For example, clouds are formed when air is cooled or moistened to reach supersaturation, but the supersaturation level at which aerosol particles become activated to form cloud condensation nuclei (CCN) or ice nuclei varies with the size distribution, hygroscopicity, and chemical composition of aerosols [*McFiggans et al.,* 2006]. In addition, the composition and size distribution also affect the growth rate of clouds after the CCN have activated.

2.1.2.3 Major aerosol species

2.1.2.3.1 Dust

Dust is a major contributor to aerosol loading and optical thickness, especially in sub-tropical and tropical regions. As to 2000, estimates of its global source strength range from 1,000 to 5,000 Mt/yr. with high temporal and spatial variability. Dust source regions are mainly deserts, dry lakebeds, and semi-arid desert fringes, but also areas in drier regions where vegetation has been reduced or soil surfaces have been disturbed by human activities. Pure dust has a SSA ranging between 0.9 and 0.99 globally [*Claquin et al.,* 1999; *Shi et al.,* 2005; *Dubovik et al.,* 2002; *Mikami et al.,* 2006], and a radiative forcing of -0.1 ± 0.2 W/m^2 [*IPCC,* 2007].

2.1.2.3.2 Organic carbon (OC)

Organic carbon (OC) is a mixture of chemical compounds with carbon-hydrogen bonds. OC is produced from anthropogenic sources such as fossil fuel and biofuel burning and from natural source biogenic emissions. Organic aerosols are emitted as primary aerosol particles or formed as secondary aerosol particles from condensation of organic gases considered semi-volatile or having low volatility. Most types of OC are scattering aerosols, with weak absorption at ultraviolet and visible wavelengths [Bond et al., 1999; Jacobson, 1999; Bond, 2001)]; however, the absorbing abilities of OC vary greatly with organic composition, and the absorbing portion of organic aerosols often called brown carbon is currently under increased scrutiny [*Andreae and Gelencsér*, 2006] The estimated direct radiative forcing of OC is -0.05 ± 0.05 W/m^2 [*IPCC*, 2007]. Studies by *Gunthe et al*. [2009] and *Pöschl et al.* [2009] indicated that OC is slightly hygroscopic with a hygroscopicity parameter of ~0.1 and

is therefore less likely to be activated as Cloud Condensation Nuclei compared to other very hygroscopic aerosols such as ammonium sulfate. However, other studies [*Chang et al.,* 2010; *Tritsche et al.,* 2011; and *Duplissy et al.,* 2011] found that the hygroscopicity of OC depends on its composition (i.e., O/C ratio) and oxidation due to aging. OC with a higher O/C ratio or undergoing chemical aging processes due to reactions with OH tends to be more hygroscopic.

2.1.2.3.3 Black Carbon

Black carbon (BC) is a primary aerosol emitted from incomplete combustion processes such as fossil fuel and biomass burning. Black carbon aerosol strongly absorbs solar radiation, and therefore shows positive radiative forcing of $+0.20 \pm 0.15$ W/m^2 globally [*IPCC,* 2007]. However, the calculation of a global radiative forcing for BC is complicated as the optical properties of BC change within a few hours of emission. Studies by *Haywood et al.* [2003] and *Abel et al.* [2003] show that aerosols emitted from biomass burning sources became less absorbing with time; the SSA increases from 0.85 for freshly emitted aerosols to 0.9 for aged aerosols. They conclude that the reason for the increase of SSA is the condensation of non-absorbing organic gases onto the BC.

2.1.2.3.4 Sulfate

Sulfate is formed by aqueous phase reactions within cloud droplets, oxidation of SO_2 via gaseous phase reactions with OH, and by condensational growth onto pre-existing particles. As the major precursor of sulfate, SO_2 is mainly emitted from fossil fuel burning. Recently, emissions of SO_2 have decreased over developed nations such as

the US (6.2% yr^{-1} reduction from 2001 to 2010 [*Hand et al.,* 2012]) and Europe (from 55 Tg yr^{-1} in 1980 to 15 Tg yr^{-1} in 2004 [*Vestreng et al.,* 2007]). On the other hand, SO_2 emissions in developing countries are increasing or just beginning to decrease. For example, due to an annual growth rate of 7.3%, total SO_2 emissions in China increased from 21.7 Tg to 33.2 Tg (53%) from 2000 to 2006 but are now decreasing due to wide spread installations of flue-gas desulfurization devices in power plants [*Lu et al.,* 2010].

Sulfate is essentially a scattering aerosol across the solar spectrum ($\omega_o = 1$) with only a small degree of absorption [*Penner et al.,* 2001]. The estimated direct radiative forcing of sulfate is -0.4 ± 0.2 W/m^2 [IPCC, AR4]. Sulfate aerosols are very hygroscopic, with a hygroscopic parameter of 0.65, and are thus more likely to be activated as CCN compared to OC, BC and dust.

2.1.2.3.5 Nitrate

Nitrate aerosols are mainly ammonium nitrate. Atmospheric ammonium nitrate aerosol forms under the situation that sulfate aerosol is fully neutralized and there is excess ammonia. Nitrates are basically non-absorbing aerosols, with a direct radiative forcing of -0.1 ± 0.1 W/m^2 [*IPCC,* 2007].

2.2 EAST-AIRE campaign

The 2005 East Asian Studies of Tropospheric Aerosols: an International Regional Experiment (EAST-AIRE) campaign was conducted in China to study the properties of aerosols and their precursors, and gain insights into the aerosol direct and indirect effects on radiation, clouds, precipitation, atmospheric circulation, and the

environment [*Li et al*., 2007b]. An Intensive Observation Campaign (IOC) for EAST-AIRE was conducted at Xianghe Observatory near the Beijing metropolitan area in March 2005 (Figure 2.3). The Xianghe Atmospheric Observatory (39.798°N, 116.958°E; 35 m above sea level) is located in a rural area about 70 km southeast of the Beijing, the capital of China with population of ~19.6 million, and 80 km northwest of Tianjian, the fourth most populated city in China with a population of ~15 million. While sitting between two megacities, this area is characterized by agricultural land, relatively dense residential areas and light industry. Therefore, the site experiences frequent pollution plumes with urban, rural, or mixed origins, depending on the wind direction. Trace gases (O_3, CO, SO_2, NO and NO_y), aerosol optical properties and radiation fluxes were measured at this site. A 32-m meteorological tower located 50 m southeast of the observatory provided continuous measurements of ambient temperature, relative humidity, and wind speed at five levels (2, 4, 8, 16, and 32 m above ground) every 10 min. A wind vane at the top of the tower determined the wind direction, and a barometer monitored local atmospheric pressure from March 2, 2005 to March 26, 2005 [*C. Li et al*., 2007]. High loadings of carbon monoxide (CO), sulfur dioxide (SO_2), NO_y, and aerosols were observed during the campaign with large fluctuations due to synoptic processes [*C. Li et al*., 2007]. *Xia et al*. [2007a] calculated the aerosol direct radiative forcing on surface shortwave radiation at Xianghe observatory using an empirical equation to relate observed AOD to surface shortwave radiation and found an annual diurnal mean of -32.8 W/m^2 in 2005.

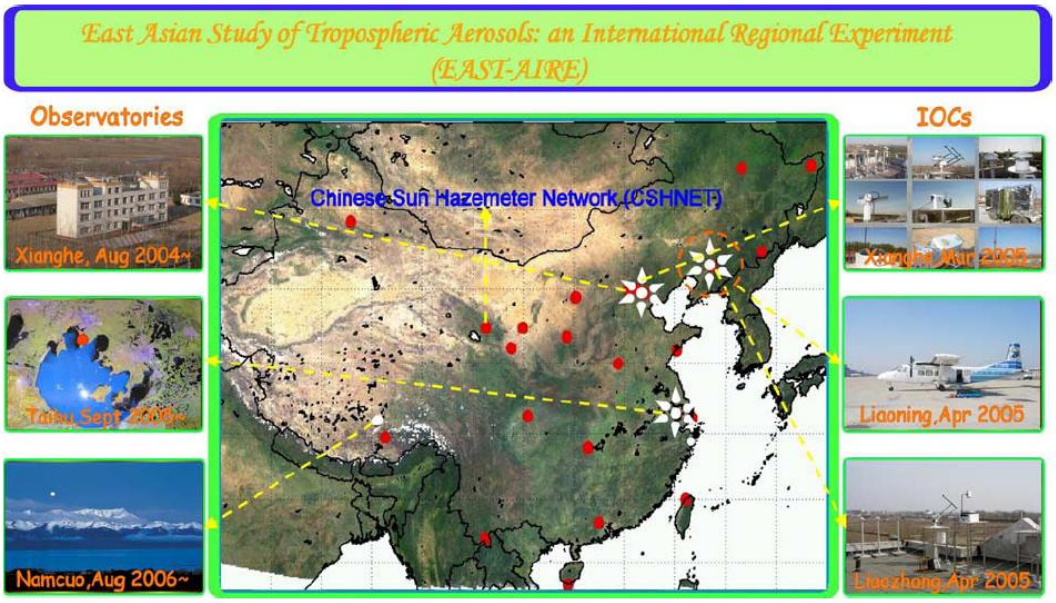

Figure 2.3. Overview of observational activities conducted under the auspices of the EAST-AIRE, including a nationwide aerosol observation network, Chinese Sun Hazemeter Network (CSHNET), observatories with extensive instrumentation, and intensive observation campaigns (IOC). Figure taken from *Z. Li et al*. (2007b).

2.3 WRF-Chem model

2.3.1 Overview

The Weather Research and Forecasting (WRF) model is a next generation mesoscale meteorological model that has been developed collaboratively among several agencies (http:// www.wrf-model.org). WRF is a nonhydrostatic model and includes several options for dynamic cores and physical parameterizations so that it can be used to simulate atmospheric processes over a wide range of spatial and temporal scales [*Skamarock et al*., 2005]. WRF-Chem [*Grell et al*., 2005] is a version of WRF

that also simulates trace gases and particulates simultaneously with the meteorological fields using the mass and scalar conserving flux form of the governing equations and a terrain-following mass vertical coordinate system.

2.3.2 Previous studies using WRF-Chem

Fully coupled regional models like WRF-Chem are widely used to investigate aerosol direct and indirect effects. *Fast et al.* [2006] simulated urban- to regional-scale variations in trace gases, particulates, and aerosol direct radiative forcing in the vicinity of Houston over a 5 day summer period with WRF-Chem and evaluated the simulations with measurements obtained during the 2000 Texas Air Quality Study. They performed simulations with and without aerosols. They calculated radiative forcing by taking the difference between received shortwave flux at the surface between the two simulations. They then compared the results with observations. The "observed" radiative forcing in their work was defined as the difference between the shortwave flux measured by the MFRSR (Multifilter Rotating Shadowband Radiometer) at ground level and simulated by the SBDART (Santa Barbara DISORT Atmospheric Radiative Transfer) model for a "pristine" atmosphere (no aerosols). The magnitude of the simulated aerosol radiative forcing was 10 to 50 W/m^2 less than observed likely due to an underestimation of column optical depth. *Fast et al.* (2006) concluded that there are several factors that may contribute to the under prediction of AOD. First, the particulate concentration profile used as initial and boundary conditions had a very low AOD of ~0.16. Second, the simulated wind field from this study had a considerable high bias that could lead to excessive transport of aerosols away from the observation site. Third, the model tended to be drier than

observations, which lead to lower aerosol water content and consequently lower AOD. The fourth possible factor is the lack of secondary organic aerosols in the modal aerosol scheme used in the model.

Yang et al. [2011] assessed how well v3.3 of WRF-Chem coupled with the Morrison double-moment microphysics scheme simulated boundary layer structure, aerosols, stratocumulus clouds, and energy fluxes over the Southeast Pacific Ocean. They conducted two sensitivity simulations, one with fixed cloud droplet number concentrations in the microphysics scheme (METO), and the other one with prognostic aerosol-cloud interaction (AERO). Cloud optical and microphysics properties simulated by AERO showed better agreements with observations than METO, showing the importance of coupling prognostic aerosols to the microphysics scheme, and the encouraging ability of a fully-coupled regional model to simulate mesoscale clouds.

2.3.3 Model configuration

In this study, the model domain covers most of East Asia with a horizontal resolution of 36 km (Figure 2.4) or 12 km (Figure 2.5), and 32 vertical layers from the surface to 100 hPa with 14 layers in the lowest 2 km. We use WRF-Chem Version 3.3 with the physics options that are mainly based on some previous studies [*Fast et al.,* 2006; *Yang et al.,* 2011] listed in Table 2.1.

The major chemical mechanisms used are the Carbon Bond Mechanism- Z (CBM-Z) photochemical mechanism *[Zaveri and Peters*, 1999] and Model for Simulating Aerosol Interactions and Chemistry (MOSAIC). CBMZ contains 55 prognostic species and 134 reactions, and uses a lumped structure approach to condense organic

species and reactions. It is an updated version of the widely used Carbon Bond Mechanism (CBM-IV) that also includes additional long-lived species and their intermediates and treats explicitly less reactive paraffins such as methane and ethane. MOSAIC uses a sectional approach, which divides the aerosol size distribution into 8 discrete size bins (see Table 2.2 for the 8 bins from MOSAIC), defined by their lower and upper dry particle diameters. Aerosols in each bin are assumed to be internally mixed, so that all particles within a bin are assumed to have the same chemical composition. Aerosol types included in MOSAIC are sulfate, nitrate, ammonium, chloride, sodium, other (unspecified) inorganics, organic carbon (OC) and black carbon (BC). Dry deposition of aerosol number and mass is based on *Binkowski and Shankar* [1995] and is calculated using the wet size of particles. Coagulation, nucleation, and secondary organic aerosol (SOA) formation processes are not included in MOSAIC in this version of WRF-Chem. The Fast-J photolysis scheme is modified to include the effect of prognostic aerosols and applied to calculate photolysis rates of chemical species (See Appendix for details).

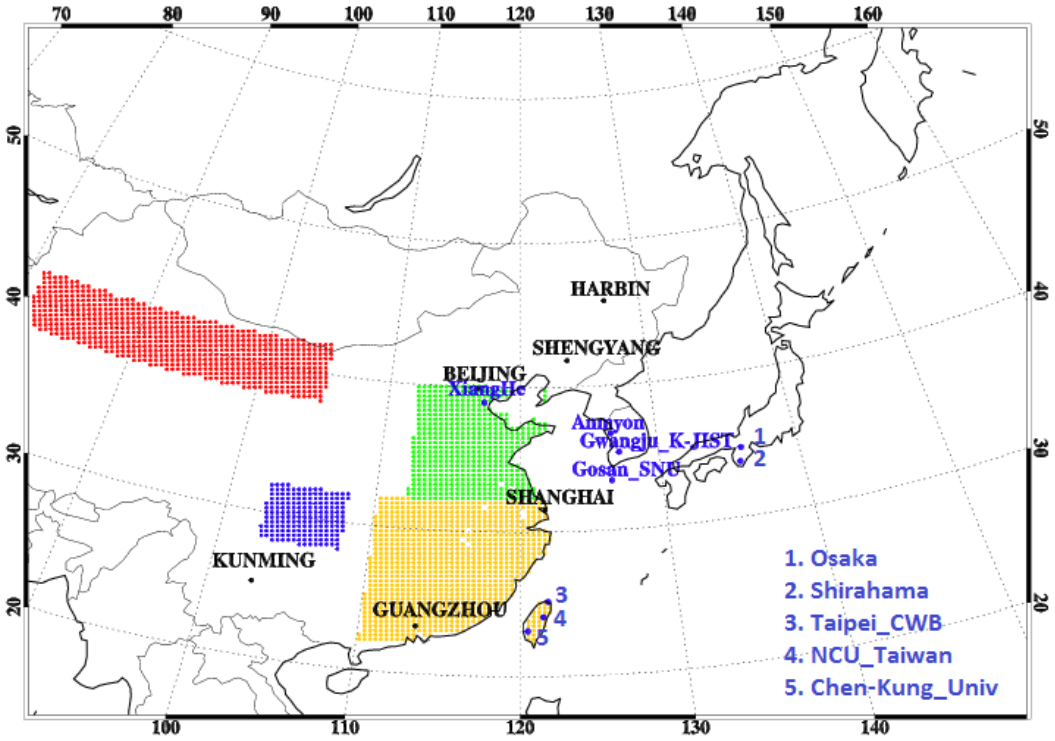

Figure 2.4. Domain of WRF-Chem simulation and analysis with 36 km horizontal resolution (within rectangle, 179 grid cells from west to east and 149 grid cells from south to north). Shaded regions of interest: Western China (Red, 38˚N~42˚N, 81˚E~105˚E), Sichuan Basin (blue, 26˚N~34˚N, 97˚E~108˚E), Southern China (yellow, 22˚N~32˚N, 110˚E~122˚E), and Eastern China (green, 32˚N~40˚N, 112˚E~122˚E). World Radiation Data Center (WRDC) stations in black, and AErosol RObotic NETwork (AERONET) stations in blue.

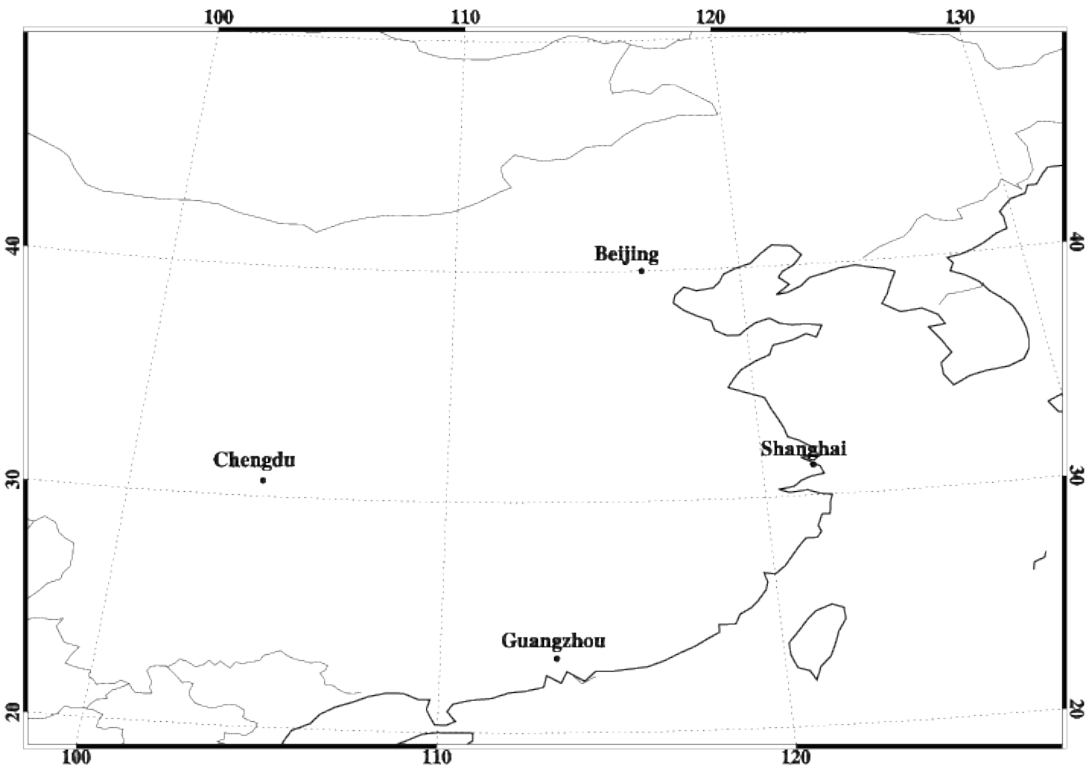

Figure 2.5. Domain of WRF-Chem simulation and analysis with 12 km horizontal resolution (within rectangle, 249 grid cells from west to east and 279 grid cells from south to north).

Table 2.1. Configuration of WRF-Chem (V3.3) model

Longwave radiation	Rapid Radiative Transfer Model (RRTM) [*Mlawer et al*., 1997]
Shortwave radiation	Goddard [*Chou and Suarez*, 1994]
Land surface	NOAH [*Chen and Dudhia*, 2001]

Surface Layer	QNSE [*Sukoriansky* et al., 2005]
Boundary layer	QNSE [*Sukoriansky* et al., 2005]
Cumulus clouds	Grell 3D [*Grell and Devenyi*, 2002]
Cloud microphysics	Morrison [*Morrison et al*., 2009]
Gas phase chemistry	CBM-Z [*Zaveri and Peters*, 1999]
Aerosol module	MOSAIC 8 bins [*Zaveri et al*., 2008]
Photolysis	Fast-J [*Barnard et al*., 2004; *Wild et al*., 2000]

Table 2.2. Size bins for MOSAIC in this work

Bin	1	2	3	4	5	6	7	8
Lower Diameter (μm)	0.04	0.08	0.16	0.31	0.62	1.25	2.5	5.0
Upper Diameter (μm)	0.08	0.16	0.31	0.62	1.25	2.5	5.0	10.0

2.3.4 Model input datasets

2.3.4.1 Initial and Boundary conditions

Initial conditions, boundary conditions, and time dependent sea surface temperatures (SSTs) were obtained from Global Forecast System (GFS) output archived on the National Center for Atmospheric Research (NCAR) Computational Information Systems Laboratory (CISL) Research Data Archive [http://rda.ucar.edu/datasets/ds083.2/]. Analysis nudging is not applied in order to

allow for feedbacks between aerosols, radiation, and meteorology. The Model for Ozone and Related chemical Tracers (MOZART) [*Emmons et al.*, 2010] provided the initial and boundary conditions for trace gases and aerosols [http://www.acd.ucar.edu/wrf-chem/mozart.shtml].

2.3.4.2 Emission inventories

The anthropogenic emission inventory used in this work was developed by *Zhang et al* [2009] for the year 2004-2005 with a horizontal resolution of 0.5°×0.5°. It was prepared for the Intercontinental Chemical Transport Experiment-Phase B (INTEX-B) in 2006 [*Singh et al*., 2009] and includes emissions for eight major species: SO_2, NO_x, CO, PM_{10}, $PM_{2.5}$, BC, OC and non-methane volatile organic compounds (NMVOC). The emissions for inorganic species are divided into four sectors: industry, transportation, power plant, and residential. Table 2.3 shows the total emissions of these 8 species for each emission sector in the domain described in Figure 2.4. Emissions for anthropogenic NMVOC species are speciated based on the RADM2 chemical mechanism, converted into species used by CBMZ, and grouped into categories of biofuel burning, fossil fuel burning, industry, transportation, and power plant. Emissions from industry, transportation and residential are put into the surface layer, and power plant emissions are put in the level that includes 200 meters. Since NH_3 emissions are not available from the INTEX-B emission inventory, data with 0.25˚×0.25˚ horizontal resolution from MICS Asia 2008 emission inventory are used [*Huang et al.,* 2012].

Table 2.3. Total emissions for WRF-Chem domain (Gg/year)

	Industry	Power Plant	Transportation	Residential	Total
CO	82050.3	2511.1	48853.1	68768	202182.5
SO_2	11628.6	20031.6	481.2	3179.3	35320.7
NO_X	7013	10391.7	8497.3	1452.4	27354.4
BC	609.9	39.5	309.4	1184.8	2143.6
OC	525.9	7.5	160.3	3377.4	4071.1
$PM_{2.5}$	7422.2	1693.5	649.9	5880.9	15646.5
PM_{10}	11241.7	2837.5	751.2	6458.4	21288.8

Biomass burning emissions of CO, NO_x, other carbon compounds and particulate matter are obtained from the Global Fire Emissions Database (GFED) Version 3.1 with a spatial resolution of 0.5°×0.5° degrees and a temporal resolution of 1 day [*van der Werf et al.*, 2010; *Mu et al*., 2010]. Compared with the anthropogenic CO emissions (Figure 2.6a), CO from biomass burning (Figure 2.6b) is much more intense over South Asia and will have huge local impacts on surroundings.

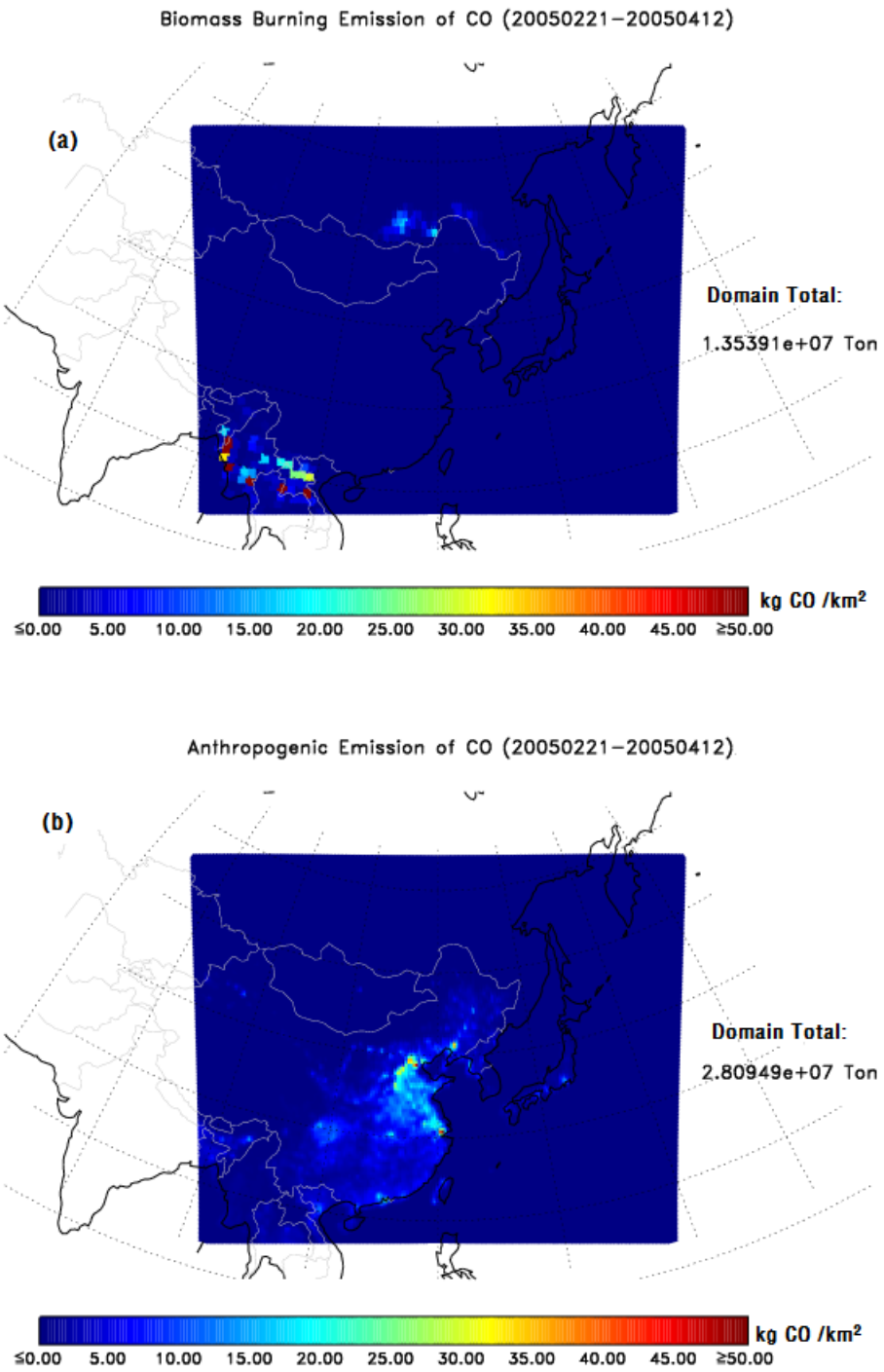

Figure 2.6. CO emissions from (a) anthropogenic sources and (b) biomass burning.

Biogenic VOC (BVOC) emissions account for ~90% of global VOC emissions annually [*Guenther et al*., 1995]. BVOC emissions are important during March in the southern portion of our modeling domain. We simulated these emissions using v2.04 of the Model of Emissions of Gases and Aerosols from Nature (MEGAN) [*Guenther et al.,* 2006] that is a standard component of v3.3 WRF-Chem. MEGAN v2.04 is driven by land cover information from NCAR (http://www.acom.ucar.edu/wrf-chem/download.shtml) and meteorological variables from the prognostic WRF-Chem simulation.

We use the GOCART dust scheme [Ginoux et al., 2001] that is coupled to the standard WRF-Chem v3.3, to calculate the dust emissions flux:

$$G = C * S * s_p * u_{10m}^2 * (u_{10m} - u_t)$$

where C is an empirical proportionality constant, S is a source function that is defined as the probability of dust uplifting in a given area and is proportional to the erosion factor (Figure 2.7), s_p is the fraction of each size class of dust in the emissions, u_{10m} is the horizontal wind speed at 10 m, u_t is the threshold wind velocity below which dust emissions do not occur and is a function of particle size, air density, and surface moisture.

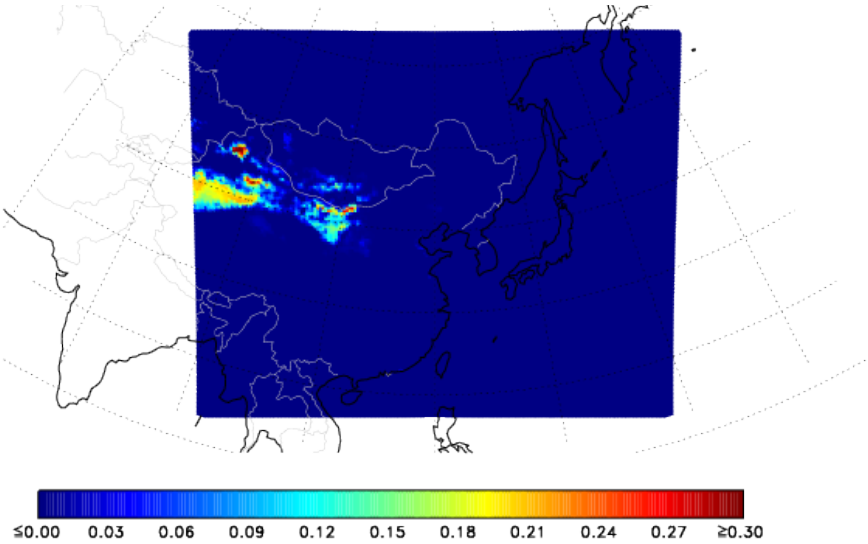

Figure 2.7. Erosion Fraction from WRF geographical input files that is used in WRF-Chem to calculate dust emissions [*Ginoux et al*., 2001].

2.4 Observational datasets

Besides observations made at Xianghe Observatory, WRF-Chem model simulations are also evaluated against several observational datasets, such as weather station observations, MODIS aerosol / cloud optical properties, and OMI NO_2 columns.

2.4.1 Meteorological observations

Daily ground observations of the surface temperature and precipitation from 743 stations across China [*Li et al.*, 2009 and *Zhai et al*., 2005] are used to evaluate the WRF-Chem simulation of surface temperature and precipitation.

2.1.2 MODIS

The Moderate Resolution Imaging Spectroradiometer (MODIS) instruments aboard NASA's Terra and Aqua satellites, with overpass times at 10:30 AM and 1:30 PM local time, respectively, are making near-global daily observations of the Earth in a wide spectral range (0.41–15 μm) [*Remer et al.,* 2003]. Spectral AOD and aerosol size parameters are routinely derived from these measurements. Level 2 MODIS Terra and Aqua data with 10 km spatial resolution (https://modis-atmos.gsfc.nasa.gov/MOD04_L2/, collection 5, deep blue retrieval algorithm) at the locations of AERONET stations obtained from **G**eospatial Interactive Online Visualization ANd aNalysis Infrastructure (GIOVANNI) [http://giovanni.gsfc.nasa.gov/aerostat/] over the study region are used to evaluate the model simulation of AOD.

2.1.2 OMI

Tropospheric NO_2 columns from Ozone Monitoring Instrument (OMI) are obtained from version 2 of the "Derivation of OMI tropospheric NO_2" project (DOMINO) [*Boersma et al*., 2011]. The OMI instrument has a 13× 24 km spatial resolution at nadir and produces global coverage over cloud-free locations in one day [*Levelt et al*., 2006].

2.1.3 AERONET

The AERONET (AErosol RObotic NETwork) program [*Holben et al.,* 1998] is a ground-based remote sensing aerosol network that provides a long-term, continuous

and globally distributed observation data of aerosol optical, microphysical and radiative properties, which can be used for aerosol research and satellite validation.

2.1.4 WRDC

WRDC (World Radiation Data Center) is sponsored by the World Meteorological Organization (WMO) to collect and archive solar radiation data collected at over 1000 measurement sites worldwide. The WRDC archive contains the following measurements: global solar radiation, diffuse solar radiation, downward atmospheric radiation, sunshine duration, direct solar radiation (hourly and instantaneous), net total radiation, net terrestrial surface radiation (upward), terrestrial surface radiation, reflected solar radiation, and spectral radiation components (instantaneous fluxes), although not all the measurements are made at all sites. The data is available for download from http://wrdc.mgo.rssi.ru/wrdc_en_new.htm.

Chapter 3: Impact of Aerosol Direct Effect on East Asian Air Quality

3.1 Introduction

3.1.1 Previous studies

Solar radiation is the major driver of tropospheric photochemistry through its impact on photolysis rates. Ozone among all the absorbing gases in the troposphere is the most sensitive to changes in shortwave radiation due to aerosols [*Liu and Trainer*, 1988; *Thompson et al*., 1989; *Madronich and Grainer*, 1992; *Fuglestvedt et al*., 1994; *Ma*, 1995]. Therefore, the increasing aerosol loading in China [*Hsu et al.,* 2012] substantially influences concentrations of tropospheric ozone, a major air pollutant that is also harmful to human health. With the Sulfur Transport and Emissions Model (STEM), *Tang et al*. [2004] found that surface ozone concentrations were reduced by 0.1% to 0.8% in northeastern China during the dust event of April 4 ~14, 2001 due to dust-induced changes in photolysis rates [*Seinfeld and Pandis*, 2006]. *Tie et al*. [2005] showed that with aerosols included in the radiation/photolysis scheme, surface-layer photolysis rates of $j(O_3)$ and $j(NO_2)$ in eastern China were reduced, respectively, by 20 to 30% and 10 to 30% in winter as well as 5 to 20% and 1 to 10% in summer, leading to reductions in surface-layer ozone concentrations of 2 to 4% in winter and minimal changes in summer. The formation rate of secondary aerosols, i.e., sulfate aerosol, is related to the abundance of the precursor gas (SO_2) and atmospheric oxidants such as hydroxyl radical (OH), hydrogen peroxide (H_2O_2),

ozone (O_3), methylhydroperoxide (MHP) and peroxyacetic acid (PAA) [*Seinfeld and Pandis*, 2006]. These atmospheric oxidants are formed via photochemical processes that are influenced by the ADE. ADE-induced changes that affect air quality not only include changes in chemistry, but also include changes in meteorology. *Forkel et al*. [2012] studied changes in ozone and PM triggered by aerosol direct and indirect effects and found that mean surface ozone mixing ratios over continental Europe were increased by 10% mainly from the change in cloud cover due to both the semi-direct effect and indirect effect. PM_{10} (Particulate Matter up to 10 micrometers in size) was decreased by 2-5 $\mu g\ m^{-3}$ (20-50%) when only the direct and semi-direct effects were included. *Wang et al* [2015] investigated haze episodes in July 2008 over Jing-Jin-Ji and surrounding regions of China (Beijing, Tianjin, Hebei, East Shanxi, West Shandong and North Henan) and showed that aerosol direct radiative forcing decreased the flux of solar radiation at the surface by more than 15% over most of the region leading to a 14% increase in surface $PM_{2.5}$ due to ADE-related changes in meteorological conditions.

3.1.2 Experiment setup

WRF-Chem is widely used to relate the emissions of aerosols and their precursors to aerosol formation, growth and transport, and ultimately to study their impact on air quality, radiative balance, and the regional climate. *Fast et al*. [2006] simulated trace gases, PM, and aerosol direct radiative forcing in the Houston area over a 5-day summer period and found that the simulated surface shortwave radiation was closer to observations with the high bias reduced by up to 50% when the ADE was included in the shortwave radiative transfer scheme. In this chapter, we apply WRF-Chem with

the configuration shown in Table 2.1 in the domain covering most of East Asia shown in Figure 2.4 with horizontal resolution of 36 km, and simulate the impact of ADE on meteorology and chemistry during EAST-AIRE IOC period (March 1 to March 30, 2005). Two WRF-Chem experiments (Table 3.1) were conducted to investigate the effects of the ADE: 1) All aerosol effects are included (Base); 2) aerosol direct effect is removed (Base_No_ADE). We evaluate the meteorological conditions, trace gas concentrations, and aerosol properties simulated from the Base case with observations. The total aerosol radiative forcing can be decomposed into three components: direct radiative forcing, cloud radiative forcing, and surface albedo forcing [*Ghan*, 2013]. In this study, the first term, was determined by subtracting the results from the Base_No_Ade simulation that did not pass aerosols to the Goddard shortwave radiation scheme from the Base simulation that passed prognostic aerosols to the shortwave scheme. The Goddard shortwave radiation scheme as configured for WRF-Chem V3.3 uses simulated aerosol and cloud optical information, fixed CO_2 (300 ppm), and prescribed ozone profiles. Interactions between prognostic aerosol and photolysis rates are included in the Fast-J module in the BASE case (see appendix). However no aerosols are passed to the Fast-J module in the Base_No_ADE case.

Table 3.1. Experiment setup

Base	Include both aerosol direct and indirect effects
Base_No_ADE	Include only aerosol indirect effect
SO_2×0.2	Same setting as Base with SO_2 emission reduced to 20% of INTEX-B values

BC×0.2	Same setting as Base with BC emission reduced to 20% of INTEX-B values

Because air quality is currently poor in much of China, we perform two additional sensitivity simulations to test the potential impact of pollutant emission regulations. Since sulfate and BC are different types of aerosols in terms of optical properties, i.e., scattering and absorbing, reducing the emissions of sulfate precursor (SO_2) and BC should have different effects. Therefore, we carried out two sensitivity simulations: a) SO_2 emissions reduced to 20% of INTEX-B emissions (SO_2×0.2), chosen based on the fractional change in SO_2 emissions between 2005 and 2050 from the IPCC Representative Concentration Pathways (RCP) 4.5 scenario [http://tntcat.iiasa.ac.at:8787/RcpDb/dsd?Action=htmlpage&page=welcome#intro], while emissions of other trace gases and PM are unchanged from INTEX-B; b) BC emissions reduced to 20% of INTEX-B emissions (BC×0.2), while emissions of other trace gases and PM are unchanged from INTEX-B. An 80% reduction of BC reduces Chinese BC emissions to approximately current US BC emissions. (see section 3.3). The difference between the reduced emission simulations and the Base simulation shows the impact of reducing pollutant emissions on radiation, meteorological variables and air quality.

3.2 Results and discussions

3.2.1 Model evaluation against observations

The meteorological fields from the Base case simulation agree well with surface temperature, pressure, wind fields and relative humidity observations at Xianghe Observatory (Figure 3.1). The temporal variations of modeled surface temperature, pressure and RH are well correlated with observations (correlation coefficient R = 0.7-0.9) and the wind speed is moderately correlated (R = 0.5) with observations, indicating that WRF-Chem can capture the evolution of synoptic systems passing Xianghe Observatory.

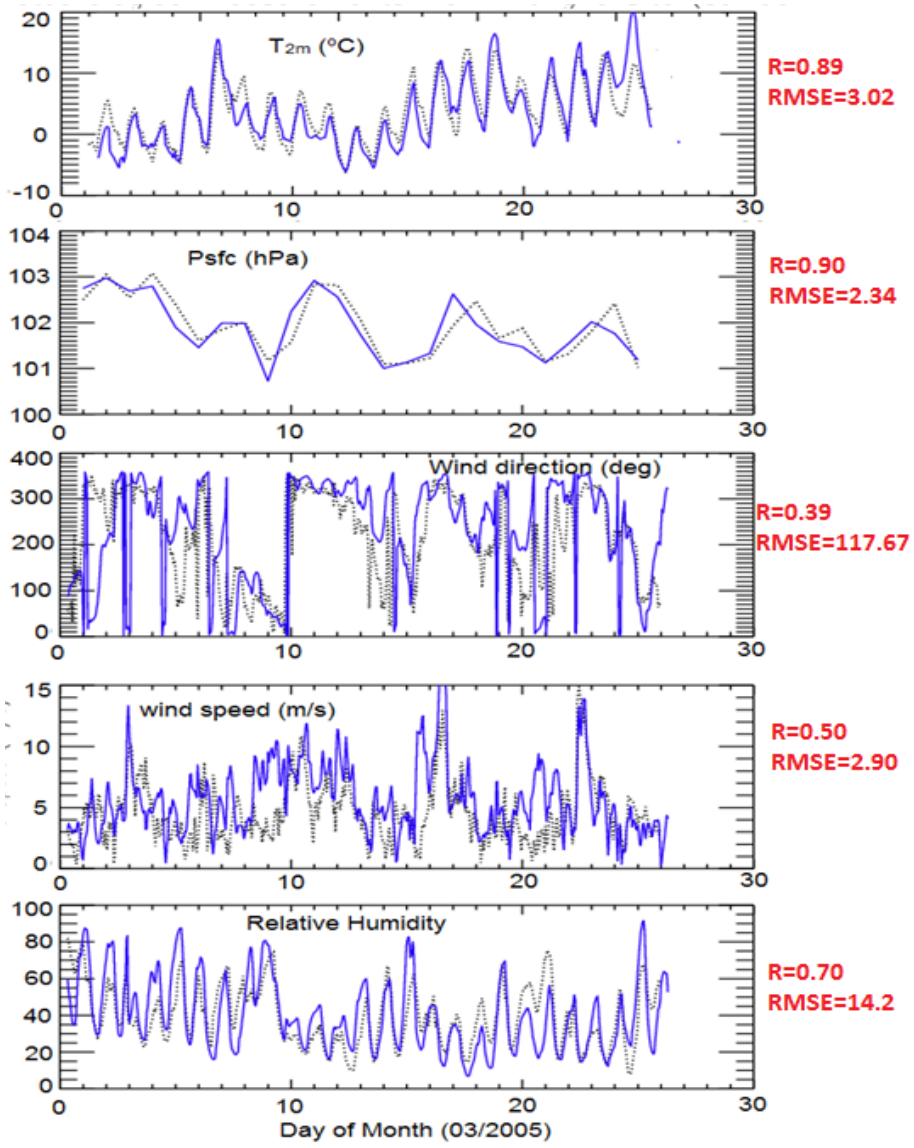

Figure 3.1. Comparison of meteorological variables: hourly surface temperature at 2 meters, daily average surface pressure, hourly surface wind speed, and hourly relative humidity from WRF-Chem simulation versus hourly averaged observations at Xianghe Observatory in March 2005 (black dots: observation; blue lines: model).

The monthly average 2-meter temperature simulated from Base case (Figure 3.8c) agrees well with observations (not shown in figure) from 743 meteorological stations

in China [*Li et al.,* 2009]. The average temporal correlation of the hourly values is 0.82 with about 70% of the station correlations exceeding 0.8. After the seasonal cycle is removed, the domain-wide average temporal correlation is still 0.75, indicating that the model captures the temporal evolution of surface temperature in most parts of China. The magnitudes for all the variables are reasonably reproduced, with biases less than 20%. We find that the simulated wind field is sensitive to the boundary layer physics, land use, and surface schemes used in the model. By changing the combination of land surface layer scheme and boundary layer scheme from the revised MM5 Monin-Obukhov scheme and YSU scheme [*Hong et al*., 2006], which are used by *Fast et al.,* [2006], to the Quasi–normal Scale Elimination (QNSE) land surface and boundary layer Scheme [*Sukoriansky et al.,* 2005], we reduced the high-biases in wind speed from 40% to 20%. We compared the March total precipitation with data from the Global Precipitation Climatology Project (GPCP). Figure 3.2 shows that the model does a reasonable job of reproducing the precipitation distribution with a spatial correlation of 0.66. However, the model does overestimate the precipitation in the whole domain with an average bias of 28%, although low biases (~ -13%) were found in southeast China.

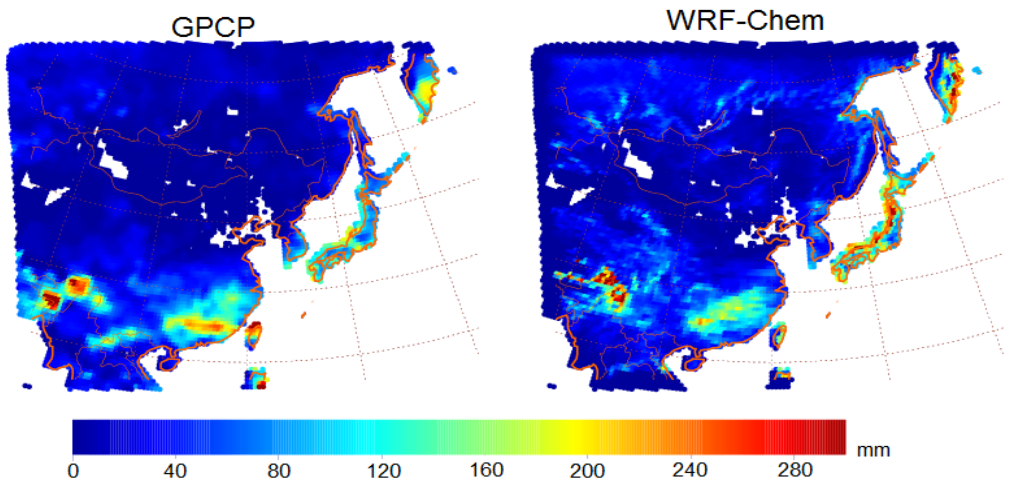

Figure 3.2. Comparison of total precipitation for March 2005 between WRF-Chem simulation and data from Global Precipitation Climatology Program (GPCP).

Hourly average trace gas measurements at Xianghe Observatory from the EAST-AIRE campaign were used to evaluate the performance of WRF-Chem (Figure 3.3). Temporal fluctuations of CO and SO_2 are moderately correlated with observations with substantial underestimation on highly polluted days. The underestimation of peaks is expected due to the relatively coarse resolution of both the emission inventory and the WRF-Chem simulation.

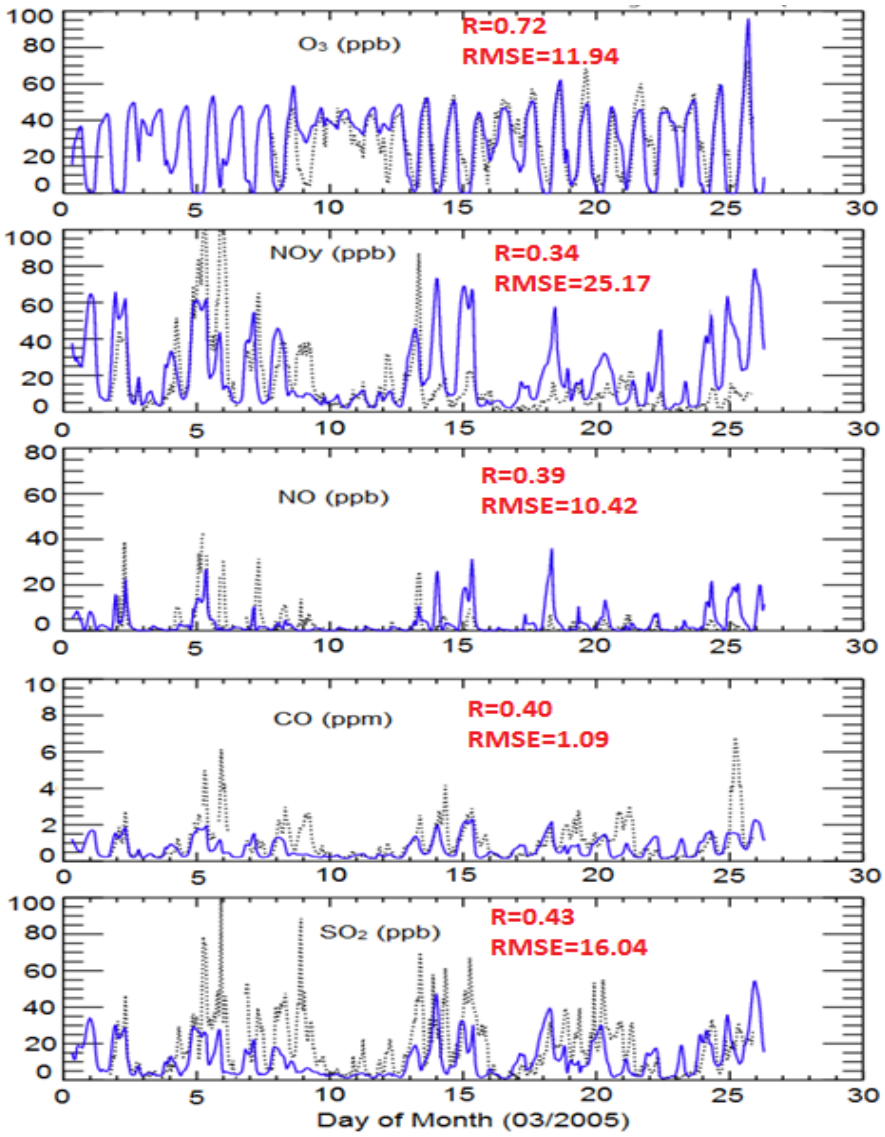

Figure 3.3. Comparison of hourly average trace gases: O_3 (a), NO_y (b), NO (c), CO(d), and SO_2 (e) from WRF-Chem simulation and observations at Xianghe Observatory from March 2 to March 26 (black dots: observation; blue lines: model).

Figure 3.4 shows the correlation between pollutant levels and wind speed and direction. The most frequent wind directions (Figure 3.4a) at Xianghe simulated by WRF-Chem are from the northwest quadrant (where Beijing is located), which is

consistent with the observations. However the model produces more strong winds from the north and northeast than observed. A portion of the low bias in CO is caused by the 20% overestimation of wind speeds and hence dilution during periods of stagnation. Based on the observed and modeled wind roses (Figure 3.4a), the frequency of easterly winds is underestimated by WRF-Chem. Consistently, most of the high CO mixing ratios (larger than 3ppm) observed at Xianghe (Figure 3.4b) occur when winds come from the east. Therefore, an underpredicted frequency of easterly winds in the model is another reason for the low bias of CO concentration at Xianghe. However, model CO amounts are low regardless of wind direction, indicating that there is likely a low bias in the CO emissions too. The model captures the diel cycles of ozone and NO. O_3 is well simulated starting on March 12th, while from March 9th to March 12th, WRF-Chem overestimates the nighttime ozone. This high bias in nighttime ozone is related to the underestimation of NO during these days, which slows down the ozone titration process. WRF-Chem underestimates NO levels for March 6th to March 12th, which is consistent with the low bias of CO and SO_2 during these days, after cold frontal passages on March 6th and March 9th [*Li et al., 2007*]. After the cold fronts, the wind speed is significantly overestimated, with biases approaching twice the monthly average bias.

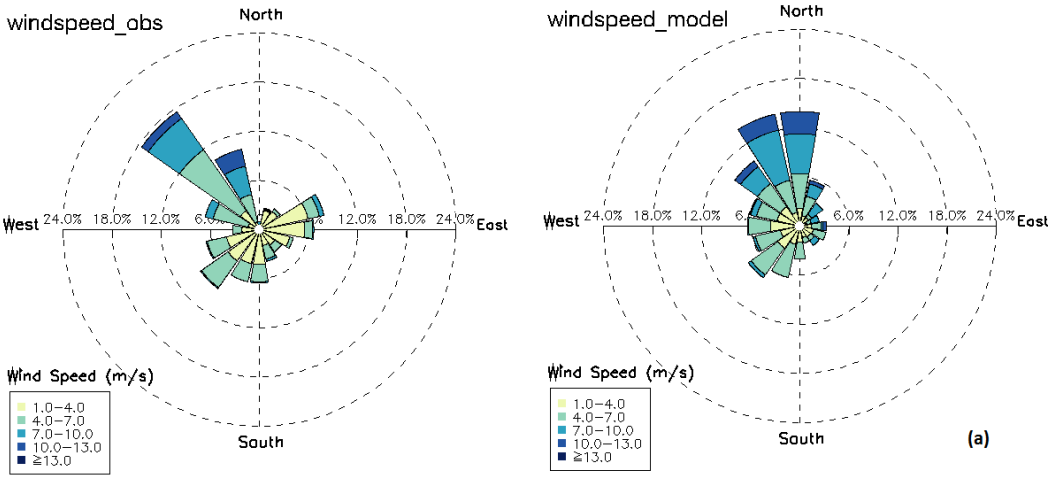
windspeed_obs
North
West
East
South
24.0% 18.0% 12.0% 6.0% 12.0% 18.0% 24.0%
Wind Speed (m/s)
1.0–4.0
4.0–7.0
7.0–10.0
10.0–13.0
≧13.0

windspeed_model
North
West
East
South
24.0% 18.0% 12.0% 6.0% 12.0% 18.0% 24.0%
Wind Speed (m/s)
1.0–4.0
4.0–7.0
7.0–10.0
10.0–13.0
≧13.0

(a)

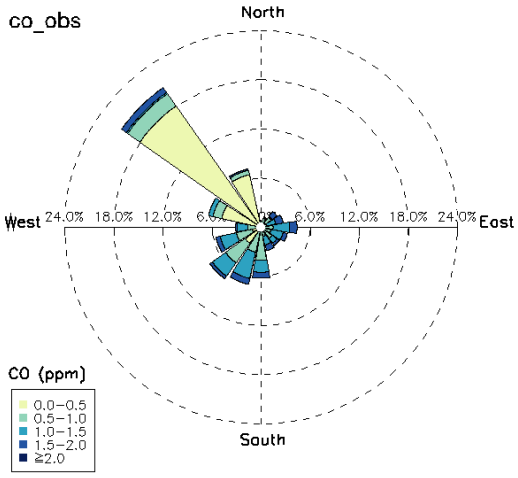
co_obs
North
West
East
South
24.0% 18.0% 12.0% 6.0% 12.0% 18.0% 24.0%
CO (ppm)
0.0–0.5
0.5–1.0
1.0–1.5
1.5–2.0
≧2.0

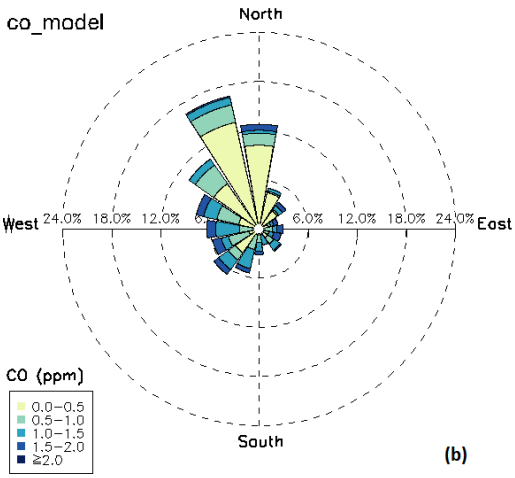
co_model
North
West
East
South
24.0% 18.0% 12.0% 6.0% 12.0% 18.0% 24.0%
CO (ppm)
0.0–0.5
0.5–1.0
1.0–1.5
1.5–2.0
≧2.0

(b)

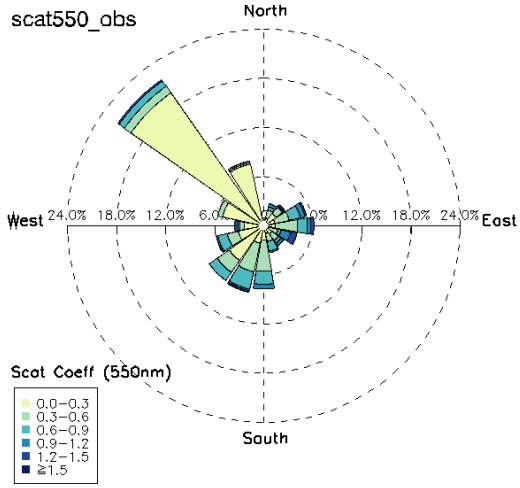
scat550_obs
North
West
East
South
24.0% 18.0% 12.0% 6.0% 12.0% 18.0% 24.0%
Scat Coeff (550nm)
0.0–0.3
0.3–0.6
0.6–0.9
0.9–1.2
1.2–1.5
≧1.5

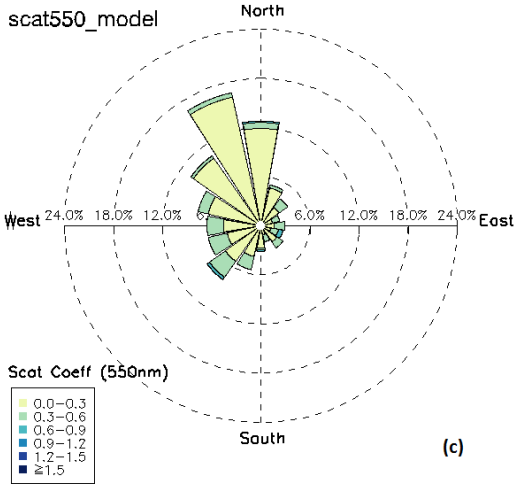
scat550_model
North
West
East
South
24.0% 18.0% 12.0% 6.0% 12.0% 18.0% 24.0%
Scat Coeff (550nm)
0.0–0.3
0.3–0.6
0.6–0.9
0.9–1.2
1.2–1.5
≧1.5

(c)

Figure 3.4. Comparisons of wind roses (a), CO roses (b) and scattering coefficient roses (c) at Xianghe Observatory from observations (left) and WRF-Chem (right). The length of each wedge shows the frequency that the wind comes from one of 16 directions. The colored sections of each wedge show the frequency the wind speed, CO mixing ratio, and scatter coefficient take on values shown in the legend.

Model output is compared to retrieved OMI tropospheric NO_2 columns for March 2005 in Figure 3.5. The domain wide spatial correlation between WRF-Chem and the DOMINO tropospheric NO_2 column is 0.85 with a mean bias of about 16%, demonstrating that the model can reproduce the spatial pattern and magnitude of tropospheric NO_2 column amounts with a small high bias. The high bias is mainly found in the Sichuan basin (southwest China), and eastern China. *Zhao et al*. [2009] estimated NO_x emissions from fossil fuel combustion in East Asia constrained by assimilated inversion of daily OMI tropospheric NO_2 columns in a Regional chEmical trAnsport Model (REAM). They found that the a posteriori NO_x emissions from the assimilated inversion are 13% lower than the a priori NO_x emissions (INTEX-B), which indicates that the NO_x emissions used in our work are biased high and likely explain a portion of the high biases in simulated NO and NO_2.

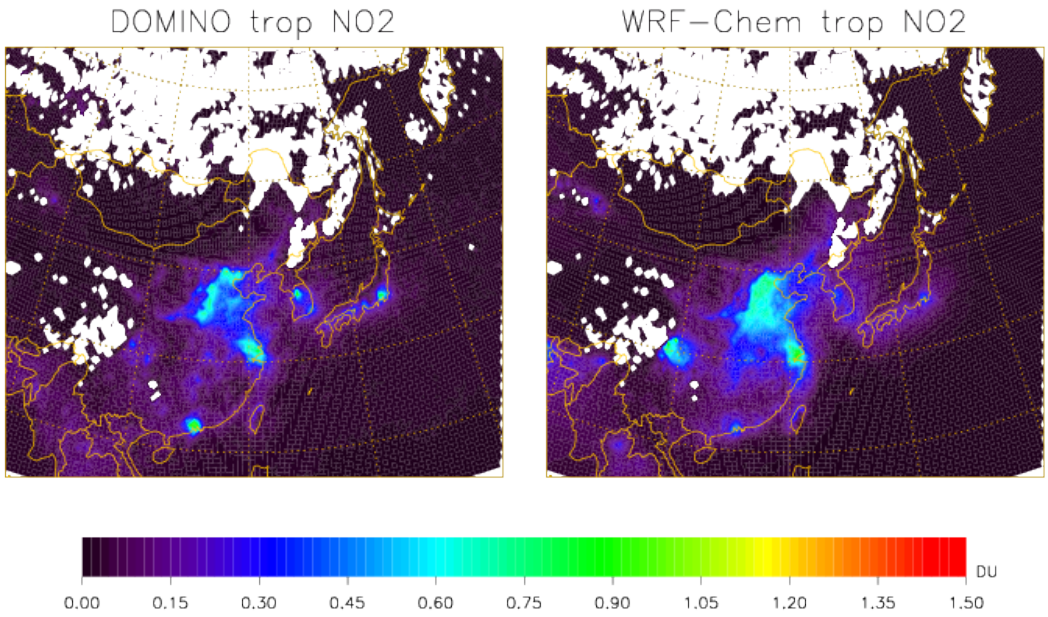

Figure 3.5. Monthly Mean tropospheric NO_2 from OMI DOMINO data (left) and WRF-Chem simulation AER_all (right) in March, 2005. (Unit, Dobson Unit, 1 DU = 2.69×10^{16} molecules/cm^2). The tropospheric NO_2 column is derived from DOMINO v2.0 retrieval algorithm [*Boersma et al*., 2011]. Level 2 data are used with the averaging kernel applied to the model.

The evaluation of simulated aerosol properties is shown in Figure 3.6. WRF-Chem is able to reproduce the buildup and decrease of aerosols (Figure 3.6a), however WRF-Chem tends to under-predict AOD on highly polluted days as indicated by observations. Comparing the aerosol absorption coefficient (Figure 3.6b) and scattering coefficient (Figure 3.6c), we found that the absorption coefficient shows better agreement with observations (although the model underestimates the peak values) than the scattering coefficient, indicating that the underestimation of AOD is mainly contributed by the underestimated aerosol scattering coefficient. A test run

with 5×SO_2 emissions enhances scattering coefficients at Xianghe by less than 10%, which indicates that the underestimated scattering coefficients are not caused by a low bias in emissions of the sulfate precursor. The low relative humidity in this region during March leads to the low sensitivity of the scattering coefficient to the emissions of the sulfate precursor since the formation of sulfate via aqueous chemistry is suppressed. We conduct a scattering coefficient rose analysis, similar to CO (Figure 3.4), and find that WRF-Chem underestimates scattering coefficients in all directions, suggesting that the potential sources of the bias not only include the bias in wind field but also include the large uncertainty of the anthropogenic OC emissions (±258%) from INTEX-B emission inventory [*Zhang et al.,* 2009].

The lack of secondary organic aerosol (SOA) formation in WRF-Chem 3.3 may also contribute to the low bias in aerosol scattering coefficient, scattering coefficient, aerosol optical depth, and single scattering albedo and affect the radiation budget [*Fast et al.*, 2006]. *Jiang et al.* [2012] studied seasonal and spatial variations in SOA concentrations over China in 2006 using WRF-Chem coupled with the secondary organic aerosol model (SORGAM) and an additional SOA module that accounts for SOA formation from isoprene. As in our work, their study used the INTEX-B emission inventory for anthropogenic VOC emissions and MEGAN model coupled with WRF-Chem for biogenic VOC emissions. Thus our SOA concentrations would likely be similar to theirs if we used a version of WRF-Chem that included SOA formation. They found that the mean surface concentration of total SOA over China in spring was 0.94 $\mu g/m^3$, which was 37% of the mean summertime SOA concentration. The mean concentration in early spring was even lower.

Anthropogenic sources were responsible for 41% of the springtime SOA, while biogenic sources were responsible for 59% of the SOA. In our simulation, the mean $PM_{2.5}$ concentration over China was 46.3 $\mu g/m^3$ suggesting that in a mean sense SOA may have comprised a small percent (2%) of total $PM_{2.5}$. However, recent observations indicate that SOA and anthropogenic SOA in particular play an important and "not yet widely recognized" role in urban wintertime haze events [*Huang et al*., 2014] contributing 30% to 77% of total $PM_{2.5}$ in Beijing, Shanghai, Guangzhou, and Xi'an during severe haze events in January 2013. In summary, the lack of a SOA module in v3.3 of WRF-Chem is not a showstopper as SOA concentrations are usually relatively small during the early spring; however, it is a weakness that must be considered when interpreting results, especially during intense haze events.

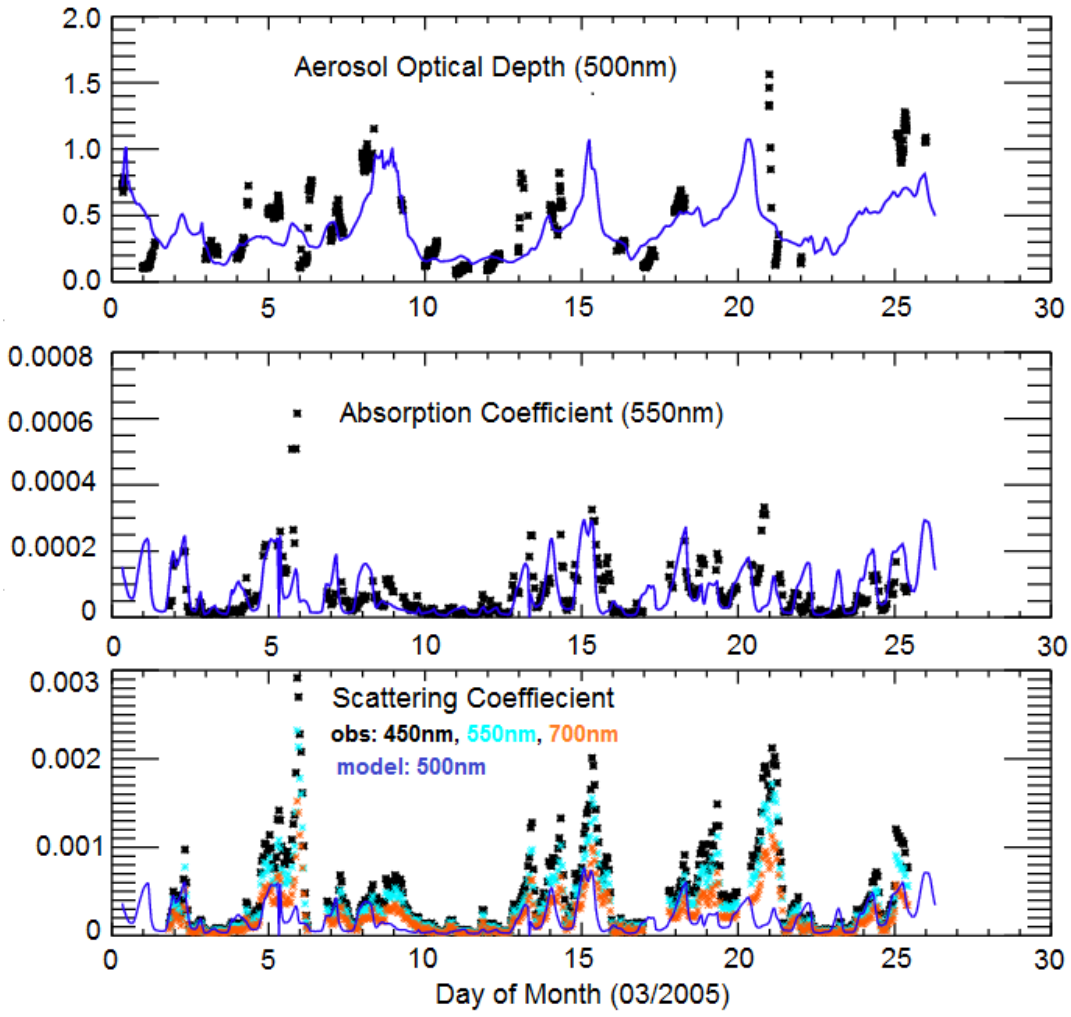

Figure 3.6. Comparison of aerosol properties: AOD (a), absorption coefficient at 550 nm (b), and scattering coefficient (c) from hourly WRF-Chem simulation outputs (dark blue lines) and observations (symbols) at Xianghe Observatory from March 2 to March 26. Observed absorption coefficient and scattering coefficient are hourly averaged from EAST-AIRE IOC data.

In addition, we evaluate the WRF-Chem simulated AOD with AERONET measurements and MODIS Terra and Aqua at the locations of AERONET sites (Figure 3.7). The correlation between MODIS and AERONET observations are

above 0.86 at these stations. The comparison shows that WRF-Chem captures the temporal variation moderately well with correlations (AERONET and MODIS combined) higher than 0.5 at 8 out of 10 stations. WRF-Chem simulated AOD values are also close to AERONET and MODIS values, demonstrating the ability of WRF-Chem to simulate the aerosol loading. In general, the model slightly underestimates AOD with respect to AERONET (Table 3.2), with biases less than 30% at 7 stations. Low-biases are largest in urban areas on highly polluted days (AOD > 1) suggesting that the model is unable to capture local peaks due to its coarse spatial resolution. On the other hand, WRF-Chem overestimates the aerosol loading at the coastal rural site Gosan_SNU (Table 3.2).

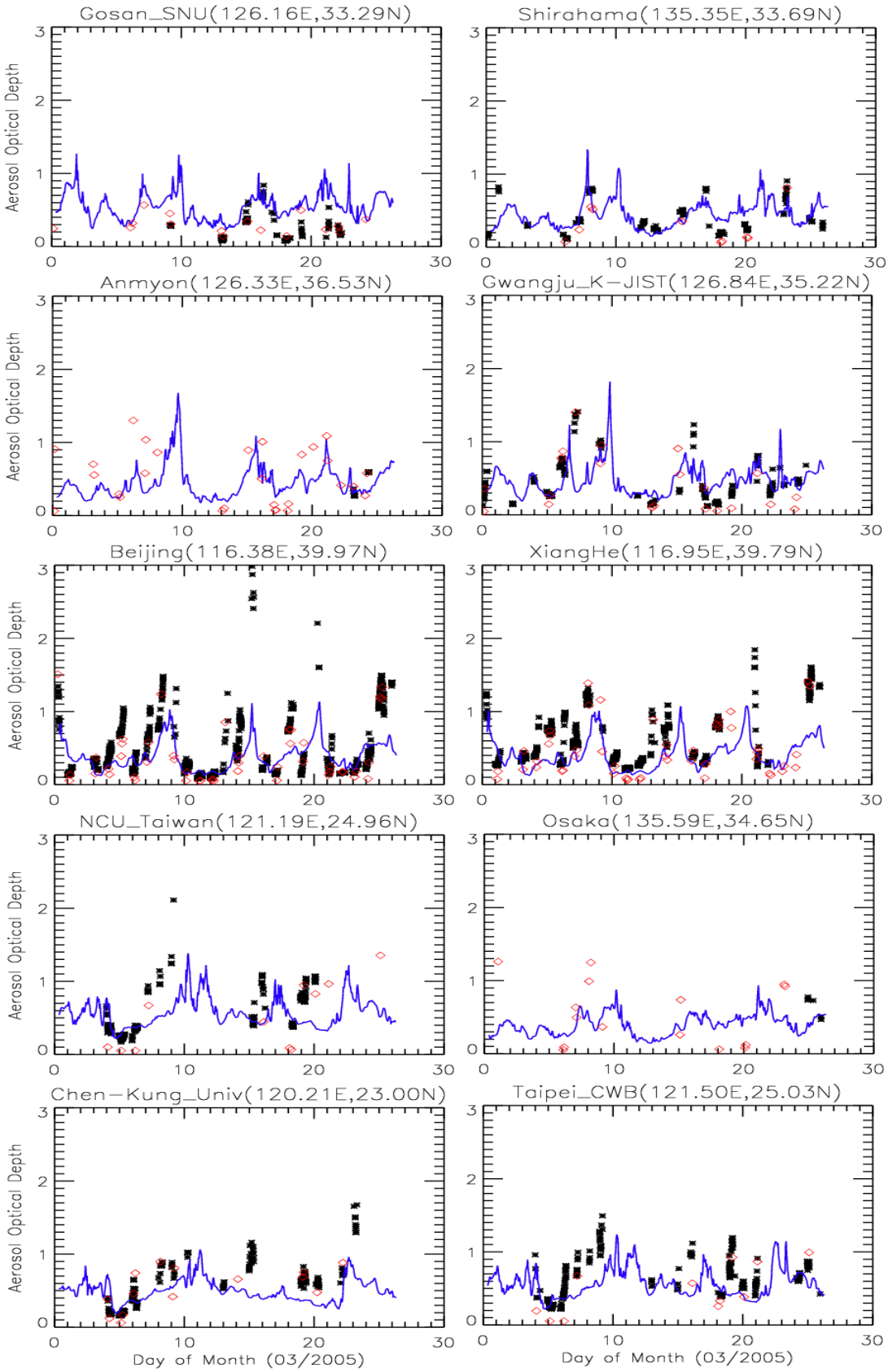
Gosan_SNU(126.16E,33.29N)
Shirahama(135.35E,33.69N)
Anmyon(126.33E,36.53N)
Gwangju_K-JIST(126.84E,35.22N)
Beijing(116.38E,39.97N)
XiangHe(116.95E,39.79N)
NCU_Taiwan(121.19E,24.96N)
Osaka(135.59E,34.65N)
Chen-Kung_Univ(120.21E,23.00N)
Taipei_CWB(121.50E,25.03N)
Aerosol Optical Depth
Day of Month (03/2005)

Figure 3.7. AOD values from AERONET (black asterisks), MODIS (red diamonds), and WRF-Chem simulation (blue lines) are compared at the location of 10 AERONET sites.

Table 3.2. Statistics of aerosol optical depth from AERONET and WRF-Chem

Station	AERONET		Model		Bias	Corr
	mean	std	mean	std		
Gosan_SNU	0.26	0.18	0.53	0.13	0.27	0.52
Shirahama	0.39	0.21	0.39	0.13	0.007	0.54
Anmyon	0.37	0.13	0.35	0.14	-0.02	0.60
Gwangju_K-JIST	0.47	0.32	0.45	0.18	-0.02	0.38
Beijing	0.52	0.49	0.36	0.19	-0.14	0.72
Xianghe	0.60	0.35	0.35	0.16	-0.25	0.72
NCU_Taiwan	0.62	0.37	0.43	0.11	-0.19	0.37
Osaka	0.65	0.15	0.47	0.06	-0.18	0.25
Chen-Kung_Univ	0.63	0.36	0.45	0.14	-0.18	0.57
Taipei_CWB	0.64	0.29	0.45	0.13	-0.19	0.38

3.2.2 Aerosol direct effect

As shown in section 3.2.1, WRF-Chem reproduces the observed meteorological fields with high temporal correlations ($R > 0.7$) and low biases. The concentrations of trace gases are moderately well simulated ($0.4 < R < 0.7$) with NO and NO_y overestimated and SO_2 and CO underestimated. Temporal fluctuations in AOD are also well ($R > 0.7$) simulated although some peaks are underestimated at highly polluted locations and on highly polluted days. With the reasonable capability in simulating the interaction between meteorology, chemistry and aerosol, we investigate the ADE by comparing the differences between sensitivity runs Base and Base_No_ADE.

The feedbacks of aerosols on surface shortwave radiation are examined in Figure 3.8, which compares model output with measurements from the World Radiation Data Center (WRDC) at six Chinese stations. The upper three stations in Figure 3.8 (Beijing, Shengyang and Harbin) are from northern China, and the lower three stations (Kunming, Guangzhou and Shanghai) are from southern China (Figure 2.4, black stations). The Base case captures the trend and magnitude of the surface radiation moderately well, with temporal correlations between 0.4 and 0.7, and an average bias of 61.5 W/m^2 (Table 3.3). Biases are largest at all stations for the Base_No_ADE case that does not include ADE. The average aerosol direct forcing on surface radiation for these six stations is -21.2 W/m^2, and is -27 W/m^2 for Beijing station, which is close to the value obtained at Xianghe [*Xia et al., 2007a*] by subtracting the calculated radiative flux assuming aerosol-free conditions from the observed surface radiation. Figure 8 also shows temporal variations of daily AOD at each station. Negative correlation coefficients between AOD and surface SW

radiation ranging from -0.50 to -0.82 are found, suggesting the important impact of the ADE on surface SW radiation.

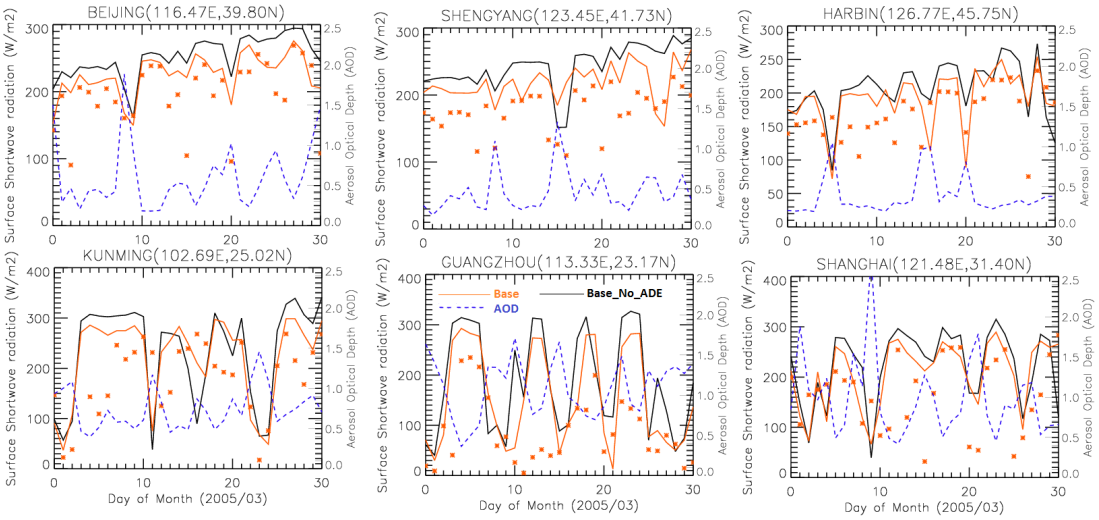

Figure 3.8. Daily surface shortwave radiation from World Radiation Data Center (red asterisks) and two WRF-Chem simulations (red: Base; black: Base_No_ADE) for March, 2005. The blue dashed line is the simulated daily average AOD from Base run at each station.

Table 3.3. Statistics of the comparison of surface shortwave radiation between WRF-Chem and WRDC data

	Base			Base_No_ADE		
	Correlation (R)	Bias (W/m^2)	RMSE	Correlation (R)	Bias (W/m^2)	RMSE
Beijing	0.69	82.6	44.6	0.63	109.7	66.7
Shengyang	0.50	45.2	52.3	0.78	69.3	70.4
Harbin	0.45	52.3	46.8	0.48	66.7	54.3

Kunming	0.44	73.8	103.2	0.35	87.9	123.2
Guangzhou	0.60	105.4	103.1	0.50	168.8	134.4
Shanghai	0.51	9.6	79.6	0.35	24.1	99.2

Figure 3.9a shows mean model surface shortwave radiation from the Base case for March 2005. The spatial pattern shows a gradual decrease of surface SW radiation from south to north primarily due to the change in sun angle with latitude. A maximum is also seen over the elevated Tibetan plateau with relatively low values over the Sichuan Basin and southern China. Aerosols lead to the domain-wide decrease of surface SW radiation over land due to the ADE with an average of -20 W/m^2 (Figure 3.9b). The reduction is higher than the domain average over the four regions of interest (Table 3.4): western China (-30.8 W/m^2), eastern China (-27.1 W/m^2), Sichuan Basin (-25.8 W/m^2), and southern China (-22.8 W/m^2), as $PM_{2.5}$ concentrations are high with respect to the domain average in these regions (Figure 3.10a). The percentage changes of the surface SW radiation due to the ADE in these four regions range from -11.7% to -14.3%, comparable with the 15% decrease shown in *Wang et al*. [2015].

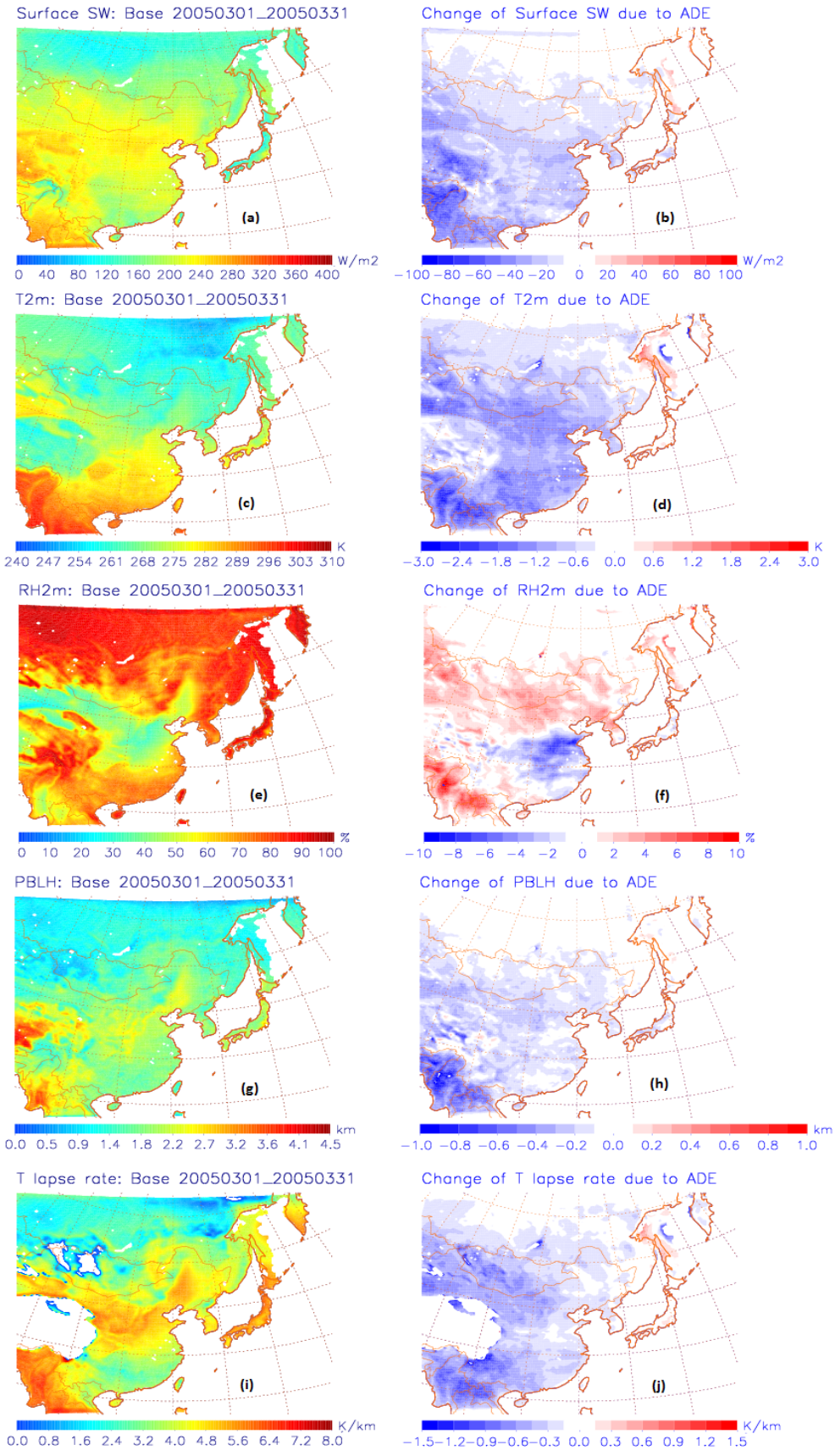
Surface SW: Base 20050301_20050331
(a)
W/m2
0 40 80 120 160 200 240 280 320 360 400
Change of Surface SW due to ADE
(b)
W/m2
−100 −80 −60 −40 −20 0 20 40 60 80 100
T2m: Base 20050301_20050331
(c)
K
240 247 254 261 268 275 282 289 296 303 310
Change of T2m due to ADE
(d)
K
−3.0 −2.4 −1.8 −1.2 −0.6 0.0 0.6 1.2 1.8 2.4 3.0
RH2m: Base 20050301_20050331
(e)
%
0 10 20 30 40 50 60 70 80 90 100
Change of RH2m due to ADE
(f)
%
−10 −8 −6 −4 −2 0 2 4 6 8 10
PBLH: Base 20050301_20050331
(g)
km
0.0 0.5 0.9 1.4 1.8 2.2 2.7 3.2 3.6 4.1 4.5
Change of PBLH due to ADE
(h)
km
−1.0 −0.8 −0.6 −0.4 −0.2 0.0 0.2 0.4 0.6 0.8 1.0
T lapse rate: Base 20050301_20050331
(i)
K/km
0.0 0.8 1.6 2.4 3.2 4.0 4.8 5.6 6.4 7.2 8.0
Change of T lapse rate due to ADE
(j)
K/km
−1.5 −1.2 −0.9 −0.6 −0.3 0.0 0.3 0.6 0.9 1.2 1.5

Figure 3.9. March, 2005 monthly mean of hourly: surface shortwave radiation (a), temperature at 2m (c), relative humidity at 2m (e), PBLH (g) and temperature lapse rate between 700 hPa and surface (i) simulated by WRF-Chem Base case; monthly mean of changes of surface shortwave radiation (b), temperature at 2m (d), relative humidity at 2m (f), PBLH (h) and temperature lapse rate between 700 hPa and surface (j) due to the ADE.

Table 3.4. Percentage changes of meteorological variables due to ADE in different regions

(Change=Base−Base_No_ADE)

Eastern China	**SWDOWN (W/m^2)**	**T_{2m} (K)**	**RH_{2m} (%)**	**PBLH (m)**	**T lapse rate (K/km)***
Mean (Base)	219.7	276.6	44.9	1262.2	4.87
Mean (Base_No_ADE)	246.9	277.7	48.2	1337.4	5.09
Change	-27.2	-1.1	-3.3	-75.2	-0.22
Southern China	**SWDOWN (W/m^2)**	**T_{2m} (K)**	**RH_{2m} (%)**	**PBLH (m)**	**T lapse rate (K/km)***
Mean (Base)	193.6	282.6	66.4	1206.6	3.56
Mean (Base_No_ADE)	216.4	283.7	68.1	1301.0	3.86
Change	-22.8	-1.1	-1.7	-94.4	-0.30
Western China	**SWDOWN (W/m^2)**	**T_{2m} (K)**	**RH_{2m} (%)**	**PBLH (m)**	**T lapse rate (K/km)***
Mean (Base)	221.5	275.3	40.4	994.4	4.47
Mean (Base_No_ADE)	252.4	276.5	38.6	1132.8	5.10

Change	-30.9	-1.2	1.8	-138.4	-0.63
Sichuan Basin	**SWDOWN (W/m^2)**	**T_{2m} (K)**	**RH_{2m} (%)**	**PBLH (m)**	**T lapse rate (K/km) ***
Mean (Base)	194.6	281.6	58.2	1155.4	4.11
Mean (Base_No_ADE)	220.4	282.8	58.7	1266.7	4.61
Change	-27.8	-1.2	-0.5	-111.3	-0.50

* The calculation of temperature lapse rate has excluded the locations with surface pressure lower than 700hPa.

The hourly surface SW radiation shows a good agreement between the observation at Xianghe and the WRF-Chem (Base) simulation (Figure 3.11, top) on two cloud-free days (March 12 and March 13, 2005). The mean bias is 8 W/m^2 for these two days, and the highest bias occurs at noon and is 43 W/m^2 (5% higher than the observation). The high bias in the model simulated surface radiation during these two clear-sky days comes from the underestimated AOD by WRF-Chem. The ADE on the surface SW radiation (Figure 3.11, bottom) at Xianghe is up to -40 W/m^2 with a diurnal mean of -15.6 W/m^2 for these two days.

Surface temperatures are generally reduced by the ADE (Figure 3.9d), with an average reduction of about 0.73˚C over land. The largest impacts on surface temperature in China are shown in the Sichuan Basin, cooling this region by ~ 1.4 ˚C. Changes of relative humidity (RH) differ between the four regions, with decreases in eastern China (3.3%), southern China (1.7%) and the Sichuan Basin (0.5%), and an increase in western China (1.8%).

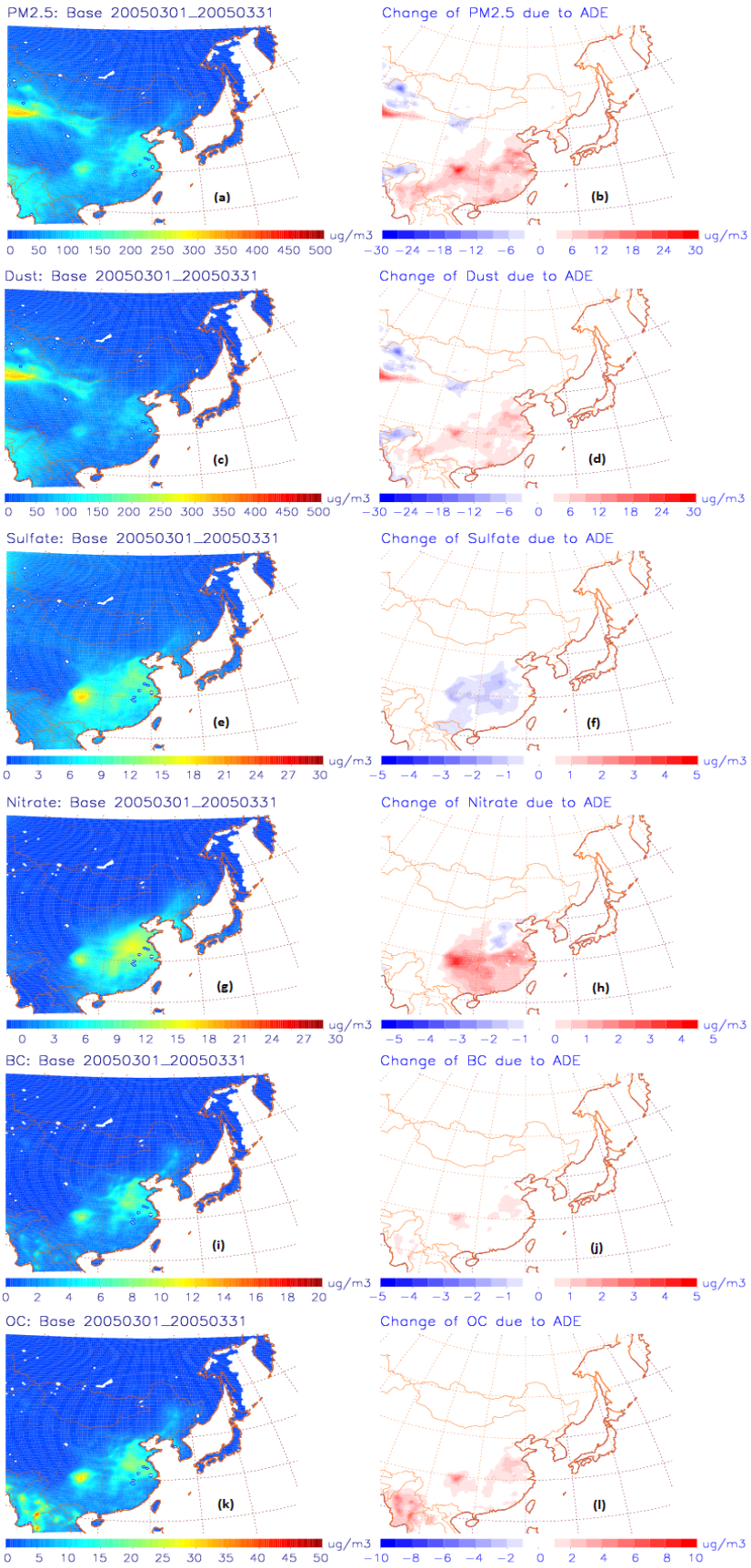
PM2.5: Base 20050301_20050331
Change of PM2.5 due to ADE
(a)
(b)
ug/m3
0 50 100 150 200 250 300 350 400 450 500
−30 −24 −18 −12 −6 0 6 12 18 24 30
Dust: Base 20050301_20050331
Change of Dust due to ADE
(c)
(d)
ug/m3
0 50 100 150 200 250 300 350 400 450 500
−30 −24 −18 −12 −6 0 6 12 18 24 30
Sulfate: Base 20050301_20050331
Change of Sulfate due to ADE
(e)
(f)
ug/m3
0 3 6 9 12 15 18 21 24 27 30
−5 −4 −3 −2 −1 0 1 2 3 4 5
Nitrate: Base 20050301_20050331
Change of Nitrate due to ADE
(g)
(h)
ug/m3
0 3 6 9 12 15 18 21 24 27 30
−5 −4 −3 −2 −1 0 1 2 3 4 5
BC: Base 20050301_20050331
Change of BC due to ADE
(i)
(j)
ug/m3
0 2 4 6 8 10 12 14 16 18 20
−5 −4 −3 −2 −1 0 1 2 3 4 5
OC: Base 20050301_20050331
Change of OC due to ADE
(k)
(l)
ug/m3
0 5 10 15 20 25 30 35 40 45 50
−10 −8 −6 −4 −2 0 2 4 6 8 10

Figure 3.10. March, 2005 monthly mean surface concentration of: PM2.5 (a), dust (c), sulfate (e), nitrate (g), Black Carbon (BC) (i), Organic Carbon (OC) (k) simulated by WRF-Chem Base case; monthly mean surface concentration changes of PM2.5 (b), dust (d), sulfate (f), nitrate (h), Black Carbon (BC) (j), Organic Carbon (OC) (l) due to the ADE.

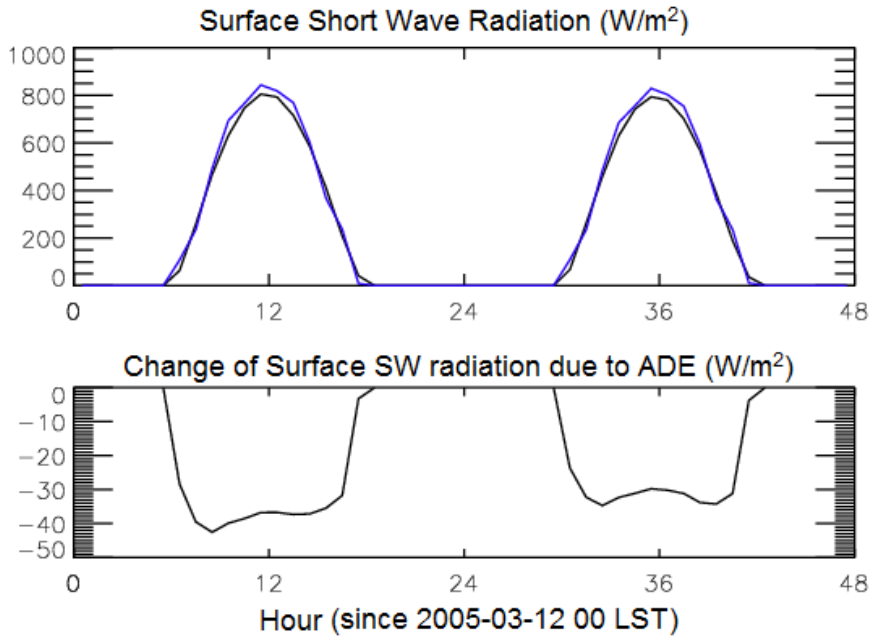

Figure 3.11. Top panel: observed surface shortwave radiation at Xianghe Observatory (black) and WRF-Chem Base (blue) between 2005-03-12 00:00 and 2005-03-13 23:00 Local Standard Time (LST); Bottom panel: Change of surface shortwave radiation due to the ADE between 2005-03-12 00:00 and 2005-03-13 23:00 LST.

The impacts of the ADE on surface concentrations of $PM_{2.5}$ and its components are shown in Figure 3.10. Monthly mean surface $PM_{2.5}$ is high over eastern China (116 $\mu g/m^3$), southern China (76 $\mu g/m^3$), Sichuan Basin (116 $\mu g/m^3$), and western China

(155 μg/m^3) (see Figure 2.4 for latitude/longitude boundaries of each region). Dust is the dominant component in all regions, while sulfate is most important in the Sichuan Basin, and nitrate, BC and OC all have high values over the Sichuan Basin and eastern China. $PM_{2.5}$ in east China is composed of dust (61.6%), sulfate (7.1%), nitrate (9.4%), BC (4.8%) and OC (11.4%). In southern China, dust is 58.1%, sulfate is 10%, OC is 9.8%, nitrate is 10.8%, and BC is 3.3% of the total $PM_{2.5}$. Composition of $PM_{2.5}$ in western China is mainly dust aerosols (97.4%). In the Sichuan Basin, $PM_{2.5}$ components include 58.7% dust, 10.6% sulfate, 7.7% nitrate, 3.8% BC and 12.8% OC.

The ADE has a different impact on $PM_{2.5}$ components in different regions. The ADE increases the total $PM_{2.5}$ concentration in all four regions (4.4% in eastern China, 10% in southern China, 2.3% in western China, and 9.6% in the Sichuan Basin) and all the primary aerosols (dust, BC and OC) (Table 3.5). The percentage increases in $PM_{2.5}$ found here are less than the 14% found by *Wang et al*. [2015], which is to be expected as they show an average over a hazy period in July while we show monthly averages from March. The enhancement of primary aerosols can be attributed to a thinner mean planetary boundary layer height (PBLH) and a more stabilized atmosphere. The PBLH is mainly driven by the strength of the thermal and mechanistic turbulence. Cooler surface temperatures cause weaker thermal turbulence; therefore the PBLH gets thinner (Figure 3.9h), with the regional average decrease ranging from 75 meters to 138 meters (Table 3.4), therefore concentrating pollutants. The ADE also tends to stabilize the atmosphere. We use the temperature lapse rate between the surface and 700 hPa (Figure 3.9i) as a proxy for atmospheric

stability as applied in *Storer et al* [2014]. The temperature lapse rate reduces domain wide (Table 3.4), which means the temperature difference between the surface and 700 hPa is smaller, and air parcels have less tendency to move upward, therefore constraining the vertical mixing of aerosols. Increased atmospheric stability due to aerosol effects was also shown by *Park et al.,* [2001].

Table 3.5. Percentage changes of $PM_{2.5}$ due to ADE in different regions

(Change= Base−Base_No_ADE)

Eastern China	**$PM_{2.5}$**	**Dust**	**Sulfate**	**Nitrate ($\mu g/m^3$)**	**BC**	**OC**	**Ammonia**
Mean (Base)	116.1	71.5	8.3	10.9	5.2	13.2	6.3
Mean (Base_No_ADE)	111.2	67.3	8.9	11.0	4.8	12.2	6.5
Change	4.9 (4.4%)	4.2 (6.2%)	-0.6 (-6.7%)	-0.1 (-0.9%)	0.4 (8.3%)	1.0 (8.2%)	-0.2 (-3.1%)

Southern China	**$PM_{2.5}$**	**Dust**	**Sulfate**	**Nitrate ($\mu g/m^3$)**	**BC**	**OC**	**Ammonia**
Mean (Base)	75.7	44.0	7.6	8.2	2.5	7.4	5.0
Mean (Base_No_ADE)	68.9	39.9	8.0	6.6	2.2	6.5	4.7
Change	6.8 (10%)	4.1 (10.3%)	-0.4 (-5%)	1.6 (24.3%)	0.3 (13.6%)	0.9 (13.8%)	0.3 (6.4%)

Western China	**$PM_{2.5}$**	**Dust**	**Sulfate**	**Nitrate ($\mu g/m^3$)**	**BC**	**OC**	**Ammonia**
Mean (Base)	155.2	151.2	2.2	0.23	0.19	0.55	0.80
Mean (Base_No_ADE)	151.6	147.8	2.2	0.25	0.18	0.52	0.78
Change	3.6	3.4	0	0.06	0.01	0.03	0.02

	(2.3%)	(2.3%)	0	(31.6%)	(5.6%)	(5.8%)	(2.6%)

Sichuan Basin	**$PM_{2.5}$**	**Dust**	**Sulfate**	**Nitrate ($\mu g/m^3$)**	**BC**	**OC**	**Ammonia**
Mean (Base)	115.9	68.0	12.3	8.9	4.4	14.8	7.2
Mean (Base_No_ADE)	105.7	62.1	13.3	6.4	3.9	12.9	6.7
Change	10.2 (9.6%)	5.9 (9.5%)	-1.0 (-7.5%)	2.5 (39%)	0.5 (12.8%)	1.9 (14.7%)	0.5 (7.5%)

The emissions of BC and OC are held constant, however the dust emission will change due to ADE-related changes in soil moisture and wind speed. Figure 3.12 shows the distribution of dust emissions and the change due to the ADE. The dust emissions in our work are calculated by the GOCART dust scheme, using erosion and porosity data from WRF geographical input files, dust sizes, dust densities, and dust effective radius from look-up tables included in WRF-Chem, and prognostic variables from the model simulation (soil moisture and wind speed at 10 meters). The maximum reduction of dust emission due to the ADE is about 8.6 kg/s per gridbox, which is about 16% of the total emission at that location (Figure 3.12b). Both changes of soil moisture (up to 8.6% more moist) and wind speed (up to 10% weaker wind) due to ADE contribute to the reduction of dust emission (Figure 3.12c, 3.12d), with the change of wind speed having dominant impact. However, the reduction of the dust emission does not lead to a decrease in dust aerosol concentration in most parts of western China, which implies that the change of meteorological conditions (PBLH and temperature lapse rate) are the driving factors for the change of dust aerosol due to the ADE.

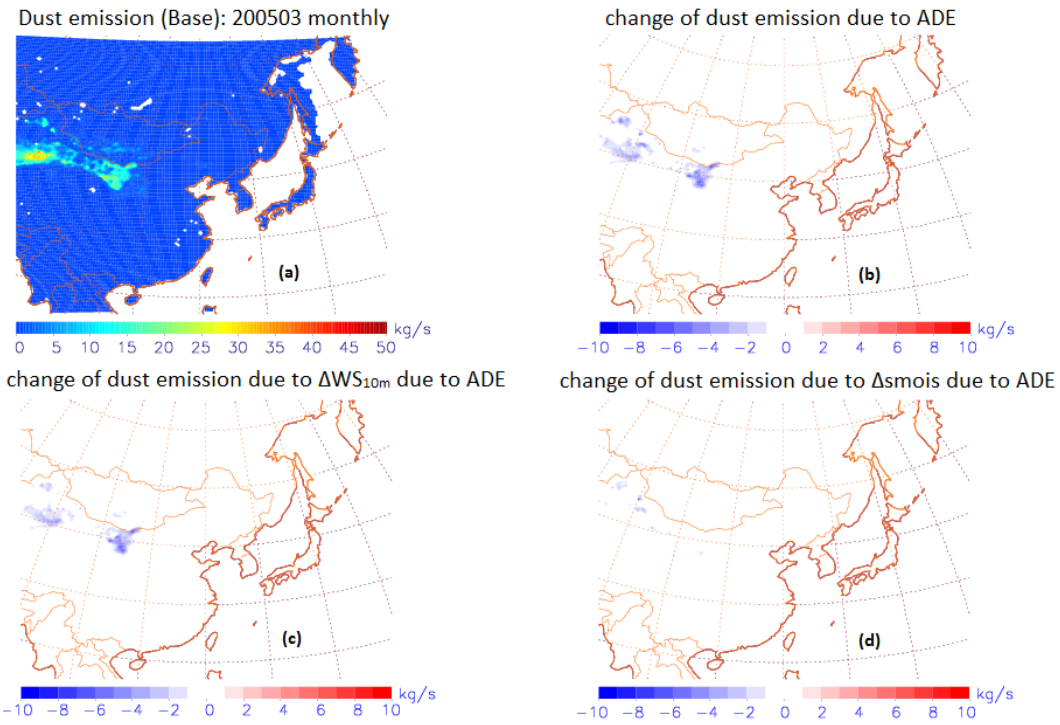

Figure 3.12. March, 2005 monthly mean of dust emission: (a) surface distribution simulated by WRF-Chem Base case based on GOCART dust scheme; (b) change due to ADE; (c) change due to Δsoil moisture caused by ADE; (d) change due to Δwind speed at 10-meter altitude caused by ADE.

The effect of the ADE on secondary aerosols, i.e., sulfate and nitrate, is different from that on primary aerosols, since the driving factors for these species differ. Under the same meteorological conditions, sulfate decreases in all four regions due to the ADE, mainly caused by the inhibited aqueous phase and gas phase reactions of SO_2 to form sulfate. Aqueous phase reactions between SO_2 and H_2O_2 or SO_2 and O_3 are the major pathways for sulfate formation although gas phase reaction of SO_2 with OH is also important [*Eriksen*, 1972; *Tanaka et al.*, 1994; *Harris et al.*, 2012]. Analyses based on the difference between the Base run and the Base_No_ADE run show domain-

wide decreases of H_2O_2 with a maximum reduction over the Sichuan Basin (6.9%) and domain-wide decreases of ozone with a maximum reduction over Eastern China (12%) due to the ADE. The cloud water amount also decreases, but only by a small amount due to the ADE. The reductions in H_2O_2, O_3, and cloud water slow down the sulfate formation from aqueous phase reactions, thus also leading to decreased sulfate aerosols due to the ADE. The domain-wide average surface OH concentration is 0.02 pptv, and it is reduced by 20% because the ADE decreases the incoming solar radiation, thus slowing the photolysis of H_2O_2, HONO, and O_3 to form OH. The Sichuan Basin has the highest OH concentration of the four regions, approximately 0.4 pptv in the Base_No_ADE run, and the percentage change of OH in Sichuan Basin is also highest (-40%). Therefore the relatively large decrease of sulfate aerosol in Sichuan Basin is likely due to the high percentage changes in H_2O_2 and OH there. The change of nitrate due to the ADE shows regional differences. *G. Wang et al*.,[2016] proposed a new sulfate formation mechanism that includes efficient oxidation of, SO_2 by NO_2 to form sulfate under severe haze condition. If this mechanism were used in this simulation, it is possible that,the increase in NO_2 due to less photolysis and favorable meteorological conditions (i.e., thinner PBL and more stabilized lower troposphere) would lead to an increase in sulfate that would counter the change discussed above. Nitrate is enhanced in southern China, Sichuan Basin and western China, but decreased in eastern China. The composition of nitrate is mostly NH_4NO_3, and the formation of NH_4NO_3 largely depends on the availability of ammonia. The surface concentration of ammonia also shows a decrease in eastern China and an increase in the other three regions (Table 3.5).

Ground-level ozone decreases due to the ADE. Domain-wide decreases of surface 1-hour maximum ozone are shown in Figure 3.13, with a domain average reduction of 1.0 ppbv and a maximum decrease of 12.0 ppbv located in the Sichuan Basin. Ozone is reduced because the ADE is dominated by the dust that absorbs UV radiation and leads to less solar radiation reaching the boundary layer (Figure 3.9b). Therefore the photolysis process for NO_2 is slowed down, which leads to less tropospheric ozone formation. Meanwhile, the ADE leads to the decrease of biogenic VOC emissions, most significantly in southern China. For example, the biogenic isoprene emissions are reduced by 51% in southern China due to the ADE. The reduction in VOC emissions is partly responsible for the decrease of the surface ozone; however, it is unlikely to be the dominant factor in this season in most parts of China. The ozone dry deposition velocity also decreases due to the ADE. The dry deposition velocity is calculated based on aerodynamic resistance, quasi-laminar resistance, and surface resistance, among which the surface resistance is dominant. The surface resistance in WRF-Chem v3.3 is parameterized as a function of solar radiation, surface air temperature, surface type, and vegetation type with the Wesely scheme [*Wesely*, 1989]. In general, the ozone deposition velocity decreases with less surface solar radiation and cooler surface temperatures due to the ADE, with a domain-average decrease of 8%. The slower photochemistry and less VOC emissions due to the ADE contribute to the decrease of surface ozone while the smaller dry deposition velocity leads to the accumulation of ozone in lower troposphere, leading to a negative feedbacks between the ADE and surface ozone concentrations.

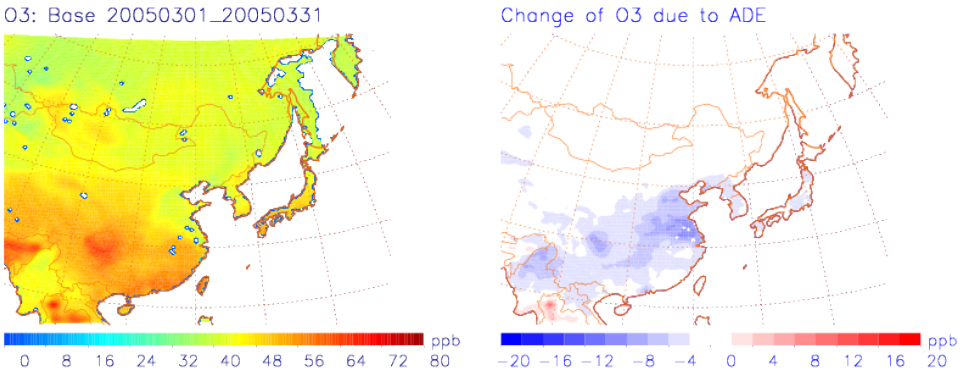

Figure 3.13. March, 2005 monthly mean of surface 1-hour maximum ozone: (left column) surface distribution simulated by WRF-Chem Base case; (right column) change due to ADE.

Forkel et al. [2012] found increases in monthly average surface ozone in July over Germany, Eastern Europe, and southwestern France, associated with increases in surface SW radiation. They attributed most of the changes to the aerosol semi-direct effect. They found that the changes in surface radiation were not correlated with aerosol amounts and inferred that they were mostly due to the cloud cover change from the semi-direct effect. *Makar et al*. [2014] also studied the relative importance of aerosol direct and indirect effects on meteorology. Focusing on Europe and North America they found that the indirect effect on meteorological fields is usually larger than the direct effect and sometimes opposes the direct effect.

We find a negative temporal correlation between aerosol loading (represented by AOD) and surface SW radiation with correlation coefficients at six WRDC stations ranging from -0.50 to -0.82 (Figure 3.8), suggesting the aerosol loading is an important factor determining the temporal variation of the surface SW radiation.

However, the semi-direct effect also plays a role as the cloud optical depth (CODs) decreases over much of the domain. This decrease in COD increases surface SW radiation and ambient ozone and partially counters the increase in SW radiation and ozone due to the ADE. The large aerosol loading and relatively low water vapor concentrations in our domain during this season may cause the stronger ADE and weaker semi-direct effect in our case compared to *Forkel et al*. [2012].

3.2.3 Impact of future emission reductions

SO_2 emissions declined 15% between 2005 and 2010 due to large-scale deployment of flue gas desulfurization (FGD) at China's power plants [*Li et al.,* 2010, *Wang et al.,* 2014]. Assuming best available technologies are fully implemented, SO_2 emissions in 2030 should be reduced to 27% of the 2010 level [*Wang et al.,* 2014]. The RCP4.5 emission scenario estimates 2050 SO_2 emission to be 20% of that in 2005. Therefore, we assume that the SO_2 emissions will decrease by 80% in 2050 compared to the 2005 level, and apply this reduction in our sensitivity run (SO_2×0.2_ADE). With less SO_2 emission, surface shortwave radiation increases, especially south of 30˚N. Surface temperatures are higher with emission reductions with the maximum increase about 0.15K in China. By emitting less SO_2, the air quality is mostly improved (Figure 3.14). SO_2 is the precursor of sulfate aerosol, a scattering aerosol. Regulating SO_2 leads to changes of the scattering aerosols. The impact on $PM_{2.5}$ concentration is most significant over the Sichuan basin and southern China, with reductions of up to 17.5 $\mu g/m^3$ in Sichuan Basin and southern China and a regional average decrease of 5.4%. However, in this simulation reducing SO_2 emissions leads to an increase of $PM_{2.5}$ over dusty areas in western China as dust

emissions increase due to ADE-induced changes that are shown in Figure 3.12. The surface 1-hour maximum ozone concentration goes down by up to 6 ppbv in Sichuan Basin, and up to 4 ppbv in eastern China. This result is consistent with the study by *Dickerson et al*. [1997] indicating that scattering aerosols accelerate boundary layer ozone production since scattering of UV radiation enhances the actinic flux and simultaneously the photolysis rate in the boundary layer. Therefore, in our sensitivity run, reducing SO_2 emissions is also beneficial for reducing ozone pollution.

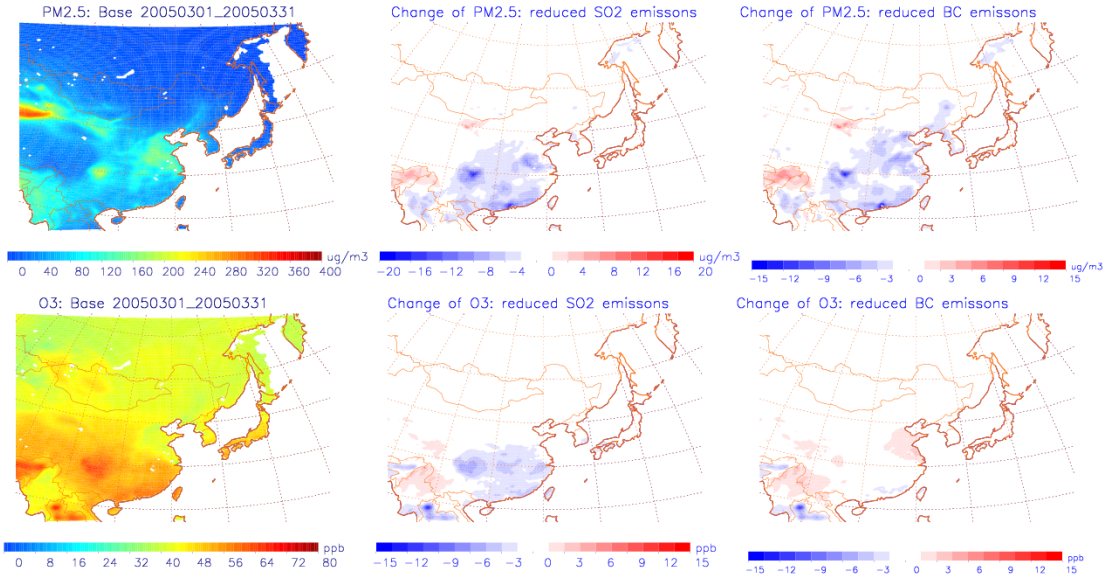

Figure 3.14. Change of surface $PM_{2.5}$ concentration and surface ozone concentration due to SO_2 and BC emission reductions

In 2005, the total BC emission in China according to the INTEX-B emission inventory was 1811 Gg/year, while the total black carbon emission from the US was 580 Gg(Report to Congress on Black Carbon, *EPA*, 2010). Assuming the best control technologies are available and that rigorous regulations are fully implemented, the BC

emission in China is expected to decrease to the current US level by 2050, approximately 20% of the INTEX-B level. The sensitivity simulation (BC×0.2) tested the impact of reducing BC emissions to 20% of INTEX-B levels. BC is mainly a primary aerosol, i.e., it is emitted directly. The surface radiation and surface temperature are both enhanced due to BC emission reductions, similar to the case with less SO_2 emission. The $PM_{2.5}$ level declines, especially in the Sichuan Basin (by up to 13 $\mu g/m^3$) and eastern China (up to 6.8 $\mu g/m^3$). However, the ozone pollution worsens in the Sichuan Basin (with increases of up to 3.2 ppbv) and parts of eastern China (increases of up to 3.6 ppbv) (Figure 3.14). Reducing absorbing aerosols allows more shortwave radiation to reach the surface, therefore increases photolysis rates, and accelerates the photochemistry of ozone production.

3.3 Summary

WRF-Chem sensitivity simulations were conducted in East Asia for the EAST-AIRE IOC period (March, 2005) to investigate the ADE on surface radiation and air quality. Comparison between model and *in-situ* and satellite observations demonstrated that WRF-Chem when run with the configuration shown in Table 2.1 captured the temporal and spatial variations of meteorological fields, trace gases, and aerosol loadings reasonably well. However, WRF-Chem underestimated some peak values of trace gases (CO, SO_2) and AOD, partly due to the biases in simulated wind fields and the coarse resolution of emission inventories. Scattering by aerosols was underestimated in the model partially due to low biases in OC emissions and the lack of aging processes for absorbing aerosols (BC), leading to the AOD underestimation.

We found that the effect of ADE on surface SW radiation is -20 W/m^2 domain-wide, with a value of -25 W/m^2 at Xianghe Observatory, consistent with observations. The ADE caused diverse changes in $PM_{2.5}$ and its components in four regions of China with high $PM_{2.5}$ loading. The surface $PM_{2.5}$ level was enhanced domain wide due to ADE, with increase of 4.4 % in eastern China, 10% in southern China, 2.3% in western China, and 9.6% in the Sichuan Basin, as a result of reduced vertical mixing. The concentrations of primary aerosols (dust, BC and OC) increase in the four regions mainly driven by the thinner PBL and higher atmospheric stability caused by the ADE. The changes of secondary aerosols (sulfate and nitrate) due to the ADE show different signals compared to primary aerosols, largely driven by the change of the chemistry such as the oxidation capacity of the atmosphere. The oxidation capacity decreases because the decrease in photolysis due to the ADE leads to smaller OH concentrations in the atmosphere. The ADE leads to a domain-wide decrease in sulfate, with the maximum in Sichuan Basin (-7.5%). Nitrate increases in southern China, western China and the Sichuan Basin, but decreases in eastern China, consistent with the change of ammonia aerosol.

Two sensitivity simulations were carried out to test the potential impact of emission reductions on East Asian air quality. Our study with reduced BC and SO_2 emissions indicates that reducing absorbing aerosols could lead to an increase in certain gas pollutants (i.e., ozone) if emissions of NO_x and VOC are unchanged, while reducing scattering aerosols would have co-benefits in ozone pollution. Thus policy makers need to take the aerosol types and the interaction between aerosols and other air pollutants into account when implementing PM regulations.

Chapter 4: Relative importance of the impact of aerosol direct and indirect effects on meteorology and air quality

4.1 Introduction

Previous studies using coupled regional models have shown that the ADE leads to lower surface shortwave radiation amounts, cooler surface temperatures, thinner planetary boundary layer heights, and more stabilized boundary layers [*Forkel et al*., 2012; *Zhang et al*., 2015; *J. Wang et al.*, 2016], which results in enhanced air pollutant (CO, SO_2, PM2.5) levels [*Zhang et al*., 2015; *Wang et al*., 2016]. Feedbacks induced by the AIE are more complicated and uncertain than feedbacks induced by the ADE based on many previous studies by regional models ([*Forkel et al*., [2012]; *Makar et al*., [2015a]; *Makar et al*., [2015b]; *Zhang et al*., [2015]). For example, *Makar et al*. [2014] investigated aerosol effects on meteorology over North America and Europe using multiple regional models and found that at most locations the AIE increased the magnitude of changes due to the ADE. Specifically, AIE intensified changes in surface shortwave radiation, 2-meter surface air temperature, and Planetary Boundary Layer (PBL) height due to the ADE over North America, but ameliorated changes in the same quantities over regions of Europe that were not impacted by Russian fires. *Forkel et al.* [2012] found that the AIE had a stronger

impact on surface shortwave radiation, surface temperature and PBL height relative to the ADE in July over Europe. *Zhang et al.* [2015] simulated a hazy winter period in January 2013 over Eastern China and discovered that for this period when aerosol loading was extremely high, the ADE had a larger impact on meteorology (i.e., solar radiation, temperature, wind speed and PBL height) than the AIE. This result differs from that found by *Forkel et al*. and *Makar et al*. over regions with low aerosol loading.

This chapter explores the relative importance of the ADE and AIE on meteorology and atmospheric chemistry, and the subsequent impact on air quality over East Asia during the EAST-AIRE campaign [*Li et al.,* 2007] period of March 2005 using the fully coupled online regional model, WRF-Chem, following up on our previous study [*J. Wang et al*., 2016] of the same time period that investigated the feedbacks of the ADE on radiation, meteorological variables, and air quality.

4.2 Experiment setup

In this experiment, the WRF-Chem simulated domain covers most of China and Korea with a horizontal resolution of 12 km and 32 vertical layers from the surface to 100 hPa (Figure 2.5). The input datasets, emission inventories, and physics and chemistry options used in the model, listed in Table 2.1, were same as in Chapter 3. Secondary Organic Aerosols (SOA) formation is not included as comprehensive SOA schemes were not available in the version of WRF-Chem used in this study. The impact of neglecting SOA formation in this region during this time period is discussed in Chapter 3, section 3.2.1.

Three WRF-Chem experiments were conducted to investigate the aerosol direct and

indirect effects (Table 4.1): 1) AER-all: both aerosol direct and indirect effects included; 2) No_ADE: aerosol direct effect not included; 3) No_AIE: aerosol indirect effect not included. The AER-all simulation includes aerosol formation from precursors, aerosol interaction with radiation and formation of cloud droplets from prognostic aerosols. WRF-Chem has a cloud droplet activation module that connects the simulated aerosol information with the microphysics scheme. The activation module generates cloud droplets based on the maximum supersaturation, which is calculated using a combination of the simulated vertical velocity and turbulent motions, and properties (i.e., hygroscopicity, size distribution) of the internally mixed prognostic aerosol within each size bin [*Chapman et al.,* 2009]. The calculated cloud droplets are then passed to the double-moment Morrison microphysics scheme that calculates number concentration and mass mixing ratios of cloud water, cloud ice, snow, rain, and graupel/hail from four microphysical processes: autoconversion, collection between hydrometeor species, melting/freezing, and ice multiplication [*Morrison et al*., 2005]. In the No_ADE simulation, aerosol information is not passed to the radiative transfer scheme, effectively removing the direct effect, however, prognostic aerosols are passed into the activation module of the microphysics scheme thus retaining the AIE. In the No_AIE case, prognostic aerosol information is passed to the radiative transfer scheme, keeping the ADE; however, instead of using prognostic aerosol concentrations, we modified the activation module to use a constant low "pre-industrial" aerosol concentration ($1x10^8$ particles per kilogram air) combined with prognostic meteorological conditions to generate spatially and temporally varying “pre-industrial” cloud droplets. Activation based on constant

background aerosols concentrations and prognostic meteorological conditions leads to spatial variations in cloud droplet numbers that are consistent with the spatial distribution of aerosols. This concentration is a factor of 100 less than is typical in this region during this season. This low aerosol concentration is then passed into the cloud droplet activation module. This approach of minimizing the AIE is different than many previous studies [*Forkel et al*., 2012; *Makar et al*., 2014; *Zhang et al*., 2015] that use a constant cloud droplet number concentration (250 cm^{-3} used in *Forkel et al*. [2012] and *Makar et al*. [2014] and 1×10^{8} kg^{-1} used in *Zhang et al.* [2015], respectively) throughout the simulation domain in the microphysics scheme in their "no-AIE" simulations. In this version of WRF-Chem, only the warm rain process is connected with the prognostic aerosols through the activation of CCN from simulated aerosols [*Yang et al.*, 2011] while the activation of IN is parameterized. Loss of prognostic airborne aerosols serving as ice nuclei (IN) is not treated in version 3.3 (as discussed in *Zhang et al*. [2015]) or in version V3.6.1 (*Gao et al*., 2016], and therefore we focus on the impact of aerosols on liquid clouds in this study. Besides the impact of aerosols on cloud droplet activation, another part of aerosol-cloud interactions in warm clouds is the impact of cloud on aerosols (wet removal is the main sink of airborne aerosols). Wet scavenging processes [*Easter et al*., 2004] are included in all three sensitivity runs.

Based on these three simulations, we estimate the impact of the direct effect using the difference between AER-all and No_ADE simulations, and the impact of the indirect effect using the difference between AER-all and No_AIE simulations. The semi-direct effect can not be separated based on this setup, thus the “direct effect”

discussed in following sections includes both direct and semi-direct effects, unless otherwise specified. The approach used in estimating the ADE is the same as in *Wang et al.* [2016], and differs from several previous studies [*Forkel et al*., 2012; *Makar et al*., 2014; *Zhang et al*., 2015] that estimate the direct effect using the difference between simulations that do not include the indirect effect. We choose to use this approach to minimize biases in aerosol amounts resulting from biases in precipitation due to neglecting the AIE. This approach may also result in a better estimation of radiative warming as it includes the effect of absorbing aerosols above cloud layers [*Ghan et al.*, 2013].

Table 4.1. Summary of three sensitivity simulations in the experiment setup

AER-All	Include all the aerosol feedbacks
No_ADE	Aerosol direct effect is removed
No_AIE	Aerosol indirect effect is removed

4.3 Results and discussions

The WRF-Chem simulations were conducted for February 22 to March 15, 2005 with the first week (February 22 to February 28) being discarded as spin-up. In *Wang et al.* [2016] the model was shown to capture temporal and spatial variations of meteorological fields, surface radiation, trace gases, and aerosol loading reasonably well. In this work, we increase the horizontal resolution of the simulations from 36 km to 12 km making it necessary to interpolate the input data sets and emission inventories used in *Wang et al*. [2016] to the new domain. Correlations and biases

between modeled (AER-All 12km and AER-All 36-km simulations) and observed meteorological fields and trace gases at Xianghe Observatory for the March 1st to March 15th time period are shown in Table 4.2. Overall, the performance of the 12-km AER-All simulation is comparable with or better than the 36km simulation, with improvements in all the meteorological fields and several trace gases (CO, SO_2, NO_y). Considerable improvements are obtained in temporal correlations of 2-meter relative humidity (RH_{2m}) and surface level wind speed, mainly owing to the better-resolved geographic information on land use, topography, soil type, and vegetation cover. Better representation in meteorological variables leads to enhanced correlations and smaller biases in trace gases such as CO and SO_2 that are mainly influenced by meteorology and emissions. Simulated aerosol optical properties (aerosol optical depth, scattering coefficient and absorption coefficient) from the 12km AER-ALL simulation are similar to those from the 36 km simulation and reasonably represent observed temporal and spatial variations. Simulated aerosol optical properties were evaluated against observations at Xianghe Observatory and AERONET stations in Chapter 3, section 3.2.1 (See Figure 3.6, Figure 3.7, and Table 3.2) and only a summary will be presented here. In general, WRF-Chem captured the buildup and decrease of aerosols at Xianghe, however underpredicted AOD on highly polluted days. Comparisons between simulated AOD from WRF-Chem and observations at 10 AERONET stations showed that 8 out of 10 stations had temporal correlations higher than 0.5 and 7 out of 10 stations had biases less than 30%.

Table 4.2. Comparison of statistics of 12 km and 36 km simulations

	Correlation 12km	**Bias 12km**	**Correlation 36km**	**Bias 36km**
T_{2m} (K)	0.93	-1.05	0.91	-1.81
P_{sfc} (hPa)	0.93	0.10	0.93	0.12
RH_{2m} (%)	0.83	6.68	0.68	5.61
Wind speed (m/s)	0.63	0.76	0.41	0.92
CO (ppm)	0.68	-0.28	0.43	-0.35
SO_2 (ppb)	0.54	-7.14	0.38	-7.26
NO (ppb)	0.46	0.54	0.47	0.10
NOy (ppb)	0.59	-1.16	0.43	-2.28
O_3 (ppb)	0.73	-1.36	0.72	1.14

In order to illustrate the impact of the AIE realized through changes in clouds and precipitation, we will focus on two periods with large-scale synoptic cloud and precipitation features in this study. The time periods for these two case studies are March 1 to March 2 (case study A), and March 10th (case study B). One major difference between these two cases is that the clouds are optically thinner and higher in Case study A than Case study B, which leads to different responses in meteorology and atmospheric composition that would be discussed in details.

4.3.1 Case Study A

As seen from the 1° ×1° Level 3 MODIS Aqua Liquid Cloud Optical Depth (COD) product (Figure 4.1, left column), on March 1, large-scale clouds with COD greater than 40 covered several provinces in southern China including from west to east Yunnan, Sichuan, Guizhou, Guangxi, Hunan, Guangdong and Fujian with maximum values exceeding 60 in Fujian Province near the southeastern coast. On March 2, cloud cover over the southeastern coast expanded and thickened over Fujian and Zhejiang Provinces, and diminished over Guizhou, Sichuan, and Hunan Provinces. The spatial correlation between the modeled (Figure 4.1, right columns) and observed COD is ~0.5 on both days indicating that the AER-All simulation has moderate success in capturing the location and thickness of clouds on this day. The model also captured the increase in clouds over southeastern China between the 1st and 2nd.

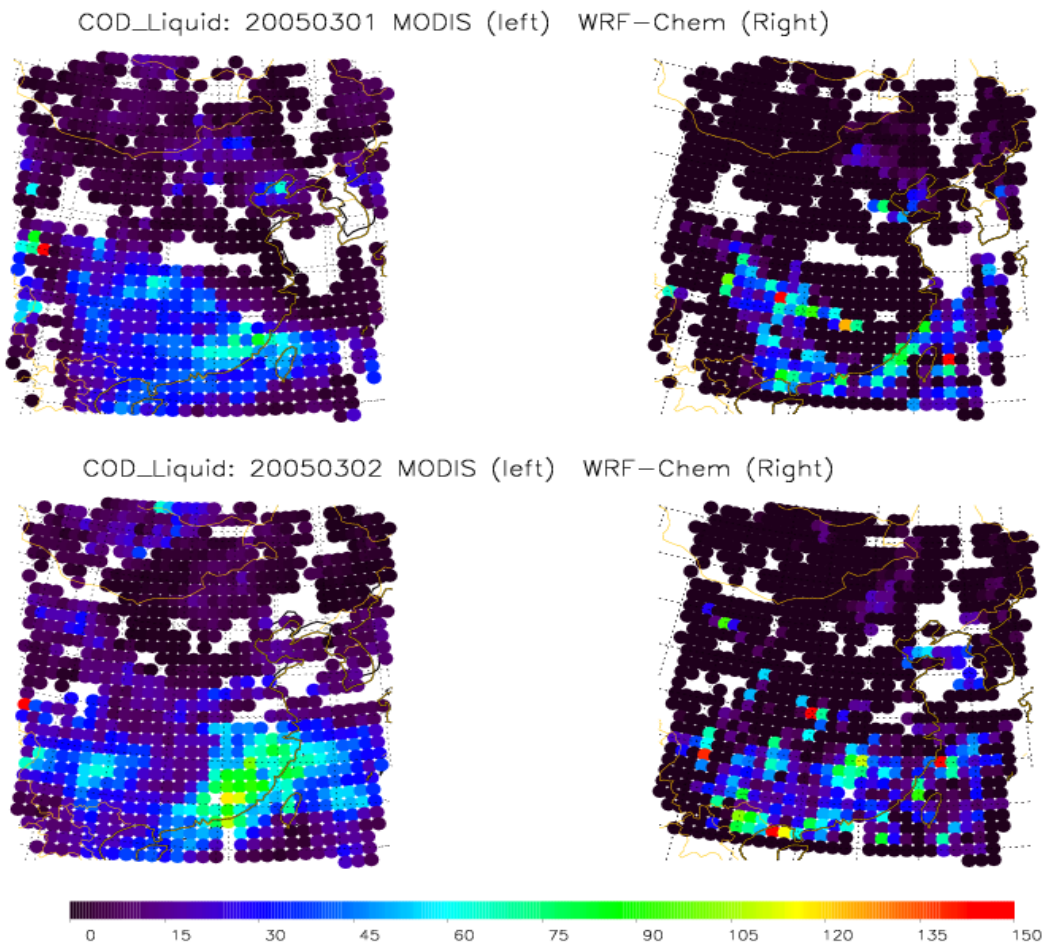

Figure 4.1. Liquid Cloud Optical Depth (COD) from WRF-Chem AER-All simulation (Right) and Liquid COD from MODIS (Aqua) L3 product (left) at MODIS Aqua overpass time on March 1 and March 2. The simulated liquid COD from the WRF-Chem AER-All simulation is extracted at the locations where MODIS Level 3 has values. The blank represents grids without MODIS L3 data. MODIS data is downloaded from http://modis-atmos.gsfc.nasa.gov/MOD08_D3/

Along with the appearance of thick clouds, precipitation is observed forming in southern China on March 1 and moving to the southeastern coast by March 2 (Figure 4.2, left column). Modeled daily precipitation from the WRF-Chem AER-All

simulation at the same locations (Figure 4.2, right column) shows fairly good agreement with observations in terms of magnitude and location (spatial correlation of ~0.5 for both days) although mean precipitation amounts at locations with greater than 5 mm of precipitation are overestimated by 6.4 mm and the spatial extent of >5 mm of precipitation is overestimated by 78% (128 model stations versus 72 observed stations). In addition, the model has spurious precipitation in southwest China on the 2nd.

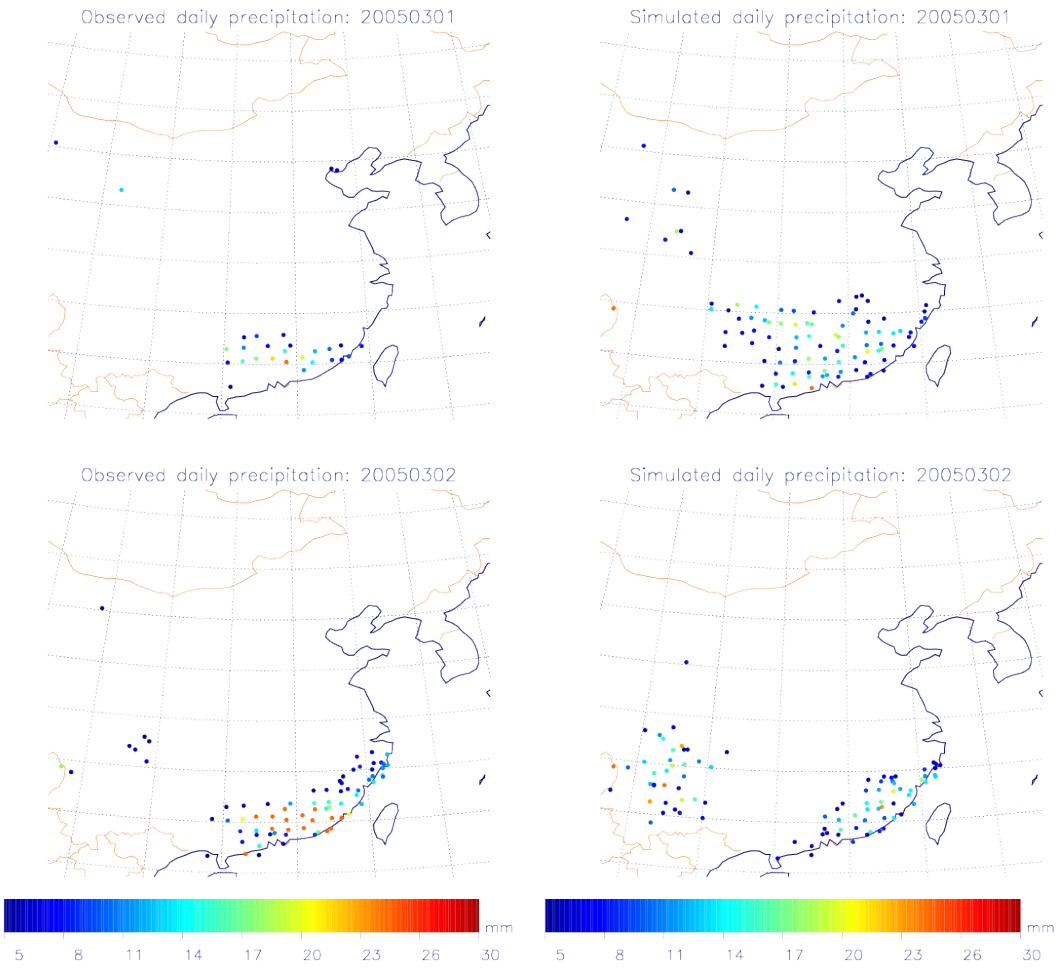

Figure 4.2. Daily total precipitation (mm) from weather station observations (left) and WRF-Chem AER-All simulation (right) from 03/01/2005 and 03/02/2005. (Precipitation data set is developed by Climate Data Center of the National

Meteorological Center of the China Meteorological Administration http://cdc.cma.gov.cn/, as discussed in Zhai et al. [2005])

The reasonable representation by the WRF-Chem AER-All simulation of the liquid COD and precipitation associated with these two case studies makes it possible to examine the impact of aerosol direct and indirect effects on meteorological variables and atmospheric components. Figure 4.3 shows spatial maps of hourly average surface shortwave (SW) radiation, 2-meter temperature, planetary boundary layer height (PBLH), 10-meter wind speed, and temperature lapse rate between 700 hPa and the surface from the AER-All simulation (left column), and their changes due to direct (center column) and indirect (right column) effects. Surface SW radiation decreases throughout the domain due to the aerosol direct effect (Figure 4.3b) with maximum reductions of ~90 W/m^2 over eastern China where surface $PM_{2.5}$ concentrations are highest (Figure 4.5a). The decrease in surface SW radiation due to the direct effect is offset at some locations (e.g., northeastern coast of China) by the aerosol semi-direct effect. The single scattering albedo (SSA) from AER-All simulation in this region is ~0.72, while the domain mean is 0.89, indicating there is strong absorbing effect in this region. The SSA is reduced from 0.92 to 0.72 by including the direct/semi-direct effects in this region; therefore the strong absorbing effect heats the atmosphere, evaporates clouds, and allows more radiation to reach the surface. Reduced values of cloud optical depth can also be found along the northeast coast (Figure 4.4b) where surface short wave radiation increases due to the AIE.

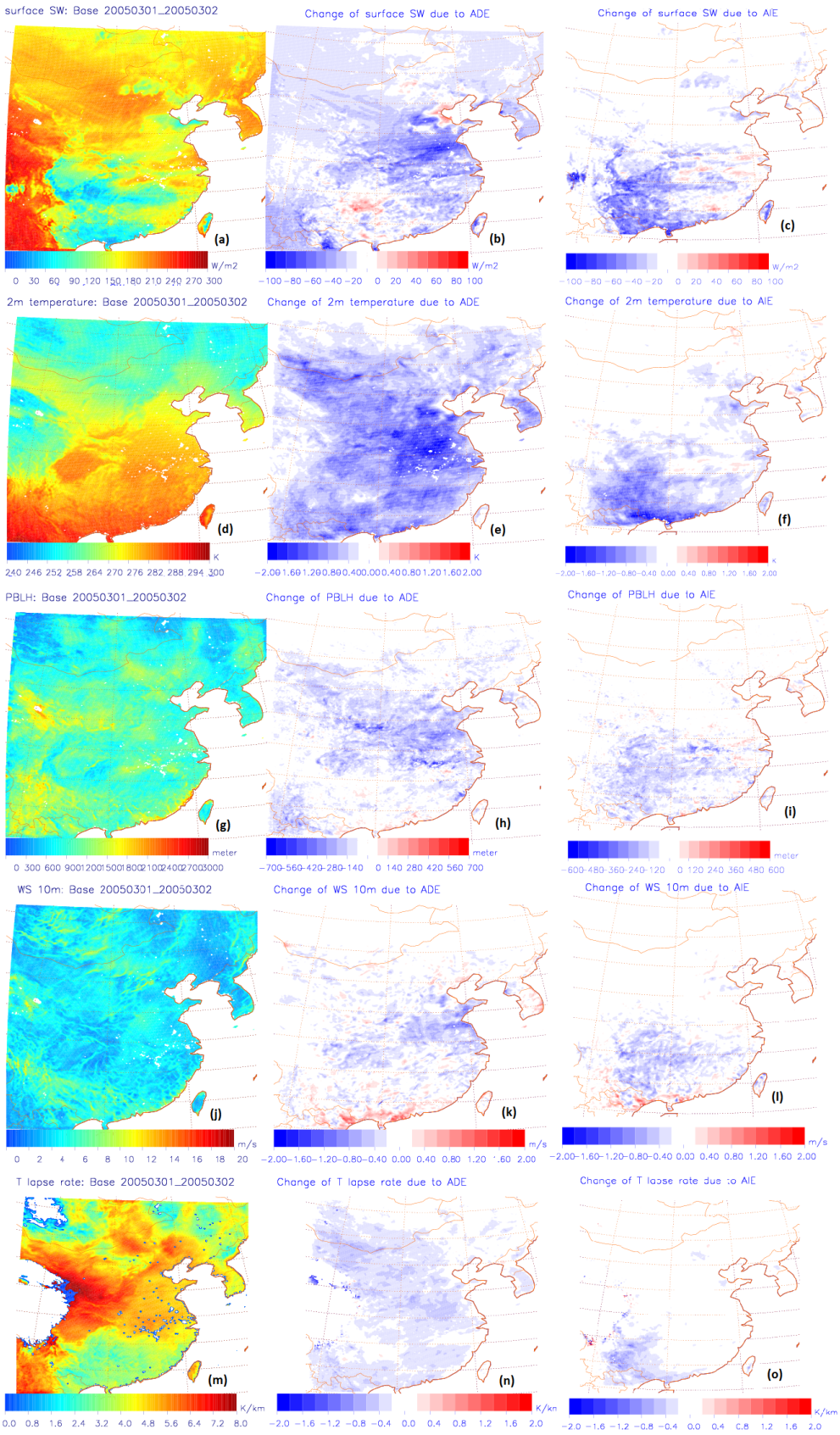
surface SW: Base 20050301_20050302
Change of surface SW due to ADE
Change of surface SW due to AIE
(a)
(b)
(c)
W/m2
0 30 60 90 120 150 180 210 240 270 300
−100 −80 −60 −40 −20 0 20 40 60 80 100
2m temperature: Base 20050301_20050302
Change of 2m temperature due to ADE
Change of 2m temperature due to AIE
(d)
(e)
(f)
K
240 246 252 258 264 270 276 282 288 294 300
−2.00 −1.60 −1.20 −0.80 −0.40 0.00 0.40 0.80 1.20 1.60 2.00
PBLH: Base 20050301_20050302
Change of PBLH due to ADE
Change of PBLH due to AIE
(g)
(h)
(i)
meter
0 300 600 900 1200 1500 1800 2100 2400 2700 3000
−700 −560 −420 −280 −140 0 140 280 420 560 700
−600 −480 −360 −240 −120 0 120 240 360 480 600
WS 10m: Base 20050301_20050302
Change of WS 10m due to ADE
Change of WS 10m due to AIE
(j)
(k)
(l)
m/s
0 2 4 6 8 10 12 14 16 18 20
−2.00 −1.60 −1.20 −0.80 −0.40 0.00 0.40 0.80 1.20 1.60 2.00
T lapse rate: Base 20050301_20050302
Change of T lapse rate due to ADE
Change of T lapse rate due to AIE
(m)
(n)
(o)
K/km
0.0 0.8 1.6 2.4 3.2 4.0 4.8 5.6 6.4 7.2 8.0
−2.0 −1.6 −1.2 −0.8 −0.4 0.0 0.4 0.8 1.2 1.6 2.0

Figure 4.3. Spatial distribution of hourly surface shortwave radiation (a), 2-meter temperature (d), PBLH (g), 10-meter wind speed (j) and temperature lapse rate between 700hPa and the surface (m) from AER-All simulation, and their corresponding changes due to the aerosol direct effect (b, e, h, k, and n) and the indirect effect (c, f, I, l, and o) from March 1 to March 2, 2005.

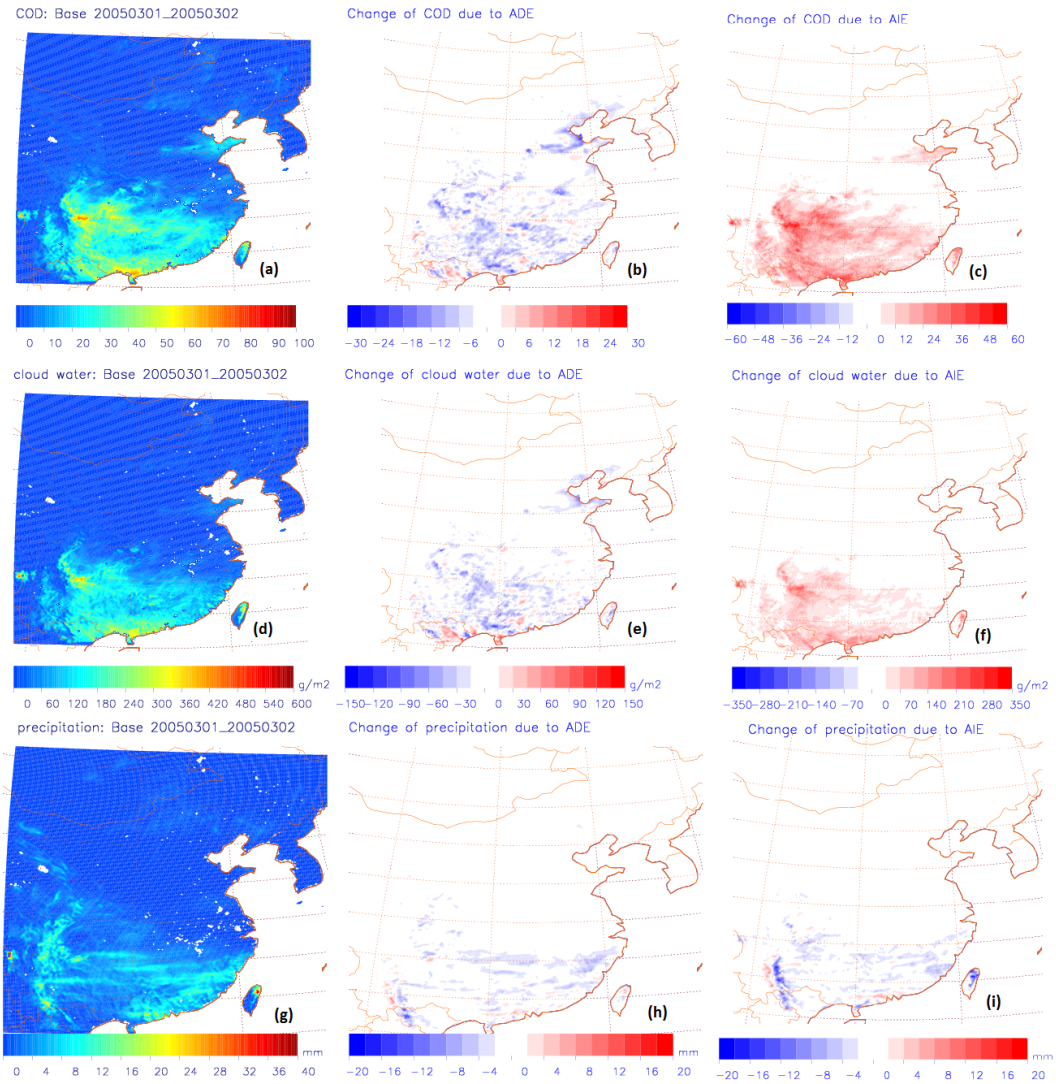

Figure 4.4. Spatial distribution of hourly liquid cloud optical depth (a), cloud water pathway (d) and precipitation (g), and their corresponding changes due to the aerosol

direct effect (b, e, and h) and the aerosol indirect effect (c, f, and i) from March 1 to March 2, 2005.

Surface SW radiation also decreases through much of the domain due to the aerosol indirect effect (Figure 4.3c) as increases in cloud optical depth (Figure 4.4b) lead to decreases in surface SW radiation. The indirect effect and associated decreases in surface shortwave radiation are strongest over regions with high cloud optical depth as opposed to regions with high pollutant levels. In general, the magnitudes of direct and indirect effects on the surface SW radiation are comparable but are focused on different locations. Decreases in 2-meter temperature, PBLH, 10-meter wind speed and 700 hPa to surface temperature lapse rate (e.g., *Storer et al*. 2014) are consistent with the changes in surface radiation and also previous studies [*Zhang et al*., 2015; *Wang et al*., 2016]. Reductions in PBLH, temperature lapse rate and surface wind speed indicate a more stabilized atmosphere with less convection and weaker winds. Therefore with this model configuration, the direct effect causes clouds to get thinner and contain less water (Figure 4.4b and 4.4e) and precipitation to decrease by 28% over regions with daily precipitation higher than 1 mm (Figure 4.4h). The aerosol indirect effect also inhibits convection primarily due to the modification of cloud microphysics due to the aerosols. In this case, the AIE increases cloud droplet numbers, cloud optical depth (Figure 4.4c) and cloud water pathway (Figure 4.4f) over southwestern and southern China by 88%, 40%, and 50% respectively, leading to a suppression of precipitation of 29%. (Figure 4.4i). The sign of the precipitation change due to the indirect effect differs from that found by *Zhang et al.* [2015]. They

found an increase in precipitation over southern China due to the AIE possibly because over this clean region the prescribed cloud droplet concentrations used in their sensitivity run were larger than the prognostic concentrations used in their base run. The result of this difference was an increase in precipitation in the base run, which included the indirect effect.

Aerosol direct and indirect effects influence air quality via changes in meteorological variables discussed above and changes in chemical processes. Figure 4.5a shows that model surface $PM_{2.5}$ concentrations are highest over eastern China (up to 250 $\mu g/m^3$) and Sichuan Basin (up to 200 $\mu g/m^3$). Due to the thinner PBLH, less convection, weaker winds, and less wet scavenging from precipitation induced by the direct effect, surface concentrations of $PM_{2.5}$ and its major components including primary and secondary aerosols are enhanced, especially over the most polluted regions (Figure 4.5, central column). However, the indirect effect shows diverse impacts on surface $PM_{2.5}$ due to competing processes involved. First, the increase in cloud optical depth and cloud water content due to the AIE stabilizes the atmosphere leading to a decrease in PBLH, wind speed, and ventilation resulting in an increase in surface $PM_{2.5}$ concentrations; secondly, suppressed precipitation causes less wet scavenging of aerosols; thirdly, with this model configuration, prognostic aerosols are removed from the air when activated as Cloud Condensation Nuclei (CCN). This removal leads to a decrease in aerosol concentrations, which is much larger in the AER-All case than in the no_AIE case due to the much higher background aerosol concentrations in the AER-All simulation. The first and second processes exert positive feedbacks on $PM_{2.5}$ concentrations while the third process acts in the

opposite direction. Regions with thick clouds such as southwestern China and coastal areas (Figure 4.1) are dominated by the third effect, while the first and second effects are most important in regions with high $PM_{2.5}$ concentrations such as central China. Comparing the magnitude of changes due to direct (Figure 4.5, central column) and indirect effects (Figure 4.5, right column) for different PM components, the primary aerosols (dust, OC) are most affected by the direct effect, while concentrations of secondary aerosols (sulfate and nitrate) are more sensitive to indirect effects because they are more hygroscopic than dust and OC [*Pringle et al*., 2010]. The hygroscopic parameters used in WRF-Chem are 0.5 for sulfate and nitrate aerosols and 0.14 for dust and OC.

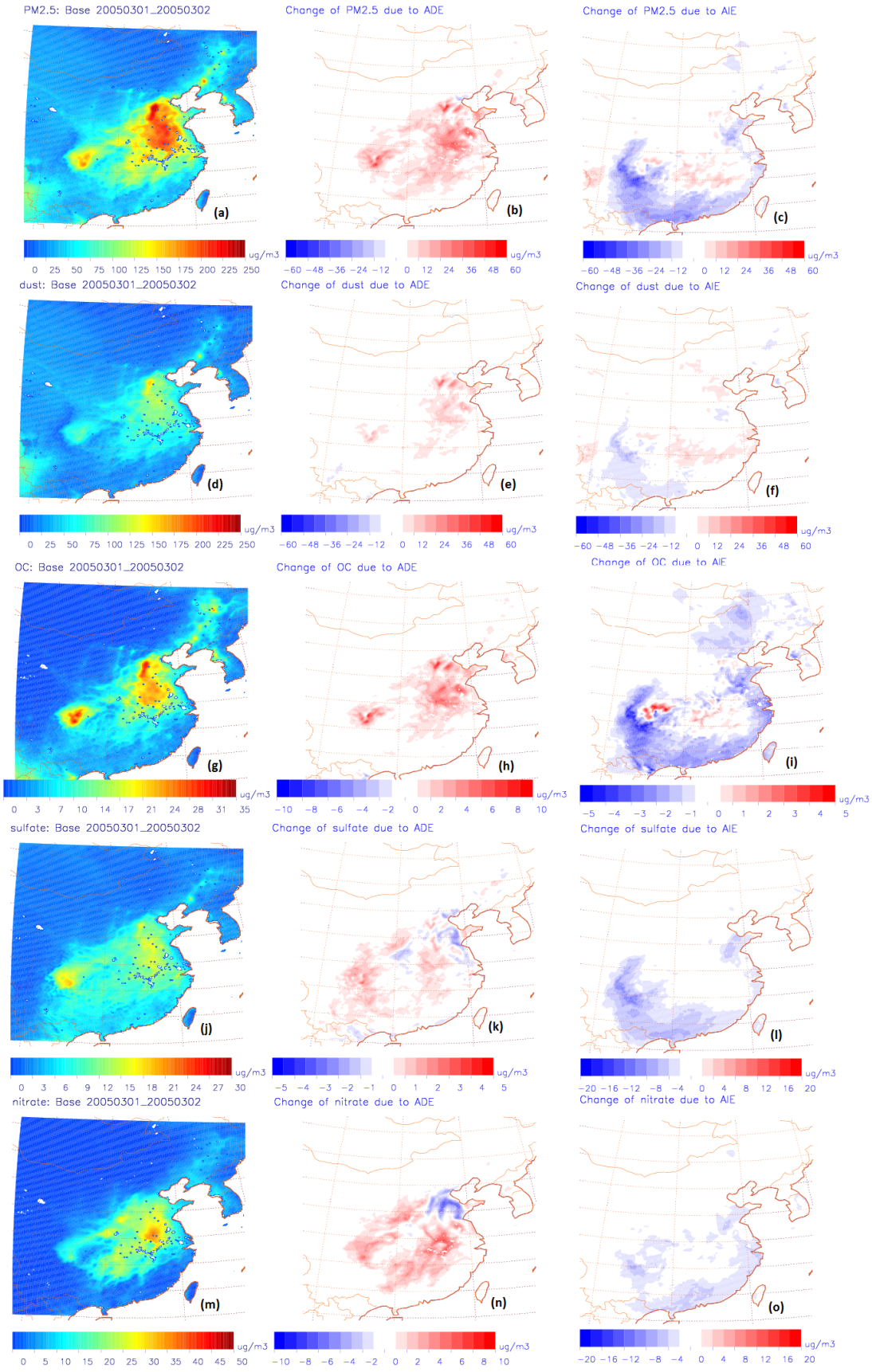
PM2.5: Base 20050301_20050302
Change of PM2.5 due to ADE
Change of PM2.5 due to AIE
(a)
(b)
(c)
ug/m3
0 25 50 75 100 125 150 175 200 225 250
−60 −48 −36 −24 −12 0 12 24 36 48 60
dust: Base 20050301_20050302
Change of dust due to ADE
Change of dust due to AIE
(d)
(e)
(f)
OC: Base 20050301_20050302
Change of OC due to ADE
Change of OC due to AIE
(g)
(h)
(i)
0 3 7 10 14 17 21 24 28 31 35
−10 −8 −6 −4 −2 0 2 4 6 8 10
−5 −4 −3 −2 −1 0 1 2 3 4 5
sulfate: Base 20050301_20050302
Change of sulfate due to ADE
Change of sulfate due to AIE
(j)
(k)
(l)
0 3 6 9 12 15 18 21 24 27 30
−5 −4 −3 −2 −1 0 1 2 3 4 5
−20 −16 −12 −8 −4 0 4 8 12 16 20
nitrate: Base 20050301_20050302
Change of nitrate due to ADE
Change of nitrate due to AIE
(m)
(n)
(o)
0 5 10 15 20 25 30 35 40 45 50
−10 −8 −6 −4 −2 0 2 4 6 8 10
−20 −16 −12 −8 −4 0 4 8 12 16 20

Figure 4.5. Spatial distributions of hourly concentrations of surface total PM2.5 (a), dust aerosols (d), organic carbon (g), sulfate (j) and nitrate (m), and their corresponding changes due to the aerosol direct effect (b, e, h, k, and n) and the indirect effect (c, f, i, l, and o) from March 1 to March 2, 2005.

As for ozone and CO, two major gaseous air pollutants, the impacts of the aerosol direct and indirect effects are quite different. The hourly averaged surface ozone and CO concentrations are shown in Figure 4.6a and 4.6d. With a relatively long lifetime in the atmosphere (~ 2 months), CO is chemically stable and mainly influenced by meteorological conditions, while ozone is a secondary pollutant and more chemically active in the troposphere. The contrasting responses of ozone and CO to the ADE are shown in Figures 4.6b and 4.6e. Ozone is reduced since decreases in its concentration due to a slowing of its formation rate via photolysis are larger than increases in its concentration due to decreases in PBL height and increases in stability, while CO concentrations increase due to the decrease in PBL height and increase in stability. The effect of the AIE on O_3 (Figure 4.6c) is opposite in sign to the effect of the ADE on O_3, and it impacts different regions. The indirect effect increases ozone concentrations along the south coast, including Guangxi, Guangdong, Fujian, and the southern part of Hunan and Jiangxi Provinces, with increases of cloud water and cloud optical depth. $O(^3P)$ generated from NO_2 photochemistry at wavelengths < 390nm is a major source of tropospheric ozone formation. Therefore, increases in the NO_2 photolysis rate ($j(NO_2)$) leads to more ozone production. The regional averaged vertical profile of $j(NO_2)$ and its change due to the AIE are shown

in Figure 4.7. Increases of $j(NO_2)$ are found over this region with an average enhancement of 34% at the surface and 10% throughout the atmosphere. This result is somewhat surprising as several previous studies using radiative transfer models have found that clouds reduce $j(NO_2)$ [*Liao et al*., 1999; *Wild et al*., 2000; *Liu et al*., 2006]. However, these studies do not consider the impact of changing clouds and aerosols at the same time. In this region and this case study, COD is enhanced but AOD is decreased as air-borne aerosols are activated and incorporated into clouds (see Figure 4.7). The vertically integrated COD increases from 12.4 to 27.8 when the AIE is included, while the vertically integrated AOD at 300 nm decreases from 3.4 to 1.8 with maximum decreases at ~875 hPa. Changes in COD and AOD have opposing impacts on surface $j(NO_2)$. *Wild et al*. [2000] calculated $j(NO_2)$ in the presence of multilayer clouds of COD = 15 using an offline Fast-J model, and found that for a solar zenith angle of 0°, $j(NO_2)$ decreased about 14% compared to cloud-free conditions. *Liu et al*. [2006] showed that the impact of increasing multilayer cloud optical depth (or cloud water) by 50% on the $j(NO_2)$ percentage change due to clouds is around 2% using Fast-J. However, *He and Carmichael* [1999] applied a 1-D comprehensive atmospheric chemistry model coupled with a radiative transfer scheme to test the sensitivity of photolysis rates to aerosol loadings and found that $j(NO_2)$ can be up to 50% lower with 50% more aerosol loadings. Therefore, substantial decreases of AOD (~46% in this case) could lead to increases in $j(NO_2)$ and therefore surface ozone concentrations over coastal southeastern China.

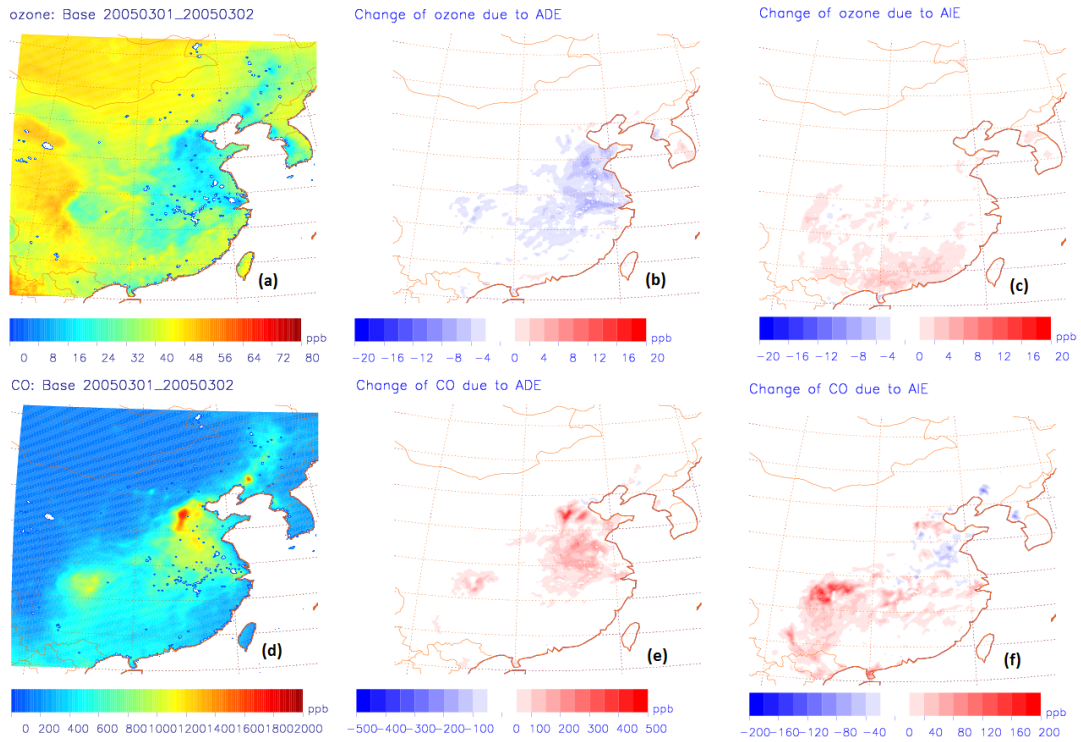

Figure 4.6. Spatial distributions of hourly concentrations of surface concentration of ozone (a) and CO (d), and their corresponding changes due to the aerosol direct effect (b and e) and indirect effects (c and f) from March 1 to March 2.

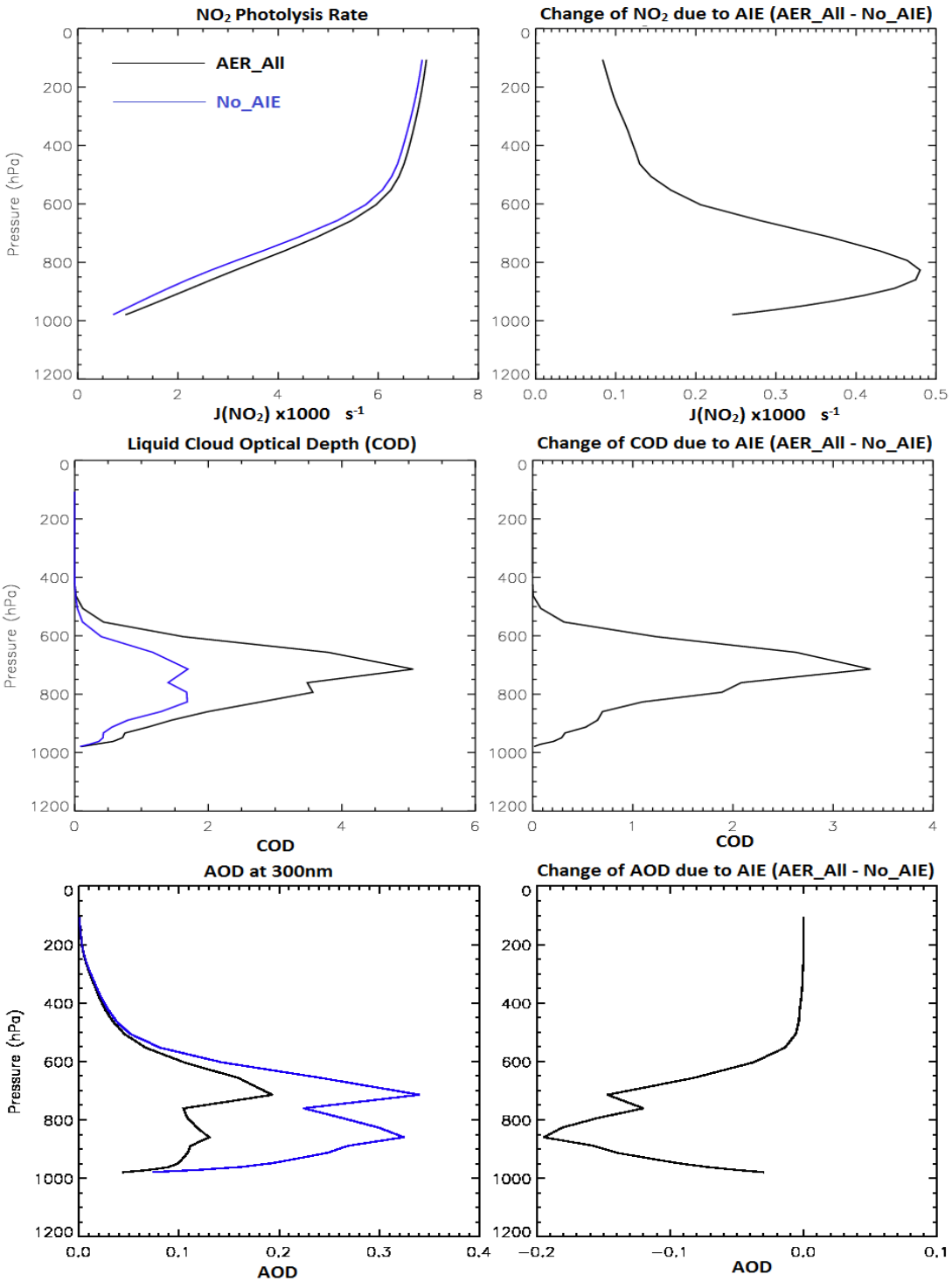

Figure 4.7. Mean vertical profiles of 24-hour averaged NO_2 photolysis rate (top panels), liquid cloud optical depth (COD) (center panels), and aerosol optical depth

(AOD) (bottom panels) averaged over coastal southeastern China (110° E – 118° E, 22° N – 27° N) for March 1 to March 2, 2005. Values are shown in the left panels and changes due to the AIE are shown in the right panels.

The impact of opposing changes in COD and AOD on surface actinic flux, the driving factor determining $j(NO_2)$, is examined using the 1-D offline TUV (Tropospheric Ultraviolet and Visible Radiation) model (http://cprm.acom.ucar.edu/Models/TUV/Interactive_TUV/). The TUV model calculates the NO_2 photolysis rate based on the following input variables: wavelength range, solar zenith angle, overhead ozone column, surface albedo, cloud base and top heights, COD, AOD, and aerosol single scattering albedo. We performed two tests using the input values specified in Table 4.3 to estimate the sensitivity of the surface NO_2 photolysis rate to AOD and COD. In these tests, the values of AOD and COD were taken from the AER-All and No_AIE simulations while the values for the other input variables were held fixed at levels typical for this region during this time period.

Table 4.3. Values of input variables and calculated $j(NO_2)$ for two TUV model tests *

	AOD at 300nm	COD	Simulated from	$j(NO_2)$ s^{-1}
Test_A	1.8	27.8	AER-All	2.48×10^{-3}
Test_B	3.4	12.4	No_AIE	2.37×10^{-3}

*: Wavelength range=280-400nm, solar zenith angle=30°, overhead ozone column=300 DU, surface albedo=0.1, cloud base=0.1km, cloud top=5km, aerosol single scattering albedo=0.9.

From Table 4.3, it can be seen that the surface j(NO_2) is larger in Test A that includes AOD and COD values from the AIE simulation than in Test B that includes AOD and COD values from the NO_AIE simulation. This result indicates that for input values chosen in Table 4, the increase in surface j(NO_2) due to a lower AOD is larger than the decrease in flux due to a higher COD and supports our belief that the AIE is an important cause of the increases in j(NO_2) in this region during this event.

4.3.2 Case Study B

On March 10, the MODIS Aqua L3 product showed a large region of southeastern China (Zhejiang, Fujian, Guangdong, Guangxi, Hunan, and Jiangxi Provinces) covered by clouds (Figure 4.8, left). The WRF-Chem AER-All run reproduced the observed spatial distribution of the COD moderately well with a domain-wide spatial correlation of 0.52.

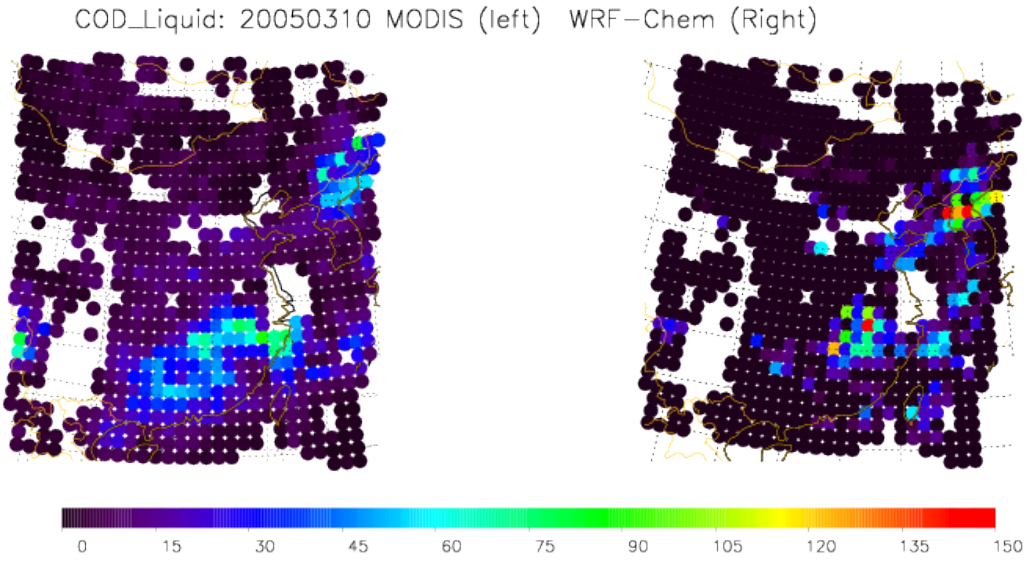

Figure 4.8. Liquid Cloud Optical Depth (COD) from WRF-Chem AER-All simulation (Right) and Liquid COD from MODIS (Aqua) L3 product at MODIS Aqua overpass time on March 10.

Similar to Case Study A, the spatial extent of the cloud cover from the model is larger than observed and the magnitude of model precipitation showed a high bias of 8.6 mm over regions where the observation showed more than 5 mm of precipitation (Figure 4.9)

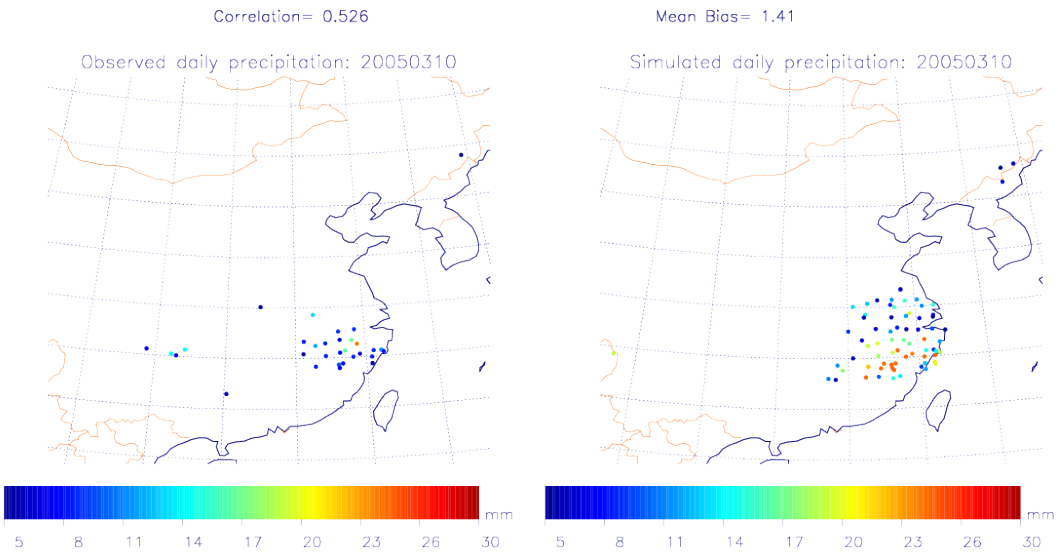

Figure 4.9. Daily total precipitations from weather station observations (left) and WRF-Chem AER-All simulation (right) from March 10, 2005.

As in Case Study A, surface shortwave radiation, 2-m temperature, PBL height, wind speed, and lapse rate usually decrease due to the aerosol direct and indirect effects although the change due to the AIE is relatively weak and occasionally slightly

positive for some variables (i.e., surface wind speed, PBLH) in regions with high aerosol loadings (Figure 4.10). For example, the change of surface temperature is less negative due to the indirect effect (~ -0.5 °C) than the direct effect (~ -2 °C) over the Sichuan Basin where $PM_{2.5}$ levels are extremely high (~350 $\mu g/m^3$), because the cooling effect due to less shortwave radiation reaching the surface is mitigated by the warming effect associated with enhanced aerosol absorbing capabilities (reduced SSA). *Zhang et al*. [2015] also found that the aerosol direct effect plays a larger role than the AIE in changing conditions over highly polluted areas. Since the Sichuan Basin is warmer than its surroundings (Figure 4.10d) and experiences a smaller temperature decrease, the temperature gradient is enhanced which causes increases in wind speed (up to 12%, Figure 4.10l) and mixing, that smooth out the pollutant spatial distribution. This is one possible cause of the decreases in the concentrations of all aerosol components (Figure 4.11, right column) in Sichuan Basin, and the increases in surrounding regions due to the indirect effect. Over regions with thick cloud cover, i.e., Jiangsu and Anhui Provinces in eastern China; Hebei, Shanxi, and Shangdong Provinces in Northern China; and North Korea and South Korea, concentrations of secondary aerosols decrease due to the AIE as discussed in case study A, however, the magnitudes of these changes are slightly smaller than the changes due to the direct effect, probably because of the higher $PM_{2.5}$ concentrations in case study B than in case study A.

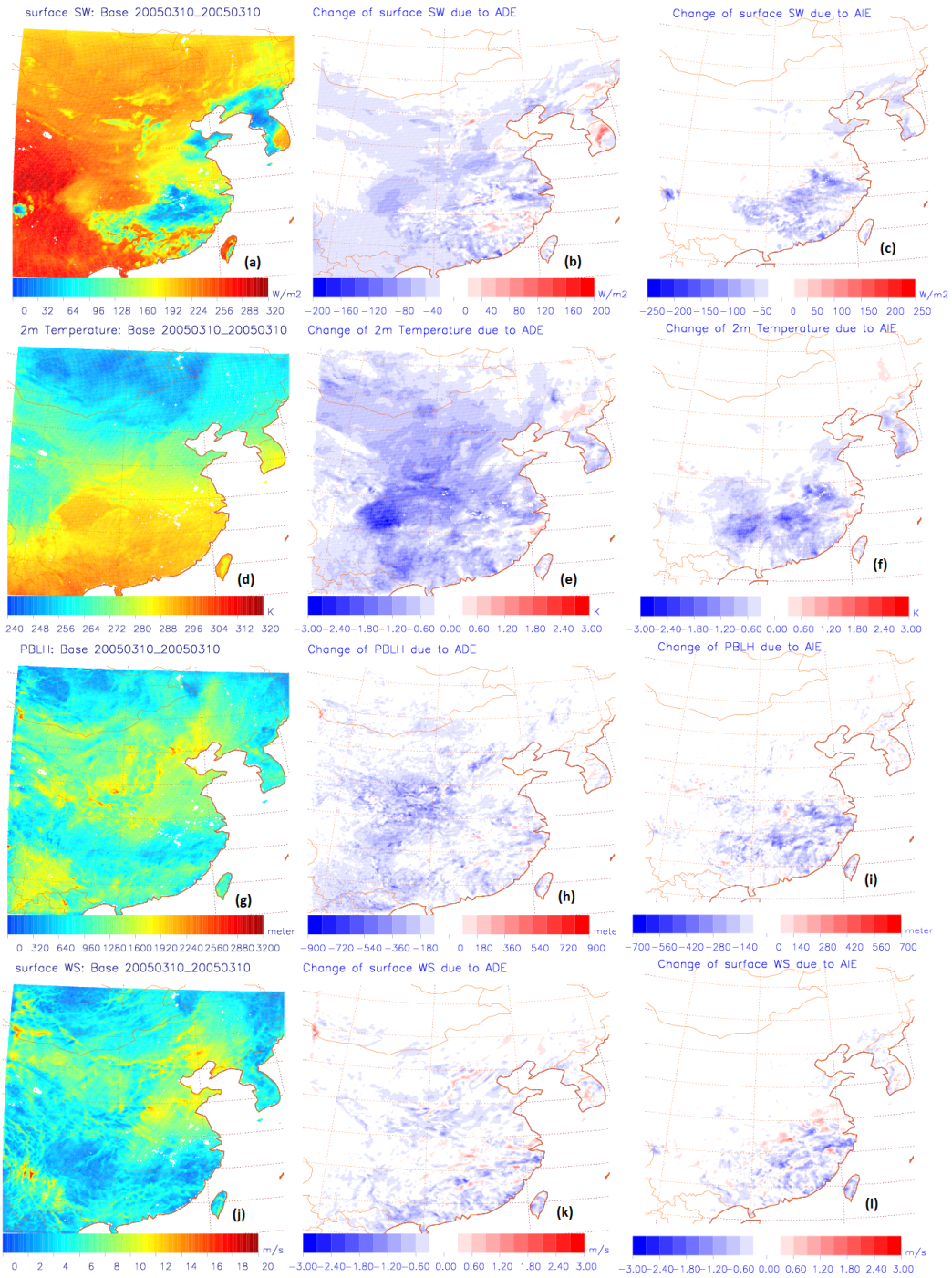

Figure 4.10. Spatial distribution of hourly surface shortwave radiation (a), 2-meter temperature (d), PBLH (g) and 10-meter wind speed (j) from AER-All simulation, and their corresponding changes due to the aerosol direct effect (b, e, h, and k) and the indirect effect (c, f, I, and l) on March 10, 2005.

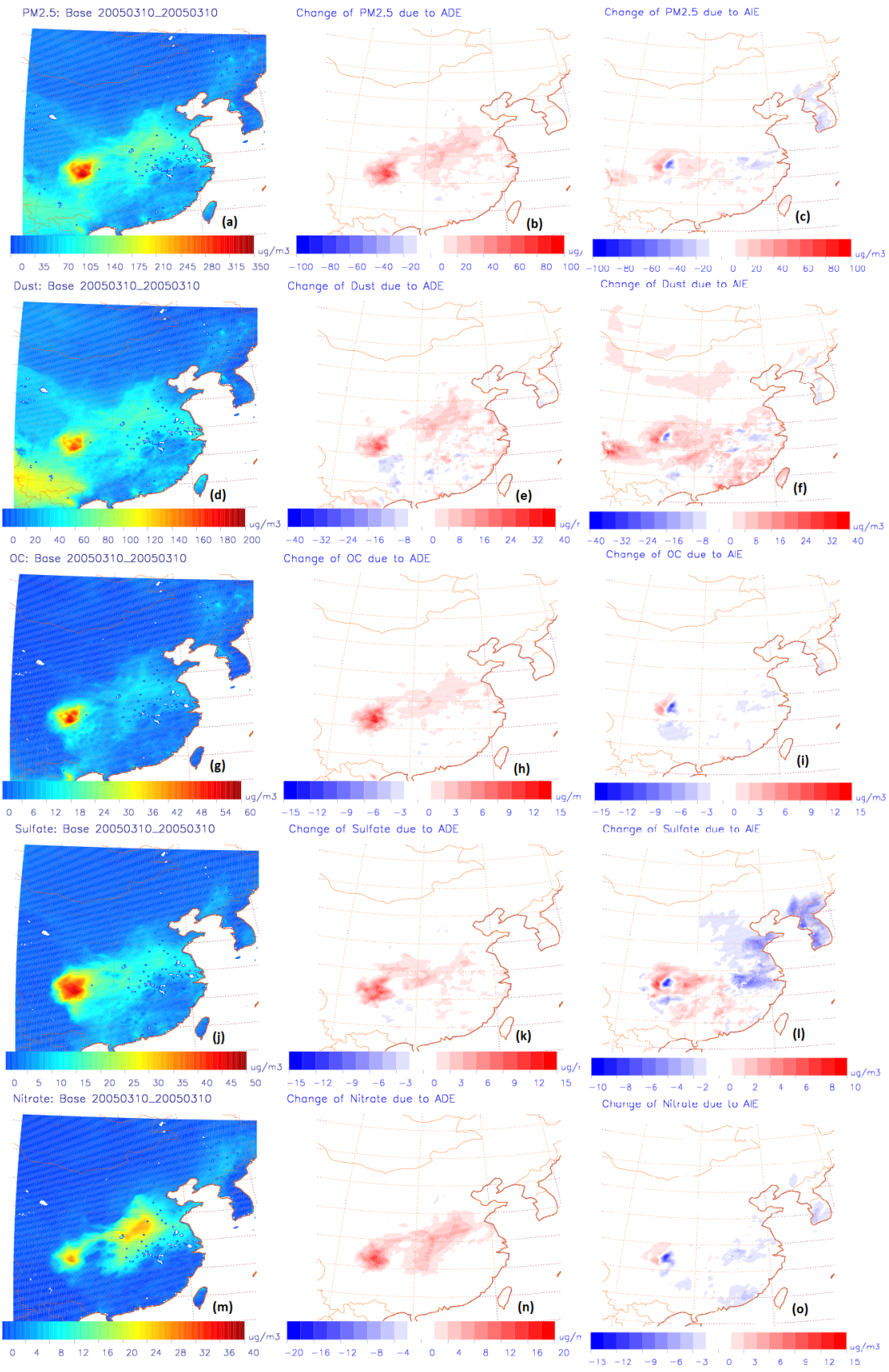
PM2.5: Base 20050310_20050310
Change of PM2.5 due to ADE
Change of PM2.5 due to AIE
(a)
(b)
(c)
ug/m3
0 35 70 105 140 175 210 245 280 315 350
−100 −80 −60 −40 −20 0 20 40 60 80 100
Dust: Base 20050310_20050310
Change of Dust due to ADE
Change of Dust due to AIE
(d)
(e)
(f)
ug/m3
0 20 40 60 80 100 120 140 160 180 200
−40 −32 −24 −16 −8 0 8 16 24 32 40
OC: Base 20050310_20050310
Change of OC due to ADE
Change of OC due to AIE
(g)
(h)
(i)
ug/m3
0 6 12 18 24 30 36 42 48 54 60
−15 −12 −9 −6 −3 0 3 6 9 12 15
Sulfate: Base 20050310_20050310
Change of Sulfate due to ADE
Change of Sulfate due to AIE
(j)
(k)
(l)
ug/m3
0 5 10 15 20 25 30 35 40 45 50
−15 −12 −9 −6 −3 0 3 6 9 12 15
−10 −8 −6 −4 −2 0 2 4 6 8 10
Nitrate: Base 20050310_20050310
Change of Nitrate due to ADE
Change of Nitrate due to AIE
(m)
(n)
(o)
ug/m3
0 4 8 12 16 20 24 28 32 36 40
−20 −16 −12 −8 −4 0 4 8 12 16 20
−15 −12 −9 −6 −3 0 3 6 9 12 15

Figure 4.11. Spatial distributions of hourly concentrations of surface total PM2.5 (a), dust aerosols (d), organic carbon (g), sulfate (j) and nitrate (m), and their corresponding changes due to the aerosol direct effect (b, e, h, k, and n) and the indirect effect (c, f, i, l, and o) on March 10.

The dominant processes controlling the changes of ozone and CO (Figure 4.12) are still similar to case study A. However the change in O_3 due to the AIE is negative over regions with increased clouds in Case B, which is opposite the change in Case A. Figure 14 demonstrates the negative change of $j(NO_2)$ (~8%) from the surface up to 900 hPa where the COD is the highest. This decrease results in less formation of ozone at the surface and below the cloud. $j(NO_2)$ increases above the cloud due to the enhanced actinic flux from cloud reflectance of solar radiation. Similar to Case A, changes in AOD and COD are of opposite sign (Figure 4.13) and therefore have different impacts on actinic flux and $j(NO_2)$. For example, AOD at 300 nm is reduced by 6%, a value that is much smaller than the decrease in Case A, whereas COD increases by 500% (from 8.9 to 45.8), a value that is much higher than in Case A. Compared to Case Study A, the cloud heights in Case Study B are lower, therefore the aerosol loading above the cloud is not significantly affected, leading to smaller percentage changes in AOD than Case Study A. Hence, the dramatic enhancement of COD dominates over the small decrease of AOD, leading to the decrease of actinic flux $j(NO_2)$ below the cloud.

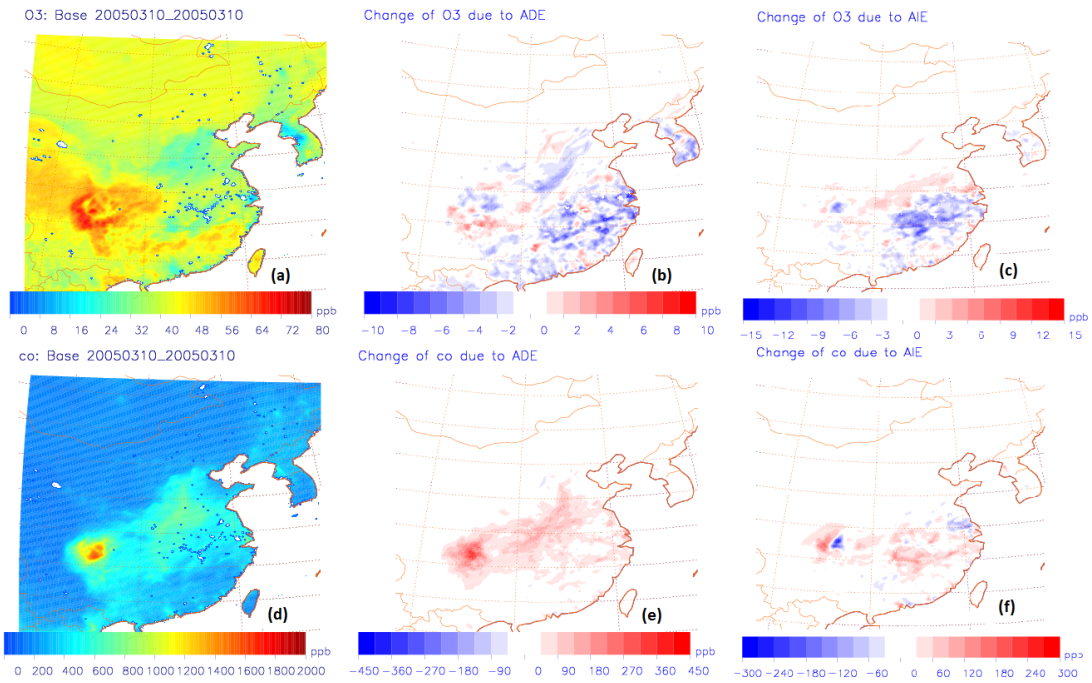

Figure 4.12. Spatial distributions of hourly concentrations of surface concentration of ozone (a) and CO (d), and their corresponding changes due to the aerosol direct effect (b and e) and indirect effects (c and f) on March 10.

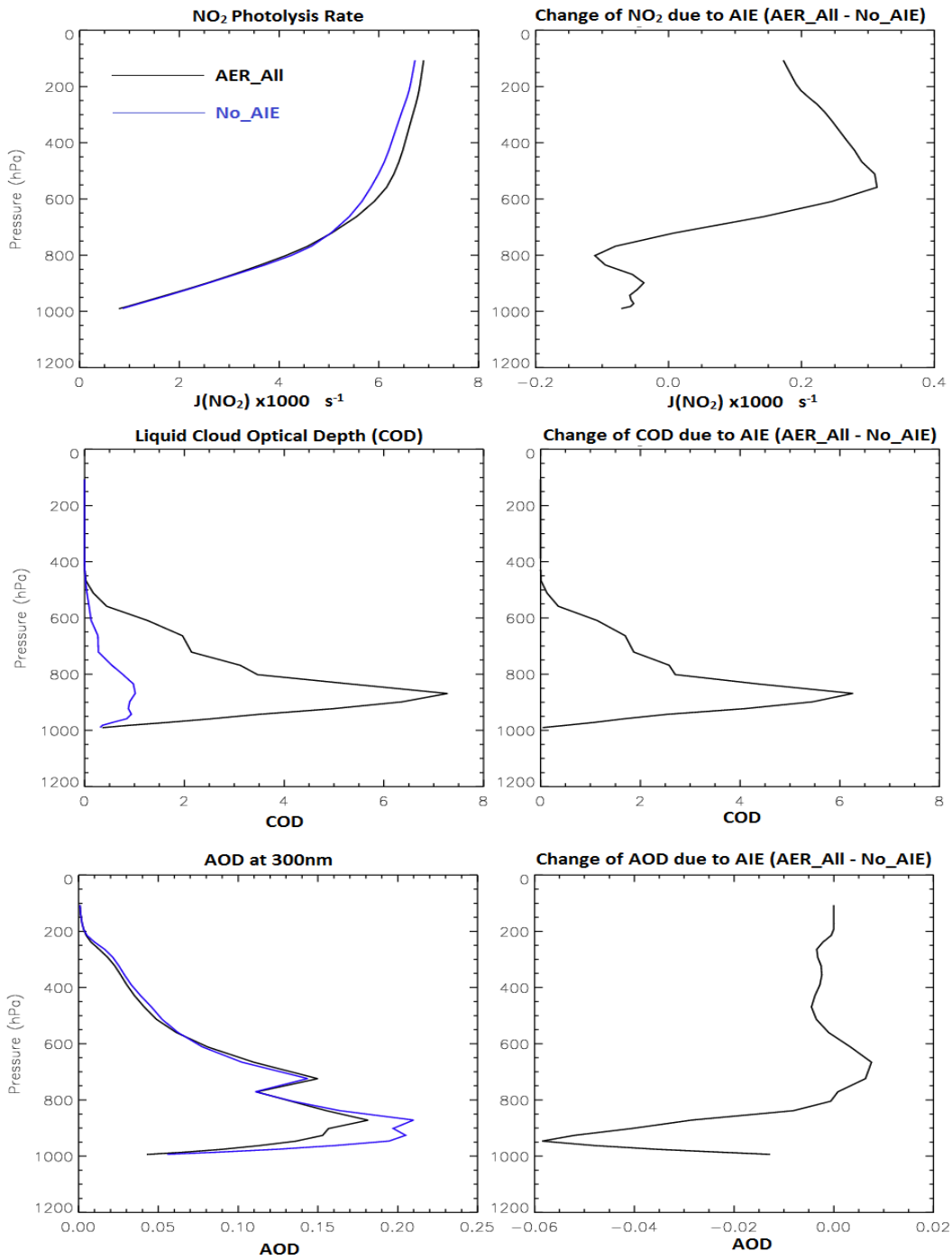

Figure 4.13. Mean vertical profiles of 24-hour averaged NO_2 photolysis rate (top), liquid COD (center), and AOD (bottom) from simulation AER-All (left column) and their changes due to the AIE (right column) over eastern part of China (115° E – 118° E, 28° N – 32° N) on March 10, 2005.

4.3.3 Sensitivity test of different treatments of CDNC in No_AIE simulation

As discussed in Case Study A, daily precipitation over southern China decreases due to increased cloud droplet numbers (88%) due to the indirect effect. The sign of the precipitation change due to the indirect effect differs from that found by *Zhang et al*. [2015] who found an increase in precipitation over southern China. The increase observed by *Zhang et al.* could be caused by differences in CDNC in the microphysics schemes between their simulations. Specifically, for this clean region, the prognostic CDNC used in their base run may be smaller than the prescribed constant CDNC used in their sensitivity run that did not include the indirect effect with the decrease in CDNC contributing to an increase in precipitation. Therefore, the difference in the sign of the precipitation change between this study and *Zhang et al*. may be due to subtle differences in how CDNC are prescribed in the sensitivity runs.

We performed sensitivity simulations to test the sensitivity of precipitation changes to the approach used to specify CDNC in the microphysics scheme. These simulations used the same input datasets, physical and chemical modules as in Table 1 for the Case Study A period (March 1st to March 2nd, 2005). The first sensitivity simulation (Test_1) applies the approach used in this study and prescribes a spatially and temporally uniform "pre-industrial" background aerosol concentration of 1×10^8 particles per kg dry air, ~1/100 of the present day values, in the cloud droplet activation module in WRF-Chem. The 1×10^8 particles are evenly divided (1×10^8 / (number of species × nbins)) as the number concentration for each species in each size bin. The activation module then calculates the CNDC based on the prescribed

background aerosols, and passes the CDNCs to the microphysics scheme. The second and third sensitivity simulations (Test_2a and Test_2b) apply the approach used in several previous studies (*Yang et al*., [2011], *Makar et al*., [2014], *Zhang et al.*, [2015]). In these simulations a constant cloud droplet concentration (1×10^{8} droplets per kg air for Test_2a and 250 droplets per cm^3 for Test_2b) is prescribed in the microphysics scheme for grid boxes where the cloud water mixing ratio is larger than 1×10^{-14} kg/kg air. When the cloud water mixing ratio is less than 1×10^{-14} kg/kg air, the CDNC is set to zero. The impact of aerosol indirect effect on precipitation is calculated by subtracting each sensitivity simulation from the AER-All simulation that generates cloud droplets from prognostic aerosol information.

Figure 4.14 shows the average daily precipitation of the AER-All simulation (top left) and the changes in precipitation due the indirect effect calculated from the three sensitivity simulations. In simulation Test_1, CDNC increase by 88% due to the AIE with increases in CDNC observed at 63% of grid boxes with non-zero changes in CDNC. Overall, precipitation amounts decrease by 29% (Figure 4.14, top right). In simulation Test_2a (Test_2b) CDNC decreases by 28% (increases by 48%) due to the AIE with increases in CDNC observed at 44% (23%) of grid boxes with non-zero changes in CDNC. Overall, precipitation amounts increase by 5.7% (11.2%) (Figure 4.14, bottom left and bottom right). Clearly, for each of these simulations, increases in CDNC are associated with decreases in precipitation and vice versa. Thus, sensitivity experiments that use a higher CDNC background for their "no_AIE" simulations (i.e., Test_2a and Test_2b) will be more likely to have an increase in precipitation due to the AIE than experiments that use a lower CDNC background.

Therefore, for these case studies with this model set up, we find that increases in aerosol loading from pre-industrial levels causes a decline in warm cloud precipitation and associated decreases in wet scavenging and increases in pollutant levels (i.e., a positive feedback). However, for more modest changes in aerosol levels, the results are more mixed and dependent on the value of prescribed CDNC. Finally, we note that while using the first approach is useful for assessing the impact of aerosols on precipitation and air quality because the microphysics "feel" the difference in aerosol concentrations between pre-industrial and current conditions, the second approach may be more consistent with previous studies with cloud resolving models that typically prescribe constant CDNC (e.g., Khairoutdinov and Yang [2013]). In the first approach pre-industrial aerosol concentrations are passed to the microphysics scheme and affect CDNC, therefore it does not entirely remove the aerosol indirect effect.

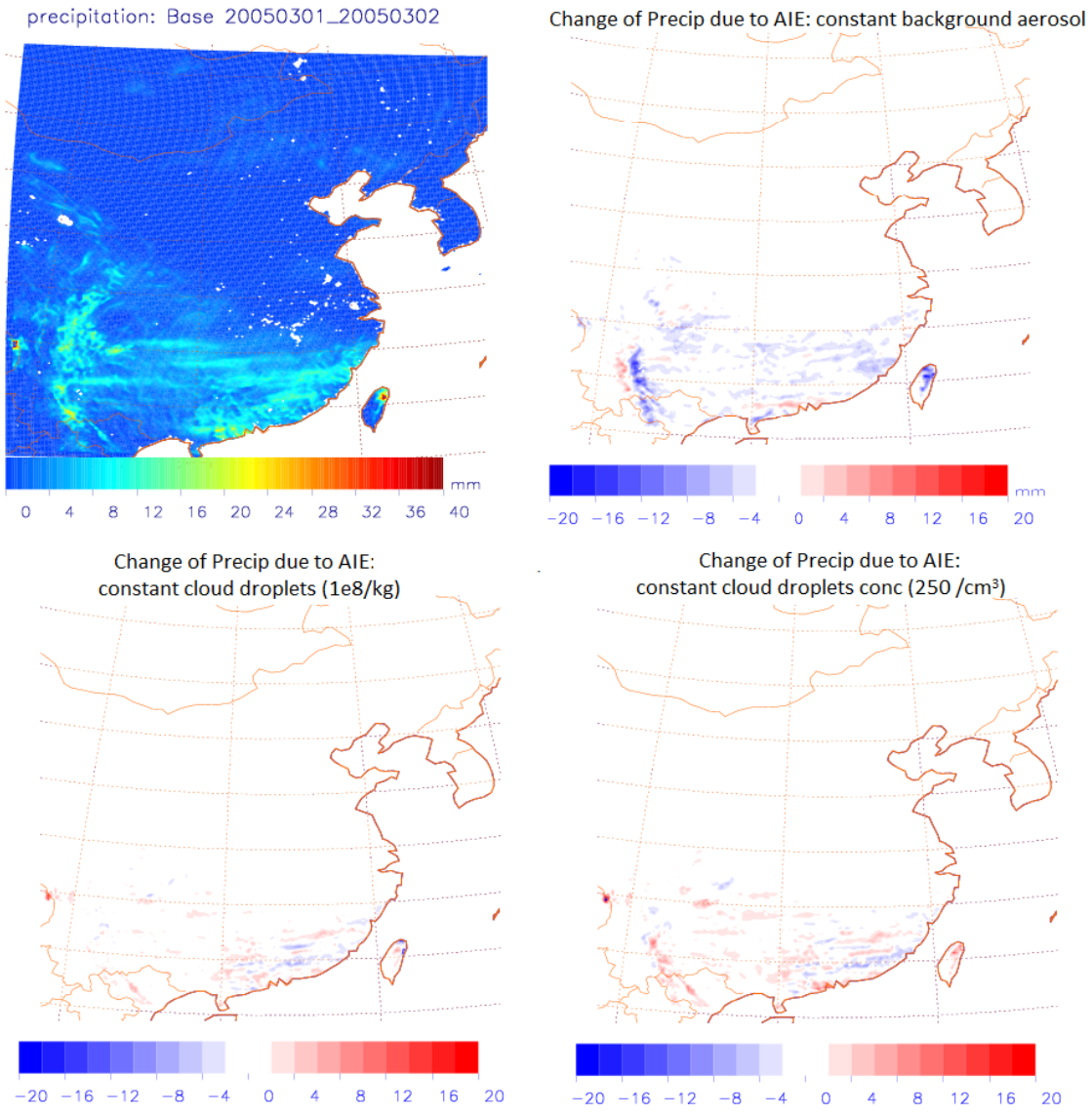

Figure 4.14. Average daily precipitation over March 1st to March 2nd (top left), Change of daily precipitation (base-Test_1) due to the indirect effect (top right), Change of daily precipitation (base-Test_2a) due to the indirect effect (bottom right), and Change of daily precipitation (base-Test_2b) due to the indirect effect (bottom left) from March 1st to March 2nd.

4.4 Discussion and Summary

This study investigated the impact of aerosol direct and indirect effects on meteorological conditions and air quality through analyses of the controlling atmospheric processes during two EAST-AIRE case studies that included significant cloud formation and precipitation. The impact of the ADE and AIE were obtained by subtracting the results of sensitivity simulations that did not include one of these processes from a base simulation that included both of these processes. The sensitivity simulation used to determine the AIE prescribed a constant "pre-industrial" background aerosol concentration in the cloud activation module as opposed to the more commonly used constant cloud droplet concentration in the microphysics scheme. Precipitation rates in southern China decreased due to the AIE. This result differed from *Zhang et al.* [2015] who prescribed cloud droplet concentrations and found that precipitation rates increased over southern China due to the AIE. Two time periods during March 2005 (Case study A and Case study B) with large-scale synoptic cloud and precipitation features but different cloud thicknesses and heights and aerosol loadings were chosen for the analysis. Overall, the impacts of the ADE and AIE on surface radiation, surface temperature and temperature lapse rate are of comparable magnitude, although the direct effect is stronger over highly polluted regions and the indirect effect is stronger over humid regions where thick clouds are formed. Over regions with high aerosol loadings, relatively lower SSA (more absorbing aerosols), and relatively thinner clouds (e.g. Sichuan Basin in Case study B), the warming effect due to reduced SSA (enhanced absorption of radiation)

mitigated the cooling effect associated with the reduction in incoming solar radiation due to the clouds. For regions with high aerosol loading, these competing processes reduced the overall impact of aerosols on meteorological variables with the net sign of the net change varying with meteorological variable and location. For example, changes in surface temperature and lapse rate usually remained negative while changes in surface wind speed and PBL sometimes became positive (e.g., over the Sichuan Basin during case study B). As for atmospheric composition, changes in primary aerosol (i.e., dust, OC) and chemically stable trace gas concentrations (i.e., CO) were mainly driven by the changes of meteorological conditions due to the direct and indirect effects, therefore the direct effect showed a stronger impact over highly polluted and dry regions whereas the indirect effect dominated humid areas. The secondary aerosols (i.e., sulfate, nitrate) and chemically active trace gas (i.e., ozone) are affected by both changes in meteorological and chemical processes. Changes in chemical processes are most important for secondary aerosols in regions with active weather as the microphysical processes associated with the formation of clouds and precipitation in WRF-Chem affects the concentration of aerosols. The variation of ozone due to the indirect effect is associated with changes in the NO_2 photolysis rate that are driven by the actinic flux dominated by either AOD or COD changes. In regions with less active weather, the direct effect is more important.

The version of the Morrison 2-moment microphysics scheme used to simulate the AIE in this study does not include several processes that contribute to the AIE. For example, it does not include interactions between aerosols and ice nuclei, which are important processes in mixed-phase clouds.

As many have shown, aerosols can invigorate mixed-phase clouds. Cloud droplets grow by condensation and coalescence. Condensation is most important for tiny cloud droplets but coalescence soon takes over due to its 5th power dependence on droplet radius [*Freud et al.*, 2011]. The height required for droplets to grow enough for warm rain to begin is proportional to the CDNC [*Freud and Rosenfeld*, 2012]. Therefore the onset of coalescence at polluted locations may be delayed until droplets rise to altitudes where temperatures are sub-freezing. These droplets do not freeze immediately due to their small size but exist as supercooled water delaying the onset of glaciation to greater heights and leading to an increase in cloud top height [*Rosenfeld et al*., 2008]. These smaller droplets rise to higher altitudes leading to a suppression of warm rain and invigoration of deep convection [*Petersen and Rutledge*, 2001; *Khain et al*., 2005; *Koren et al*., 2005; *Lohmann*, 2008; *Koren et al*., 2010]. This invigoration process is evident in observational studies from satellites [*Koren et al.,* 2012; *Lin et al.,* 2006] and in situ measurements [*Li et al.,* 2011b].

Another possible weakness of this study is that it uses a 2-moment bulk microphysics scheme that prescribes the particle size distribution using exponential or gamma distributions as opposed to a spectral bin microphysics (SBM) scheme that would solve for the particle size distribution for each hydrometeor type explicitly [*Khain et al.,* 2015]. The parameterizations used in bulk schemes vary regionally and seasonally and are less sensitive to meteorological conditions and the effect of aerosols. For example, *Fan et al.,* [2012] used a bulk and SBM scheme to study deep convective clouds and stratus clouds over China and found that the bulk microphysical scheme showed similar results to the SBM scheme for stratus clouds

but was less responsive to aerosol-induced changes in the frequency and amount of rain in deep convective clouds.

Chapter 5: Summary and Future work

5.1 Summary of the impact of aerosol direct effect on East Asian air quality

Two WRF-Chem sensitivity simulations with and without aerosol direct effects were performed during EAST-AIRE IOC period (March, 2005) to quantify the impact of aerosol direct effect on surface shortwave radiation and air pollutant levels during this campaign period, and assess the processes that contribute to the changes induced by the direct effect. The simulation including all the aerosol effects was compared with *in-situ* and satellite observations of meteorological conditions, trace gas concentrations, aerosol optical properties and radiation. Comparisons demonstrated the reasonable capability of WRF-Chem in simulating the spatial and temporal variation of meteorological, chemical and radiative components, and their interactions. Analyses performed to interpret the biases between model and the WRF-Chem simulation indicated the low biases in trace gases (CO, SO_2) and AOD for highly polluted days are partly due to the biases in simulated wind fields and emission inventories.

In this study, the impact of the aerosol direct effect was estimated to be -20 W/m^2 domain-wide, and -25 W/m^2 at Xianghe Observatory, comparable with observations. Driven by the change of the incoming radiation, average surface temperature decreased by 0.73˚C over land, the PBL thinned with regional average decreases in height from 75 meters to 138 meters, and the atmosphere became more stable. The surface $PM_{2.5}$ level was enhanced domain wide due to the direct effect, with 4.4 % enhancement in eastern China, 10% in southern China, 2.3% in western China, and

9.6% in the Sichuan Basin, with changes in components varying regionally due to different controlling factors. Increases in primary aerosols were mostly driven by decreases in PBL height and increases in atmospheric stability due to the direct effect. The changes in secondary aerosols were more complex and mainly driven by changes in chemistry resulting from lower OH concentrations due to less photolysis. Sulfate aerosols showed domain-wide decreases due to a reduction in oxidation capacity (less OH) of the atmosphere, while nitrate increased in southern China, western China and the Sichuan Basin but decreased in eastern China, depending on the availability of ammonium aerosols. With less radiation reaching the surface ozone decreased domain-wide, with maximum decreases over the Sichuan Basin.

Since the SO_2 emissions over China are beginning to decline (post 2006) due to the installation of flue gas desulfurization devices in power plants, two additional sensitivity simulations were carried out to test the potential impact of emission reductions on $PM_{2.5}$ and ozone levels. While reducing aerosol emissions reduces $PM_{2.5}$ amounts, our study also indicates that reducing absorbing aerosols could lead to an increase in certain gas pollutants (i.e., ozone) if emissions of NO_x and VOC are unchanged. By contrast, reducing scattering aerosols would reduce both PM and ozone pollution..

5.2 Summary of the relative impact of aerosol direct and indirect effects on East Asian air quality

This study explored the relative importance of the aerosol direct and indirect effects on East Asian air quality. Two time periods (Case study A and Case study B) with

large-scale synoptic cloud and precipitation features during March, 2005 were selected for the analysis since by definition, the aerosol indirect effect alters the atmospheric processes via the impact on the formation of clouds and precipitation. Three WRF-Chem sensitivity simulations were conducted to calculate aerosol direct and indirect effects separately. The impact of the ADE and AIE were obtained by subtracting the results of sensitivity simulations that did not include one of these processes from a base simulation that included both of these processes. We made modifications in the WRF-Chem cloud droplet activation module to use a prescribed constant "pre-industrial" background aerosol concentration, simulating the cloud formation in a "pre-industrial" scenario in the sensitivity simulation without the indirect effect from anthropogenic aerosols. We compared the simulated cloud optical depth and daily precipitation with observations, and found that WRF-Chem yielded fairly good agreement with observations in terms of magnitudes and spatial distributions.

In general, the impacts of the ADE and AIE show comparable magnitude on surface radiation, surface temperature and temperature lapse rate but different influencing regions based on both case studies. The aerosol direct effect dominates over highly polluted regions while the indirect effect is stronger over humid region under synoptic systems. The feedbacks due to the indirect effect are more complex than direct effect since there are competing processes involved. For example, over regions with high aerosol loadings, relatively lower SSA (more absorbing aerosols), and relatively thinner clouds (e.g. Sichuan Basin in Case study B), the warming effect due to reduced SSA (enhanced absorption of radiation) offsets the cooling effect associated

with the reduction in incoming solar radiation due to the clouds. Therefore under such scenario, these competing processes reduced the overall impact of aerosols on meteorological variables with the net sign of the net change varying with meteorological variable and location. For example, changes in surface temperature and lapse rate usually remained negative while changes in surface wind speed and PBL sometimes became positive.

These changes to the meteorological conditions drive the changes in primary aerosols (i.e., OC and dust), and chemically stable trace gas (i.e., CO). The secondary aerosols (i.e., sulfate, nitrate) and chemically active trace gas (i.e., ozone) are affected by both changes in meteorological and chemical processes, which sometimes are competing. Yet changes in chemical processes are most important for secondary aerosols in regions with active weather as the cloud droplet activation processes in WRF-Chem associated with the synoptic system affects the concentration of aerosols.

There are competing factors affecting the variation of surface ozone concentrations due to the indirect effects. The positive factors include meteorological factors like thinner PBL, more stabilized atmosphere, and chemistry factors like smaller AOD, while the negative factors include lower VOC emissions due to cooler temperature and thicker COD. We found the diverse changes of ozone in Case study A and Case study B are mainly due to the changes in the NO_2 photolysis rate that are driven by the actinic flux dominated by either AOD or COD changes.

5.3 Future work in simulating aerosol direct and indirect effects using fully coupled regional model

In Chapter 3 and Chapter 4, we showed and discussed biases and uncertainties in simulated atmospheric processes from WRF-Chem that could contribute to biases in estimates of the impact of aerosol direct and indirect effects on East Asian air quality. Future studies with more accurate input data sets should improve the biases and facilitate the exploration of aerosol direct and indirect effects using regional models.

5.3.1 Improve the representation of wind fields in WRF

As discussed in Chapter 3, overestimation of wind speed contributes to low biases in WRF-Chem trace gas levels and aerosol loading compared to observations at Xianghe Observatory. Sensitivity simulations with different combinations of land surface and boundary layer schemes showed that the high bias in surface wind speed was reduced from 40% with the revised MM5 Monin-Obukhov land surface scheme and the YSU PBL scheme, to 20% with the Quasi–normal Scale Elimination (QNSE) land surface and boundary layer schemes. *Jiménez et al*. [2012] argue that high biases in model wind fields are likely explained by overly smooth topographic features in regional models. They propose to use a new surface sink term in the momentum equation to account for the effects of unresolved topography on the atmospheric circulation. This proposed scheme reduced the mean absolute error of the mean wind speed in their study domain (Comunidad Foral de Navarra, a complex-terrain region that is located in the northeast of the Iberian Peninsula) from 1.85 to 0.72 m s^{-1}. The topographic features are also quite complex over East Asia, therefore adapting their approach to

Eastern Asia should improve the wind field simulation.

5.3.2 Include comprehensive Secondary Organic Aerosol (SOA) scheme

Fast et al. [2006] argue that lack of a SOA scheme in WRF-Chem contributes to a low bias in simulated AOD in their work. The version of WRF-Chem used in this study (v3.3) also lacks a comprehensive SOA scheme. While we argue that SOA formation is not critical during our study time period, other studies have shown the importance of SOA in China especially for hazy winter events or summertime periods with high biogenic VOC emissions, therefore including SOA formation is necessary for expanding this study to other time periods. Fortunately, SOA formation is implemented in WRF-Chem beginning with v3.4. A volatility basis set (VBS) treatment is used to simulate gas-particle partitioning and gas-phase oxidation of organic vapors for 9 species with effective saturation concentrations (C*) ranging from 10^{-2} to 10^{6} μg m^{-3} at 298 K and 1 atm [*Shrivastava et al*., 2011]. The VBS treatment of SOA formation is coupled with the gas phase chemistry and aerosol modules via KPP (Kinetic PreProcessor), and is currently being tested for different combinations of chemistry and aerosol modules.

5.3.3 Improve parameterizations of aerosol optical properties

Simulated aerosol scattering coefficients from WRF-Chem show low biases compared to observations, contributing to the low biases of AOD. Biases in scattering coefficients have potential impact on the diffuse radiation and therefore the photolysis rates of important atmospheric constituents (i.e., NO_2). Low bias of scattering coefficient may come from the lack of the aging process of black carbon

(BC). As discussed in Chapter 2, section 2.1.2.1.3, BC becomes less absorbing and more scattering when gets further away from emission sources. Taking the BC aging process into account may improve the bias in scattering coefficient.

5.3.4 Expand current study to other time periods

We conducted this work for the EAST-AIRE IOC period, which occurred in early springtime of 2005. There are limitations for investigating impact of aerosols in meteorology and chemistry during this time period. First of all, biogenic VOC emissions are minor for most parts of East Asia during this season, so that SOA levels are low, making it difficult to assess the contributions of SOA to the aerosol-radiation-meteorology-chemistry feedbacks. Secondly, even though we explored the impact of aerosol effects on other air pollutants such as ozone, pollution due to ozone is less severe in early springtime than in summer. Last but not least, pollution due to $PM_{2.5}$ in China may become extremely severe during wintertime in eastern and northern China. Based on our current study, aerosol effects may have positive feedbacks with increased aerosol loadings, which exacerbate the pollution issue. Therefore, expanding our current study to other time periods is would be meaningful.

5.3.5 Expand current study to study impact of aerosols on aloft pollution

Our current study focused on the impact of aerosol effects on air pollutants at the surface but we have seen the significant impact of aerosols (i.e., AOD) on aloft pollution too. In-depth investigations of the feedback processes at higher altitudes would be useful to gain insight into the impact of aerosols on free troposphere chemistry, atmospheric circulation, and pollutant transport. Vertical analyses require

detailed evaluations of the modeled trace gases, aerosols and meteorological/dynamic variables with observations under different conditions (i.e., cloudy vs. cloud-free, hazy vs. clear). Aircraft observations, such as the aircraft campaign for EAST-AIRE in Liaoning Province during early April, 2005 [*Dickerson et al.,* 2007] and ARIAs campaign in 2016 [Li and Dickerson from AOSC/UMD], would provide precious data at higher altitudes to improve our understanding of these relationships.

Appendix

The photolysis rate of trace gas *j* (J-value) is calculated by:

$$J(i) = \int_{\lambda 1}^{\lambda 2} \sigma i(\lambda, T)\, \phi i\,(\lambda, T) F(\lambda) d\lambda \qquad \text{eq.(1),}$$

where $\sigma_i(\lambda,T)$ (in the unit of cm^2) is the wavelength and temperature-dependent absorption cross-section of species i, $\phi_i(\lambda,T)$ is the quantum yield, and $F(\lambda)$ (in the unit of photons cm^{-2} nm^{-1} s^{-1}) is the solar actinic flux. In our work, the FAST-J photolysis algorithm [*Wild et al.*, 2000] is applied to compute the actinic flux. Determination of actinic flux at each vertical layer depends on the attenuation of incoming solar radiation, therefore optical properties for scattering and absorption by molecules, aerosols, and cloud droplets throughout the vertical extent need to be specified. In FAST-J, these optical properties are expressed as the optical thickness, τ; the single scattering albedo, ω_0; and the scattering phase function, $p(\theta)$ as a function of wavelength λ. The optical thickness (τ) is the sum of molecular (Rayleigh) scattering, gaseous absorption by ozone, aerosol extinction, and cloud optical thickness. Rayleigh scattering is solely dependent on the pressure, therefore easily determined. Absorption by ozone is given by the prognostic ozone profile from WRF-Chem. Cloud optical depths are treated by using fractional cloudiness based on relative humidity in the photolysis module in WRF-Chem. The default version of WRF-Chem uses a lookup table with prescribed aerosol optical properties to calculate the actinic flux; therefore, the model aerosols have no impact on the photolysis rates. We have implemented a link between prognostic aerosol

concentrations and the Fast-J module. The aerosol mass concentrations in each of the 8 bins are passed to a subroutine inside module_optical_averaging.F to calculate aerosol number density in each bin, effective radius, and refractive index. Then this information is used in a module (mieaer) based on Mie theory to calculate the prognostic aerosol size distribution, extinction coefficient, single scattering albedo, asymmetry parameter, and aerosol optical depth, which are applied in the calculation of actinic flux in Fast-J module.

In order to test our implementation of the aerosol photolysis link, we performed one-day sensitivity simulations to test the impact of the prognostic sulfate and black carbon on the photolysis rate in WRF-Chem assuming cloud-free conditions. We selected one simulation day (March 15th, 2005), and performed three sensitivity simulations: 1) no aerosol in Fast-J module; 2) only sulfate in Fast-J module; 3) only black carbon in Fast-J module. We examined the impact of sulfate and black carbon on the NO_2 photolysis rate at Xianghe station at 12UTC. The total burden of sulfate and black carbon are assumed to be 110 mg/m^2 and 25 mg/m^2, respectively. About 90% of black carbon is concentrated below 300 meters, decreasing rapidly with height. Sulfate is abundant near the surface and around 500 meters due to SO_2 emissions from both industrial/residential sources at surface and power plant emissions aloft. The absorbing aerosol black carbon reduces the NO_2 photolysis rate at all the vertical layers with the largest reduction near the surface (Figure A1 left, middle). On the other hand, the scattering aerosol sulfate decreases the NO_2 photolysis rate near surface but increases it at higher layers (Figure A1 left, right), because sulfate is mostly backscattering, blocking the radiation below the sulfate

aerosol layer, but enhancing the radiation at upper levels by scattering the radiation back.

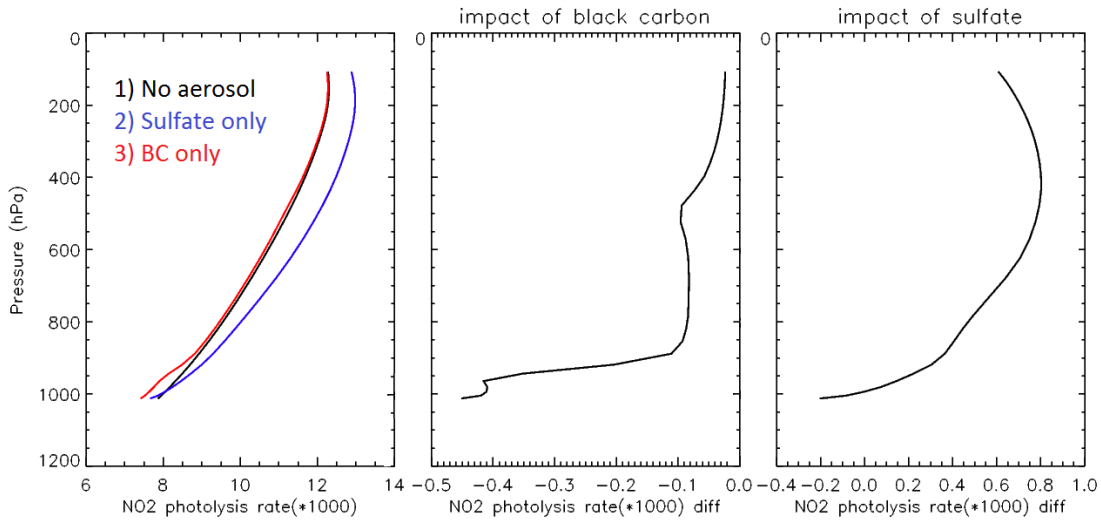

Figure A1 Left: NO_2 photolysis rate (s^{-1}) from three simulations: No aerosol in Fast-J module (black), sulfate only (blue) and BC only (red). Middle: impact of black carbon on NO_2 photolysis rate (s^{-1}). Right: impact of sulfate on NO_2 photolysis rate (s^{-1}).

The results are consistent with a previous study by *Liao et al.,* [1999]. They used the one-dimensional discrete ordinate radiative transfer (DISORT) model [*Stamnes et al*., 1988] to investigate the effects of $(NH_4)_2SO_4$ and soot on the $j(O_3 \rightarrow O^1D)$, $j(NO_2)$ and j(HCHO) profile under clear sky and cloudy sky conditions. They assumed column burdens of 125 mg m^{-2} for $(NH_4)_2SO_4$ and 25 mg m^{-2} for soot under polluted urban conditions, with the mass concentration of each species decreasing linearly from its value at the surface to 0.1 of its surface value at 3-km altitude and remaining constant from 3 to 5 km. They also found that in the clear sky condition, soot aerosol reduces photolysis rates at all altitudes, whereas sulfate aerosol generally increases

photolysis rates above and in the upper part of the aerosol layer but reduces photolysis rates in the lower part of the aerosol layer and at the surface (Figure 3 and Figure 4 from *Liao et al.,* [1999]).

Bibliography

Abel, S.J., et al. (2003), Evolution of biomass burning aerosol properties from an agricultural fire in southern Africa. *Geophys. Res. Lett*., 30(15), 1783, doi:10.1029/2003GL017342.

Albrecht, B. (1989), Aerosols, cloud microphysics and fractional cloudiness. *Science*, 245, 1227–1230.

Barnard, J. C, E. G. Chapman, J. D. Fast, J. R. Schmelzer, J. R. Schlusser, and R. E. Shetter (2004), An evaluation of the FAST-J photolysis model for predicting nitrogen dioxide photolysis rates under clear and cloudy sky conditions, *Atmos Environ.*, 38, 3393-3403.

Binkowski, F. S., and U. Shankar (1995), The Regional Particulate Matter Model: 1. Model description and preliminary results, *J. Geophys. Res.,* 100, 26,191– 26,209.

Boersma, K.F., H.J. Eskes, R. J. Dirksen, R. J. van der A, J. P. Veefkind, P. Stammes, V. Huijnen, Q. L. Kleipool, M. Sneep, J. Claas, J. Leitão, A. Richter, Y. Zhou, and D. Brunner (2011), An improved tropospheric NO2 column retrieval algorithm for the Ozone Monitoring Instrument, *Atmos. Meas. Tech.,* 4, 1905-1928.

Bond, T.C., et al., (1999), Light absorption by primary particle emissions from a lignite burning plant. *Environ. Sci.Technol.*, 33, 3887–3891.

Bond, T.C., 2001: Spectral dependence of visible light absorption by carbonaceous particles emitted from coal combustion. *Geophys. Res. Lett.*, 28(21), 4075–4078.

Brauer, M. et al. (2015), Ambient Air Pollution Exposure Estimation for the Global Burden of Disease 2013, *Environ. Sci. Technol.*, 50 (1), 79–88, DOI: 10.1021/acs.est.5b03709.

Chang, R. Y.-W. , J. G. Slowik, N. C. Shantz, A. Vlasenko, J. Liggio, S. J. Sjostedt, W. R. Leaitch, and J. P. D. Abbatt (2010), The hygroscopicity parameter (κ) of ambient organic aerosol at a field site subject to biogenic and anthropogenic influences: relationship to degree of aerosol oxidation, *Atmos. Chem. Phys.,* 10, 5047–5064.

Chapman, E. G., W. I. Gustafson Jr., R. C. Easter, J. C. Barnard, S. J. Ghan, M. S. Pekour and J. D. Fast (2009), Coupling aerosol-cloud-radiative processes in the WRF-Chem model: Investigating the radiative impact of elevated point sources, *Atmos. Chem. Phys.,* 9, 945–964, doi:10.5194/acp-9-945-2009.

Che, X., X. Xia, J. Zhu, H. Wang, Y. Wang, J. Sun, X. Zhang, G. Shi (2015), Aerosol optical properties under the condition of heavy haze over an urban site of Beijing, China, Environ Sci Pollut Res Int., 22(2), 1043-53. doi: 10.1007/s11356-014-3415-5.

Chen, F., and J. Dudhia (2001), Coupling an advanced land-surface/hydrology model with the Penn State/NCAR MM5 modeling system. Part I: Model description and implementation. *Mon. Wea. Rev.,* 129, 569–585.

Chou M.-D., and M. J. Suarez (1994), An efficient thermal infrared radiation parameterization for use in general circulation models, *NASA Tech. Memo*. 104606, 3, 85 pp.

Claquin, T., M. Schulz, and Y. Balkanski, 1999: Modeling the mineralogy of atmospheric dust. *J. Geophys. Res.*, 104(D18), 22243–22256.

Collins, W. D., Conant, W. C., and Ramanathan, V. (1994), Earth radia- tion budget, clouds, and climate sensitivity, in: The Chemistry of the Atmosphere: Its Impact on Global Change, edited by: J. G. Calvert, pp. 207–215, Blackwell Scientific Publishers, Oxford, UK.

Dickerson, R. R., S. Kondragunta, G. Stenchikov, K. L. Civerolo, B. G. Doddridge, and B. N. Holben (1997), The impact of aerosols on solar ultraviolet radiation and photochemical smog, *Science*, 278 (5339), 827-830, DOI: 10.1126/science.278.5339.827.

Dickerson, R. R., et al. (2007), Aircraft observations of dust and pollutants over northeast China: Insight into the meteorological mechanisms of transport, *J. Geophys. Res.,* 112, D24S90, doi:10.1029/2007JD008999.

Dockery, D. W., C. A. Pope, X. Xu, J. D. Spengler, J. H. Ware, M. E. Fay, B. G. Ferris, Jr., and F, E. Speizer (1993), An Association between Air Pollution and Mortality in Six U.S. Cities, N. Engl. J. Med., 329, 1753-1759.

Dubovik, O., et al., 2002: Variability of absorption and optical properties of key aerosol types observed in worldwide locations. *J. Atmos. Sci*., 59, 590–608.

Duplissy, J., P. F. DeCarlo, J. Dommen, M. R. Alfarra, A. Metzger, I. Barmpadimos, A. S. H. Prevot, E. Weingartner, T. Tritscher, M. Gysel, A. C. Aiken, J. L. Jimenez, M. R. Canagaratna, D. R. Worsnop, D. R. Collins, J. Tomlinson, and U. Baltensperger (2011), Relating hygroscopicity and composition of organic aerosol particulate matter, *Atmos. Chem. Phys.,* 11, 1155–1165.

Dusek, U., et al. (2006), Size matters more than chemistry for cloud-nucleating ability of aerosol particles. *Science*, **312**, 1375–1378.

Emmons, L. K., Walters, S., Hess, P. G., Lamarque, J.-F., Pfister, G. G., Fillmore, D., Granier, C., Guenther, A., Kinnison, D., Laepple, T., Orlando, J., Tie, X., Tyndall, G., Wiedinmyer, C., Baughcum, S. L., and Kloster, S. (2010), Description and evaluation of the Model for Ozone and Related chemical Tracers, version 4 (MOZART-4), *Geosci. Model Dev*., 3, 43-67, doi:10.5194/gmd-3-43-2010.

Eriksen, T. E. (1972), Sulfur Isotope Effects 1. Isotopic Exchange Coefficient for Sulfur Isotopes 34S-32S in System SO2(g)-HSO3(aq) at 25, 35, and 45 Degrees C, *Acta Chem. Scand.*, 26, 573.

Ervens, B., et al. (2007), Prediction of cloud condensation nucleus number concentration using measurements of aerosol size distributions and composition and light scattering enhancement due to humidity. *J. Geophys. Res.*, **112**, D10S32.

Fan, J., L. R. Leung, Z. Li, H. Morrison, H. Chen, Y. Zhou, Y. Qian, and Y. Wang (2012), Aerosol impacts on clouds and precipitation in eastern China: Results from bin and bulk microphysics, *J. Geophys. Res.,* 117, D00K36, doi:10.1029/2011JD016537.

Fast, J. D., W. I. Gustafson Jr., R. C. Easter, R. A. Zaveri, J. C. Barnard, E. G. Chapman, G. A. Grell, and S. E. Peckham (2006), Evolution of ozone, particulates, and aerosol direct radiative forcing in the vicinity of Houston using a fully coupled meteorology-chemistry-aerosol model, *J. Geophys. Res.*, 111, D21305, doi:10.1029/2005JD006721.

Forkel, R., J. Werhahn, A. B. Hansen, S. McKeen, S. Peckham, G. Grell, P. Suppan (2012), Effect of aerosol-radiation feedback on regional air quality: A case study with WRF/Chem, *Atmospheric Environment*, 53, 202-211.

Freud, E., D. Rosenfeld, K. R. Kulkarni (2011), Resolving both entrainment-mixing and number of activated CCN in deep convective clouds, *Atmos. Chem. Phys.,* 11, 12887–12900.

Freud, E., and D. Rosenfeld (2012), Linear relation between convective cloud drop number concentration and depth for rain initiation, *J. Geophys. Res.,* 117, D02207, doi:10.1029/2011JD016457.

Fuglestvedt, J. S., J. E. Jonson, and I. S. A. Isaksen (1994), Effects of reductions in stratospheric ozone on tropospheric chemistry through changes in photolysis rates, *Tellus, Ser. B*, 46, 172-192.

Gao, W., J. Fan, R. C. Easter, Q. Yang, C. Zhao, and S. J. Ghan (2016), Coupling spectral-bin cloud microphysics with the MOSAIC aerosol model in WRF-Chem: Methodology and results for marine stratocumulus clouds, J. Adv. Model. Earth Syst., 8, 1289–1309, doi:10.1002/2016MS000676.

Ghan, S. J (2013), Technical Note: Estimating aerosol effects on cloud radiative forcing, Atmos. Chem. Phys., 13, 9971-9974, doi:10.5194/acp-13-9971-2013.

Grell, G. A (1993), Prognostic Evaluation of Assumptions Used by Cumulus Parameterizations, *Mon. Wea. Rev.*, 121, 764–787.

Grell, G. A., and D. Devenyi (2002), A generalized approach to parameterizing convection combining ensemble and data assimilation techniques, *Geophys. Res. Lett*., 29, 38:1–38:4.

Grell, G. A., S. E. Peckham, R. Schmitz, S. A. McKeen, G. Frost, W. C. Skamarock, and B. Eder (2005), Fully coupled ‘‘online’’ chemistry within the WRF model, *Atmos. Environ.*, 39, 6957– 6975.

Guenther, A., C. N. Hewitt, D. Erickson, R. Fall, C. Geron, T. Graedel, P. Harley, L. Klinger, M. Lerdau, W. A. Mckay, T. Pierce, B. Scholes, R. Steinbrecher, R. Tallamraju, J. Taylor, and P. A. Zimmerman (1995), Global-Model of Natural Volatile Organic-Compound Emissions, *J. Geophys. Res.- Atmos*., 100(D5), 8873–8892.

Guenther, A., T. Karl, P. Harley, C. Wiedinmyer, P. I. Palmer, and C. Geron (2006), Estimates of global terrestrial isoprene emissions using MEGAN (Model of Emissions of Gasses and Aerosols from Nature), *Atmos. Chem. Phys*., 6, 3181-3210.

Gunthe, S. S., S. M. King, D. Rose, Q. Chen, P. Roldin, D. K. Farmer, J. L. Jimenez, P. Artaxo, M. O. Andreae, S. T. Martin, and U. Po¨schl (2009), Cloud condensation nuclei in pristine tropical rainforest air of Amazonia_size-resolved measurements and modeling of atmospheric aerosol composition and CCN activity, Atmos. Chem. Phys., 9, 7551–7575, doi:10.5194/acp-9-7551-2009.

Hand, J. L., B. A. Schichtel, W. C. Malm, and M. L. Pitchford (2012), Particulate sulfate ion concentration and SO2 emission trends in the United States from the early 1990s through 2010, Atmos. Chem. Phys., 12, 10353–10365, doi:10.5194/acp-12-10353-2012 .

Hansen, J., M. Sato, and R. Ruedy (1997), Radiative forcing and climate response. J. Geophys. Res., 102(D6), 6831–6864.

Harris, E., B. Sinha, P. Hoppe, J. N. Crowley, S. Ono, and S. Foley (2012), Sulfur isotope fractionation during oxidation of sulfur dioxide: gas-phase oxidation by OH radicals and aqueous oxidation by H_2O_2, O_3 and iron catalysis, Atmos. Chem. and Phys., 12, 407-424.

Harrison, R. M. and J. Yin (2000), Particulate matter in the atmosphere: which particle properties are important for its effects on health? Sci. Total. Environ., 249(1-3), 85-101.

Haywood, J.M., and O. Boucher (2000), Estimates of the direct and indirect radiative forcing due to tropospheric aerosols: A review. *Rev. Geophys.*, 38, 513–543.

Haywood, J.M., et al. (2003), The mean physical and optical properties of regional haze dominated by biomass burning aerosol measured from the C-130 aircraft during SAFARI 2000. *J. Geophys. Res*., 108(D13), 8473, doi:10.1029/2002JD002226.

He, S., and G. R. Carmichael (1999), Sensitivity of photolysis rates and ozone production in the troposphere to aerosol properties, J. Geophys. Res., 104(D21), 26307–26324, doi:10.1029/1999JD900789.

Hinds, W. C. (1999), Aerosol technology: Properties, behavior, and measurement of airborne particles. New York: Wiley.

Holben, B. N., et al. (1998), AERONET—A federated instrument network and data archive for aerosol characterization, *Remote Sens. Environ.*, 66, 1–16, doi:10.1016/S0034-4257(98)00031-5.

Hong, S., Y Noh and J. Dudhia (2006), A new vertical diffusion package with an explicit treatment of entrainment processes, *Mon. Weather Rev.*, 134, 2318-2341.

Hoose, C., and O. Möhler (2012), Heterogeneous ice nucleation on atmospheric aerosols: A review of results from laboratory experiments. *Atmos. Chem. Phys.*, **12**, 9817–9854.

Hsu, N. C., R. Gautam, A. M. Sayer, C. Bettenhausen, C. Li, M. J. Jeong, S. –C. Tsay, and B. N. Holben (2012), Global and regional trends of aerosol optical depth over land and ocean using SeaWiFS measurements from 1997 to 2010, *Atmos. Chem. Phys.,* 12, 8037-8053.

Huang, K., G. Zhang, Q. Wang, J. S. Fu, Y. Lin, T. Liu, L. Han, and C. Deng (2014), Extreme haze pollution in Beijing during January 2013: chemical characteristics, formation mechanism and role of for processing, *Atmos. Chem, Phys. Discuss.,* 14, 7517-7556.

Huang et al. (2014), High secondary aerosol contribution to particulate pollution during haze events in China, *Nature*, 514, 218-222.

Huang, X., Y. Song, M. Li, J. Li, Q. Huo, X. Cai, T. Zhu, M. Hu, and H. Zhang (2012), A high-resolution ammonia emission inventory in China, *Global Biogeochem. Cycles*, 26, GB1030, doi:10.1029/2011GB004161.

IPCC(2001), *Climate Change 2001: The Scientific Basis. Contribution of Working Group I to the Third Assessment Report of the Intergovernmental Panel on Climate Change* [Houghton, J.T., et al. (eds.)]. Cambridge University Press, Cambridge, United Kingdom and New York, NY, USA, 881 pp.

IPCC (2007), Climate Change 2007: The Physical Science Basis. *Contribution of Working Group I to the Fourth Assessment Report of the Intergovernmental Panel on Climate Change* [Solomon, S., D. Qin, M. Manning, Z. Chen, M. Marquis, K.B. Averyt, M.Tignor and H.L. Miller (eds.)]. Cambridge University Press, Cambridge, United Kingdom and New York, NY, USA.

IPCC (2014), Climate Change 2014: Synthesis Report. Contribution of Working Groups I, II and III to the Fifth Assessment Report of the Intergovernmental Panel on Climate Change [Core Writing Team, R.K. Pachauri and L.A. Meyer (eds.)]. IPCC, Geneva, Switzerland, 151 pp.

Jacobson, M.Z. (1999), Isolating nitrated and aromatic aerosols and nitrated aromatic gases as sources of ultraviolet light absorption. *J. Geophys. Res*., 104(D3), 3527–3542.

Jiang, F., Q. Liu, X. Huang, T. Wang, B. Zhuang, and M. Xie (2012), Regional modeling of secondary organic aerosol over China using WRF/Chem, *Journal of Aerosol Science*, 43(1), 57-73.

Jiménez, P. and Dudhia, J. (2012), Improving the Representation of Resolved and Unresolved Topographic Effects on Surface Wind in the WRF Model, *Journal of Applied Meteorology and Climatology*, 51(2), DOI: 10.1175/JAMC-D-11-084.1

Khain, A., D. Rosenfeld, and A. Pokrovsky (2005), Aerosol impact on the dynamics and microphysics of deep convective clouds. *Q. J. R. Meteorol. Soc.,* **131**, 2639–2663.

Khain, A. P., Beheng, K. D., Heymsfield, A., Korolev, A., Krichak, S. O., Levin, Z., Pinsky, M., Phillips, V., Prabhakaran, T., Teller, A., van den Heever, S. C., and Yano, J.-I.: Representation of microphysical processes in cloud-resolving models: spectral (bin) microphysics vs. bulk parameterization (2015), *Rev. Geophys.,* 53, 247– 322.

Khairoutdinov, M. F. and Yang, C.-E. (2013), Cloud-resolving modelling of aerosol indirect effects in idealised radiative-convective equilibrium with interactive and fixed sea surface temperature, *Atmos. Chem. Phys.,* 13, 4133–4144.

Koren, I., Y. J. Kaufman, D. Rosenfeld, L. A. Remer, and Y. Rudich (2005), Aerosol invigoration and restructuring of Atlantic convective clouds. *Geophys. Res. Lett.*, **32**, L14828.

Koren, I., G. Feingold, and L. A. Remer (2010), The invigoration of deep convective clouds over the Atlantic: Aerosol effect, meteorology or retrieval artifact? *Atmos. Chem. Phys.*, **10**, 8855–8872.

Koren, I., O. Altaratz, L. A. Remer, G. Feingold, J. V. Martins, and R. H. Heiblum (2012), Aerosol-induced intensification of rain from the tropics to the mid-latitudes, *Nat. Geosci.,* 5, 118–122, doi:10.1038/NGEO1364.

Koop, T. (2004), Homogeneous Ice Nucleation in Water and Aqueous Solutions, *Zeitschrift für Physikalische Chemie*. Volume 218, Issue 11/2004, Pages 1231–1258, DOI: https://doi.org/10.1524/zpch.218.11.1231.50812, September 2009.

Lee, K. H., Z. Li, M. S. Wong, J. Xin, Y. Wang, W.-M. Hao, and F. Zhao (2007), Aerosol single scattering albedo estimated across China from a combination of ground and satellite measurements, J. Geophys. Res., 112, D22S15, doi:10.1029/2007JD009077.

Levelt, P. F., G. H. J. van den Oord, M. R. Dobber, A. Malkki, H. Visser, J. de Vries, P. Stammes, J. O. V. Lundell, and H. Saari (2006), The Ozone Monitoring Instrument, *IEEE Trans. Geosci. Remote Sens.*,44, 1093–1101, doi:10.1109/TGRS.2006.872333.

Li, C., L.T. Marufu, R. R. Dickerson, Z. Li, T. Wen, Y. Wang, P. Wang, H. Chen, and J. W. Stehr (2007), In situ measurements of trace gases and aerosol optical properties at a rural site in northern China during East Asian Study of Tropospheric Aerosols: An International Regional Experiment 2005, *J. Geophys. Res.*, D22S04, doi:10.1029/2006JD007592.

Li, C., Q. Zhang, N. A. Krotkov, D. G. Street, K. He, S. Tsay, and J. F. Gleason (2010), Recent large reduction in sulfur dioxide emissions from Chinese power plants observed by the Ozone Monitoring Instrument, Geophys. Res. Lett., 37, L08807, doi: 10.1029/2010GL042594.

Li, Z., et al. (2007a), Aerosol optical properties and their radiative effects in northern China, *J. Geophys. Res.*, 112, D22S01, doi:10.1029/ 2006JD007382.

Li, Z., et al. (2007b), Preface to special section on East Asian Studies of Tropospheric Aerosols: An International Regional Experiment (EASTAIRE), *J. Geophys. Res.*, 112, D22S00, doi:10.1029/2007JD008853.

Li, Z., Z. Yan (2009) Homogenized daily mean/maximum/minimum temperature series for China from 1960-2008. *Atmos Oceanic Sci Lett* 2(4):237–243.

Li, Z., K.-H. Lee, J. Xin, Y. Wang, and W.-M. Hao (2010), First observation-based estimates of cloud-free aerosol radiative forcing across China, *J. Geophys. Res.*, 115, D00K18, doi:10.1029/2009JD013306.

Li, Z., et al. (2011a), East Asian Studies of Tropospheric Aerosols and their Impact on Regional Climate (EASTAIRC): An overview, *J. Geophys. Res.*, 116, D00K34, doi:10.1029/2010JD015257.

Li, Z., F. Niu, J. Fan, Y. Liu, D. Rosenfeld, and Y. Ding (2011b), Long-term impacts of aerosols on the vertical development of clouds and precipitation, *Nature Geosci.*, **4**, 888–894.

Liao, H., Y. L. Yung, and J. H. Seinfeld (1999), Effects of aerosol on tropospheric photolysis rates in clear and cloudy atmospheres, *J. Geophys. Res.*, 104(D19), 23697-23707.

Lin, J. C., T. Matsui, R. A. Pielke Sr., and C. Kummerow (2006), Effects of biomass-burning-derived aerosols on precipitation and clouds in the Amazon Basin: a satellite-based empirical study, J. Geophys. Res., 111, D19204, doi:10.1029/2005JD006884.

Liu, H., et al. (2006), Radiative effect of clouds on tropospheric chemistry in a global three-dimensional chemical transport model, *J. Geophys. Res.,* 111, D20303, doi:10.1029/2005JD006403.

Liu, S.C., and M. Trainer (1988), Responses of the tropospheric ozone and odd hydrogen radicals to column ozone change, *J. Atmos. Chem*., 6, 221-233.

Lohmann, U., and J. Feichter (2005), Global indirect aerosol effects: A review. *Atmos. Chem. Phys.*, 5, 715–737.

Lohmann, U., 2008: Global anthropogenic aerosol effects on convective clouds in ECHAM5–HAM. *Atmos. Chem. Phys.*, **8**, 2115–2131.

Lu, Z., D. G. Streets, Q. Zhang, S. Wang, G. R. Carmichael, Y. F. Cheng, C. Wei, M. Chin, T. Diehl, and Q. Tan (2010), Sulfur dioxide emissions in China and sulfur trends in East Asia since 2000, Atmos. Chem. Phys., 10, 6311–6331.

Ma. J., Effects of stratospheric ozone depletion on tropospheric chemistry through changes in UV-B radiation (1995), *Neth. Organ for Appl. Sci*., Delft, Netherland, TNO-MW-R-95/127.

Madronich, S., and C. Granier, Impact of recent total ozone changes on tropospheric ozone photodissociation, hydroxyl radicals, and methane trends (1992), *Geophys. Res. Lett.,* 19, 465-467.

Makar, P., W. Gong, J. Milbrandt, C. Hogrefe, Y. Zhang, G. Curci, R. Žabkar, U. Im, A. Balzarini, and R. Baró (2015a), Feedbacks between air pollution and weather, part 1: effects on weather, Atmospheric Environment, 115, 442-469.

Makar, P. A., W. GonG, C. Hogrefe, Y. Zhang, G. Curci, R. Žabkar, J. Milbrandt, U. Im, A. Balzarini, R. Baró, R. Bianconi, P. Cheung, R. Forkel, S. Gravel, M. Hirtl, L. Honzak, A. Hou, P. Jiménez-Guerrero, M. Langer, M.D. Moran, B. Pabla, J.L. Pérez, G. Pirovano, R. San José, P. Tuccella, J. Werhahn, J. Zhang and S. Galmarini (2015b), Feedbacks between air pollution and weather, part 2: Effects on chemistry , *Atmos. Eviron.,* 115, 499-526.

McFiggans, G., et al. (2006), The effect of aerosol composition and properties on warm cloud droplet activation. *Atmos. Chem. Phys*., 6, 226 2593–2649.

Mikami, M., et al. (2006), Aeolian dust experiment on climate impact: an overview of Japan-China Joint Project ADEC. *Global Planet. Change*, 52, 142–172, doi:10.1016/j.gloplacha.2006.03.001.

Mlawer, E.J., S.J. Taubman, P.D. Brown, M.J. Iacono and S.A. Cloug (1997), RRTM, a validated correlated-k model for the longwave. *J. Geophys. Res.*, 102, 16,663-16,682.

Morrison, H., J. A. Curry, and V. I. Khvorostyanov (2005), A new double-moment microphysics parameterization for application in cloud and climate models, Part I: Description, *J. Atmos. Sci.,* 62, 1665– 1677.

Morrison, H., G. Thompson, and V. Tatarskii (2009), Impact of Cloud Microphysics on the Development of Trailing Stratiform Precipitation in a Simulated Squall Line: Comparison of One- and Two-Moment Schemes, *Mon. Weather Rev.*, 137, 991–1007, doi:10.1175/2008mwr2556.1.

Mu, M., J.T. Randerson, G.R. van der Werf, L. Giglio, P. Kasibhatla, D. Morton, G.J. Collatz, R.S. DeFries, E.J. Hyer, E.M. Prins, D.W.T. Griffith, D. Wunch, G.C. Toon, V. Sherlock, and P.O. Wennberg (2010), Daily and 3-hourly variability in global fire emissions and consequences for atmospheric model predictions of carbon monoxide, *Journal of Geophysical Research-Atmospheres*,116: D24303. doi:10.1029/2011JD016245.

Myhre, G., Stordal, F., Restad, K. and Isaksen, I. S. A. (1998), Estimation of the direct radiative forcing due to sulfate and soot aerosols. *Tellus B*, 50: 463–477. doi:10.1034/j.1600-0889.1998.t01-4-00005.x.

Penner, J.E., et al. (2001), Aerosols, their direct and indirect effects. In: *Climate Change 2001: The Scientific Basis. Contribution of Working Group I to the Third Assessment Report of the Intergovernmental Panel on Climate Change* [Houghton, J.T., et al. (eds.)]. Cambridge University Press, Cambridge, United Kingdom and New York, NY, USA, pp. 289– 348.

Petersen, W. A., and S. A. Rutledge (2001), Regional variability in tropical convection: Observations from TRMM. *J. Climate,* **14,** 3566–3586.

Petters, M. D., and S. M. Kreidenweis (2007), A single parameter representation of hygroscopic growth and cloud condensation nucleus activity. *Atmos. Chem. Phys.*, **7**, 1961–1971.

Pincus, R. and M. Baker (1994), Effect of precipitation on the albedo susceptibility of clouds in the marine boundary layer, *Nature*, 372, 250 – 252, doi:10.1038/372250a0.

Pöschl, U., D. Rose, and M. O. Andreae (2009), Climatologies of Cloud-related Aerosols. Part 2: Particle Hygroscopicity and Cloud Condensation Nucleus Activity. In J. Heintzenberg, & R. J. Charlson (Eds.), *Clouds in the Perturbed Climate System: Their Relationship to Energy Balance, Atmospheric Dynamics, and Precipitation* (pp. 58-72). Cambridge: MIT Press.

Pringle, K. J., Tost, H., Pozzer, A., Pöschl, U., and Lelieveld, J. (2010), Global distribution of the effective aerosol hygroscopicity parameter for CCN activation, *Atmos. Chem. Phys.,* 10, 5241-5255, doi:10.5194/acp-10-5241-2010.

Qiu, J., L. Yang, L. and X. ZHANG (2004), Characteristics of the imaginary part and single-scattering albedo of urban aerosols in northern China. *Tellus B*, 56: 276–284. doi:10.1111/j.1600-0889.2004.00101.x.

Ramaswamy, V., et al., 2001: Radiative forcing of climate change. In: *Climate Change 2001: The Scientifi c Basis. Contribution of Working Group I to the Third Assessment Report of the Intergovernmental Panel on Climate Change* [Houghton, J.T., et al. (eds.)]. Cambridge University Press, Cambridge, United Kingdom and New York, NY, USA, pp. 349– 416.

Remer, L. A., Y. J. Kaufman, D. Tanré, S. Mattoo, D. A. Chu, J. V. Martins, R.-R. Li, C. Ichoku, R. C. Levy, R. G. Kleidman, T. F. Eck, E. Vermote, and B. N. Holben (2005), The MODIS Aerosol Algorithm, Products, and Validation. *J. Atmos. Sci.*, 62, 947–973, doi:http://dx.doi.org/10.1175/JAS3385.1.

Remer, L. A., R. G. Kleidman, R. C. Levy, Y. J. Kaufman, D. Tanré, S. Mattoo, J .V. Martins, C. Ichoku, I. Koren, H. Yu, and B. N. Holben (2008), Global aerosol climatology from MODIS satellite sensors, *J. Geophys. Res.* 113, D14S07, doi:10.1029/2007JD009661.

Rissler, J., E. Swietlicki, J. Zhou, G. Roberts, M. O. Andreae, L. V. Gatti, and P. Artaxo (2004), Physical properties of the sub-micrometer aerosol over the Amazon rain forest during the wet-to-dry season transition—comparison of modeled and measured CCN concentrations. *Atmos. Chem. Phys.*, **4**, 2119–2143.

Rosenfeld, D., U. Lohmann, G. B. Raga, C. D. O'Dowd, M. Kulmala, S. Fuzzi, A. Reissell, and M. O. Andreae (2008), Flood or drought: How do aerosols affect precipitation? *Science*, 321(5894), 1309–1313.

Seinfeld, J. H. and S. N. Pandis, Atmospheric Chemistry and Physics: From Air Pollution to Climate Change, John Wiley & Sons, Inc., New York, 2006.

Shi, G.Y., et al., 2005: Sensitivity experiments on the effects of optical properties of dust aerosols on their radiative forcing under clear sky condition. *J. Meteorol. Soc. Japan*, 83A, 333–346.

Shrivastava. M., J. Fast, R. Easter, W. I. Gustafson Jr., R. A. Zaveri, J. L. Jimenez, P. Saide, and A. Hodzic (2011), Modeling organic aerosols in a megacity: comparison of simple and complex representations of the volatility basis set approach, Atmos. Chem. Phys., 11, 6639–6662, doi:10.5194/acp-11-6639-2011.

Singh, H. B., W. H. Brune, J. H. Crawford, F. Flocke, and D. J. Jacob (2009), Chemistry and transport of pollution over the Gulf of Mexico and the Pacific: spring

2006 INTEX-B campaign overview and first results, *Atmos. Chem. Phys.*, 9, 2301-2318, doi:10.5194/acp-9-2301-2009.

Storer, R. L., S. C. van den Heever, and T. S. L'Ecuyer (2014), Observations of aerosol-induced convective invigoration in the tropical east Atlantic, *J. Geophys. Res. Atmos*., 119, 3963–3975, doi:10.1002/2013JD020272.

Sukoriansky, S., B. Galperin, and V. Perov (2005), Application of a new spectral model of stratified turbulence to the atmospheric boundary layer over sea ice. *Bound.–Layer Meteor.*, 117, 231–257.

Tanaka, N., D. M. Rye, Y. Xiao, and A. C. Lasaga (1994), Use of Stable Sulfur Isotope Systematics for Evaluating Oxidation Reac- tion Pathways and in-Cloud Scavenging of Sulfur-Dioxide in the Atmosphere, *Geophys. Res. Lett*., 21, 1519–1522.

Tang, Y., G. R. Carmichael, G. Kurata, I. Uno, R. J. Weber, C. H. Song, S. K. Guttikunda, J. H. Woo, D. G. Streets, C. Wei, A. D. Clarke, B. Huebert, T. L. Anderson (2004), Impacts of dust on regional tropospheric chemistry during the ACE-Asia experiment: a model study with observations. *J. Geophys. Res.,* 109, D19S21. http://dx.doi.org/10.1029/2003JD003806.

Thompson, A. M., M. A. Owens, and R. W. Stewart (1989), Sensitivity of tropospheric oxidants to global chemical and climate change, *Atmos. Environ*., 23, 516-532.

Tie, X.X., S. Madronich, S. Walters, D. P. Edwards, P. Ginoux, N. Mahowald, R. Y. Zhang, C. Lou, and G. Brasseur (2005), Assessment of the global impact of aerosols on tropospheric oxidants. *J. Geophys. Res.,* 110, D03204. http:// dx.doi.org/10.1029/2004JD005359.

Tritscher, T., J. Dommen, P. F. DeCarlo, M. Gysel, P. B. Barmet, A. P. Praplan, E. Weingartner, A. S. H. Prévôt, I. Riipinen, N. M. Donahue, and U. Baltensperger (2011), Volatility and hygroscopicity of aging secondary organic aerosol in a smog chamber, *Atmos. Chem. Phys*., 11, 11477–11496.

Twomey, S.A., 1977: The influence of pollution on the shortwave albedo of clouds. *J. Atmos. Sci*., 34, 1149–1152.

Vali, G. (1985), Atmospheric ice nucleation—A review. *J. Rech. Atmos.*, **19**, 105–115.

van der Werf, G. R., J. T. Randerson , L. Giglio, G. J. Collatz, M. Mu, P. S. Kasibhatla, D. C. Morton, R. S. DeFries, Y. Jin and T. T. van Leeuwen (2010), Global fire emissions and the contribution of deforestation, savanna, forest, agricultural, and peat fires (1997–2009), *Atmos. Chem. Phys.*, 10, 11707-11735, doi:10.5194/acp-10-11707-2010.

Vestreng, V., G. Myhre, H. Fagerli, S. Reis, and L. Tarraso´n (2007), Twenty-five years of continuous sulphur dioxide emission reduction in Europe, Atmos. Chem. Phys., 7, 3663–3681.

Wang, G., R. Zhang, M.E. Gomez, L. Yang, M. L. Zamora, M. Hu, Y. Lin, J. Peng, S. Guo, J. Meng, J. Li, C. Cheng, T. Hu, Y. Ren, Y. Wang, J. Gao, J. Cao, Z. An, W. Zhou, G. Li, J. Wang, P. Tian, W. Marrero-Ortiz, J. Secrest, Z. Du, J. Zheng, D. Shang, L. Zeng, M. Shao, W. Wang, Y. Huang, Y. Wang, Y. Zhu, Y. Li, J. Hu, B. Pan, L. Cai, Y. Cheng, Y. Ji, F. Zhang, D. Rosenfeld, P.S. Liss, R.A. Duce, C.E. Kolb, M.J. Molina (2016), Persistent sulfate formation from London fog to chinese haze, *Proc. Natl. Acad. Sci. U. S. A.,* 113 (2016), pp. 13630–13635.

Wang, H., G. Shi, X. Zhang, S. Gong, S. Tan, B. Chen, H. Che, and T. Li (2015), Mesoscale modelling study of the interactions between aerosols and PBL meteorology during a haze episode in China Jing–Jin–Ji and its near surrounding region–Part 2: Aerosols' radiative feedback effects, *Atmos Chem Phys.,* 15, 3277-3287.

Wang, J., D. J. Allen, K. E. Pickering, Z. Li and H. He (2016), Impact of Aerosol Direct Effect on East Asian Air Quality During the EAST-AIRE Campaign, J. Geophys. Res. Atmos., 121, 6534–6554, doi:10.1002/2016JD025108.

Wang, L. T., Z. Wei, J. Yang, Y. Zhang, F. F. Zhang, J. Su, C. C. Meng, and Q. Zhang (2014), Then 2013 severe haze over southern Hebei, China: model evaluation, source apportionment, and policy implications, *Atmos. Chem. Phys*., 14, 3151-3173, doi:10.5194/acp-14-3151-2014 .

Wang, S. X., B. Zhao, S. Y. Cai, Z. Klimont, C. P. Nielsen, T. Morikawa, J. H. Woo, Y. Kim, X. Fu, J. Y. Xu, J. M. Hao, and K. B. He (2014), Emission trends and mitigation options for air pollutants in East Asia, *Atmos. Chem. Phys*., 14, 6571-6603, doi:10.5194/acp-14-6571-2014.

Wang, Y., J. Fan, R. Zhang, L. R. Leung, and C. Franklin (2013), Improving bulk microphysics parameterizations in simulations of aerosol effects, *J. Geophys. Res. Atmos.*, 118, 5361–5379, doi:10.1002/jgrd.50432.

Wild O, X. Zhu, and M. J. Prather (2000), Fast-J: Accurate simulation of in- and below cloud photolysis in tropospheric chemical models, *J. Atmos. Chem.*, 37, 245-282.

Xia, X., Z. Li, P. Wang, H. Chen, and M. Cribb (2007a), Estimation of aerosol effects on surface irradiance based on measurements and radiative transfer model simulations in northern China, *J. Geophys. Res. Atmos.,* 112, D22S10, doi:10.1029/2006JD008337.

Xia, X., Z. Li, B. Holben, P. Wang, T. Eck, H. Chen, M. Cribb, and Y. Zhao (2007b), Aerosol optical properties and radiative effects in the Yangtze Delta region of China, *J. Geophys. Res.*, 112, D22S12, doi:10.1029/ 2007JD008859.

Xin, J., et al. (2007), Aerosol optical depth (AOD) and Ångström exponent of aerosols observed by the Chinese Sun Hazemeter Network from August 2004 to September 2005, *J. Geophys. Res.*, 112, D05203, doi:10.1029/2006JD007075.

Yang, Q., W. I. Gustafson Jr., Fast, J. D., Wang, H., Easter, R. C., Morrison, H., Lee, Y. N., Chapman, E. G., Spak, S. N., and Mena-Carrasco, M. A. (2011): Assessing regional scale predictions of aerosols, marine stratocumulus, and their interactions during VOCALS-REx using WRF-Chem, Atmos. Chem. Phys., 11, 11951–11975, doi:10.5194/acp-11-11951-2011.

Zhai, P., X. Zhang, H. Wan and X. Pan (2005), Trends in Total Precipitation and Frequency of Daily Precipitation Extremes over China, Journal of Climate, 18, 1096-1107.

Zaveri, R. A., and L. K. Peters (1999), A new lumped structure photochemical mechanism for large-scale applications, *J. Geophys. Res.*, 104, 30,387– 30,415.

Zaveri, R. A., R. C. Easter, J. D. Fast, *and* L. K. Peters *(*2008*),* Model for Simulating Aerosol Interactions and Chemistry (MOSAIC)*, J. Geophys. Res.,* 113*, D13204, doi:*10.1029/2007JD008782.

Zhang, B., Y. Wang, and J. Hao (2015), Simulating aerosol–radiation–cloud feedbacks on meteorology and air quality over eastern China under severe haze conditions in winter, *Atmos. Chem. Phys.,*15, 2387–2404.

Zhang, Q., D. G. Streets, and G. R. Carmichael (2009), Asian emissions in 2006 for the NASA INTEX-B mission , *Atmos. Chem. Phys.*, 9, 5131–5153.

Zhao, C. and Y. Wang (2009), Assimilated inversion of NO_X emissions over east Asia using OMI NO_2 column measurements, *Geophys. Res. Lett*., 36, L06805, doi:10.1029/2008GL037123.